Characterization and Manipulation of Temperature-Driven Magnetic Phenomena: Magnetic Transition in FeRh Thin Films and Ultrafast Magnetization Reversal in a-$Gd_{22-x}Tb_xCo_{78}$ Thin Films

by

Alejandro Ceballos-Sanchez

A dissertation submitted in partial satisfaction of the

requirements for the degree of

Doctor of Philosophy

in

Engineering - Materials Science and Engineering

in the

Graduate Division

of the

University of California, Berkeley

Committee in charge:

Professor Frances Hellman, Chair
Professor Lane Martin
Professor Sayeef Salahuddin

Summer 2019

Characterization and Manipulation of Temperature-Driven Magnetic Phenomena: Magnetic Transition in FeRh Thin Films and Ultrafast Magnetization Reversal in *a*-$Gd_{22-x}Tb_xCo_{78}$ Thin Films

Abstract

Characterization and Manipulation of Temperature-Driven Magnetic Phenomena: Magnetic Transition in FeRh Thin Films and Ultrafast Magnetization Reversal in a-$Gd_{22-x}Tb_xCo_{78}$ Thin Films

by

Alejandro Ceballos-Sanchez

Doctor of Philosophy in Engineering - Materials Science and Engineering

University of California, Berkeley

Professor Frances Hellman, Chair

This work covers the characterization and manipulation of two temperature-driven phenomena: the meta-magnetic transition in FeRh thin films and the ultrafast magnetization reversal in amorphous Gd-Tb-Co thin films.

For FeRh, the separate effects of strain and film thickness were determined on the antiferromagnetic-to-ferromagnetic phase transition temperature of FeRh thin films by both experiment and density functional calculations. Strain was introduced by epitaxial growth onto MgO, $SrTiO_3$ and $KTaO_3$ substrates. Film thicknesses below 15 nm substantially suppress the transition temperature, T^*, to below room temperature in unstrained films. For strained films, tensile/compressive strain decrease/increase T^* respectively. $KTaO_3$ (001) substrates produce sufficient compressive strain to increase the transition temperature of 10 nm FeRh films above room temperature, useful for many proposed applications previously limited by the stabilization of the ferromagnetic state at small thicknesses. These results demonstrate that a judicious use of film thickness and substrate can be used to manipulate FeRh's transition temperature over a $\sim$200 K range.

Amorphous (a-) ferrimagnetic $Gd_{22-x}Tb_xCo_{78}$ thin films with perpendicular magnetic anisotropy show ultrafast helicity-independent all-optical switching (HI-AOS) from x = 0 to x = 18. Increasing Tb content causes increasing values of the magnetic anisotropy constant, slower remagnetization rates and higher critical fluences. Magnetic anisotropy and saturation magnetization do not correlate with magnetization reversal upon irradiation. The ultrafast magnetization measurements show that the dynamics of reversal are fastest in pure a-$Gd_{22}Co_{78}$ and progressively slow down as Tb at.% increases until only demagnetization occurs in a-$Tb_{22}Co_{78}$. Annealing reduces the anisotropy, increases the damping and causes slower remagnetization rates. Atomistic spin dynamics reproduces the experimental dynamics as well as the increased critical fluence required for switching. Increased damping from greater spin-orbit coupling arising from Tb's $L = 3$ value is responsible for the slower dynamics and greater critical fluence and explains why switching has not been observed in Tb-Co alloys. The high anisotropy in a-$Gd_{22-x}Tb_xCo_{78}$ thin films for x $\geq$

12 makes them excellent candidates for new high-density memory devices taking advantage of ultrafast magnetization reversal mechanisms.

Time resolved X-ray magnetic circular dichroism (TR-XMCD) measurements of a-$Gd_{10}Tb_{12}Co_{78}$ revealed the element-specific ultrafast magnetization reversal dynamics. It was found that Co demagnetizes fastest with a time constant of 320 fs, followed by Tb and Gd with time constants of 410 fs and 630 fs respectively. This is consistent with previous work showing that Tb's greater spin lattice coupling allows for thermal energy to be more easily transferred to the lattice, allowing it to demagnetize faster compared to Gd.

Structural characterization of the amorphous structure of Tb-Co alloys performed via fluctuation electron microscopy indicates that not all amorphous structures are the same as evidenced by differences in the mid range order (MRO) as a function of growth temperature. A distinction between MRO along the growth direction and along the in-plane direction suggests that the perpendicular magnetic anisotropy in these amorphous alloys is positively correlated with the degree of MRO. This technique enables structural characterization of amorphous materials by describing the differences between amorphous configurations as a function of MRO and tilt angle.

Amorphous, ferrimagnetic Tb-Co thin films prepared with a thin Ta underlayer and either a Ta or Pt overlayer show evidence of both a soft and a hard magnetic phase despite no sign of this at room temperature. Low temperature magnetometry measurements reveal the decoupling of the two magnetic phases with decreasing temperature due to increased anisotropy energy at lower temperatures. Decreasing the film thickness to 2 nm, slightly above the superparamagnetic limit found at 1 nm, a soft, low density phase was isolated and found to be present in all the films as confirmed with x-ray reflectivity (XRR) and Rutherford backscattering spectrometry (RBS) measurements. For greater thicknesses, the bottom layer retains its soft magnetic nature, while the remainder of the film is denser and has strong perpendicular magnetic anisotropy, leading to exchange-spring behavior when the anisotropy becomes large, either at low temperatures or via a Pt overlayer which adds a strong interfacial anisotropy to the layer. Micromagnetic simulations reproduced the experimental hysteretic behavior by incorporating the experimentally-determined anisotropy and magnetization parameters into a soft/hard bilayer model. The Pt capping layer produces a slightly larger anisotropy constant than the Ta capping.

A membrane-based X-ray transparent heater for application of large temperature gradients was designed – with guidance from a heat-transfer simulation – and fabricated for synchrotron-based imaging of domain wall motion driven by the spin Seebeck effect.

Contents

List of Figures

List of Tables

Acknowledgments

I want to thank my advisor Frances Hellman for handing me the opportunity and the freedom to have an idea and go for it. Your guidance and mentoring throughout this process have made this work possible. I am grateful to the members of my committee, Lane Martin and Sayeef Salahuddin, for taking the time to read this work and for their encouragement back when I was taking my qualifying examination.

It has been my pleasure to share the office and the lab with the many members of the Hellman lab over these past seven years. Many thanks to Cory Antonakos, Chloé Baldasseroni, Cathy Bordel, Simca Bouma and Michalis Charilaou for teaching me a lot about sample growth and magnetic characterization. They always were lovely to me and it meant a lot, much more than I can convey in words. Mentoring visiting German students André Kowalewski and Christian Simon was a lot of fun inbetwixt a lot of hard work helping me figure out why things were not working. I am thankful for their lasting friendship and coffee. Manel Molina-Ruiz has been a steadfast inspiration for how to manage a project, he's been a mentor in many ways and an integral part of my time here, and for that I thank him. All those conversations over coffee were full of ideas, and they served as a strong motivator. Your friendship has been invaluable. The younger core of the lab, Paul 'Big D' Corbae, Tom Dauer and Keerti Shukla have made the office very fun and it's been a pleasure to work with them and see them take ownership of their projects. Thank you for humoring my rants.

I want to thank my collaborators outside of the lab that have helped me with my projects. Ellis Kennedy and Mary Scott for their help with TEM and FEM characterization. I'm excited to see where this technique can go. Akshay Pattabi and Amal El-Ghazal were instrumental and invaluable in helping me get the ultrafast magnetization dynamics project off the ground. In addition, for the synchrotron experiments Niko Pontius and Christian Schuessler were extremely helpful and beyond patient during our beamtime. Jon Gorchon and Ilie Radu provided experience and foresight during those stressful days. My sincere appreciation to all of you.

As part of the Non-Equilibrium Magnetic Materials collaboration, I want to thank all its members for their insight and discussions during our twice-a-month meetings. Jeff Bokor, Sayeef, Steve Kevan, Sujoy Roy, Peter Fischer, Richard Wilson, Jon, Noah Kent, Robert Streubel, Simca and Lin-Wang Wang. I learned a lot about how to prepare for a talk from these interactions.

Finally I want to thank my family and dedicate this work to them. My brother, my father and my mother, invisible to so many but ever-present to me. They're the people behind the scenes that should get most of the credit for where I am today. They've given me so much without ever expecting something in return. They listened, they cared, they laughed and they love me and that's all that matters to me. Gracias!

Thanks to all the taxpayers for funding and supporting me via a National Science Foundation Graduate Research Fellowship under Grant No. DGE 1106400. This work was also supported by the Director, Office of Science, Office of Basic Energy Sciences, Materials Sciences and Engineering Division, of the U.S. Department of Energy under Contract No. DE-AC02-05-CH11231 within the Non-equilibrium Magnetic Materials Program (KC2204).

Chapter 1

Introduction

Heat typically has a detrimental relationship with magnetism. Heat a ferromagnetic material sufficiently and it will destroy its magnetization. However, sometimes heat can lead to very interesting and non-destructive magnetic phenomena. For instance, equiatomic FeRh was discovered in 1939 by Fallot et al. to undergo an unusual temperature-driven magnetic phase transition [1]. The two different magnetic phases were later identified as antiferromagnetic (AF) and ferromagnetic (FM) with the AF phase transitioning into FM with increasing temperature[2, 3]. This phase transition can also be driven by a magnetic field, defining it as a metamagnetic transition, and is coupled to a lattice expansion. Current investigations of this unique transition range from the fundamental understanding of the origin and nature of the transition [4] to applications associated with the transition such as a giant magnetocaloric effect and a giant volume magnetostriction[5]. A large reason for the interest in FeRh in thin film form is that thin films have been proposed as a candidate material for heat-assisted magnetic recording (HAMR) in an exchange-spring system coupled to a hard magnetic layer (for example FePt or CoPt) [6, 7]. In those thin films, the transition temperature has been shown to be sensitive to changes in composition and substrate-induced strain as well as structural and chemical order and these effects remain to be fully understood. The thin film form is ideal in providing easy control of film composition and stress to allow the study of these factors on the phase transition mechanism.

Chapter 2 is a study on the effect of strain and thickness on the transition temperature of FeRh. It is largely a reprint of ”Effect of strain and thickness on the transition temperature of epitaxial FeRh thin-films” published in Applied Physics Letters, reprinted with permission from the authors, Copyright 2017, AIP Publishing LLC.

An examination of the inconclusive results on optically detecting the spin Seebeck effect, another thermally-driven magnetic effect, is presented in Chapter 3. The spin Seebeck effect refers to the generation of a spin current in a ferromagnet when subjected to a temperature gradient. This chapter details the development of a membrane-based heater device with the goal of enabling temperature-gradient synchrotron microscopy studies, specifically the imaging of domain wall motion as a consequence of the spin Seebeck effect as predicted by Hinzke et al[8]. A heat transfer simulation model of the device that includes conduction, radiation and convection heat loss, is presented. The design of the X-ray transparent heater features temperature homogeneity and a

large temperature gradient region while maintaining a thin thermal conduction layer. This chapter introduces rare earth (RE) - transition metal (TM) alloys, the subject of the rest of this dissertation, and explains why these are interesting and useful material systems.

Briefly, RE-TM alloys are ferrimagnetic materials, in which the RE and the TM form two magnetic sublattices. For heavy RE, those with more than half-filled f-electrons, their magnetic moments couple antiferromagnetically with those of the TM. However, since the moment of one sublattice is greater than the other there is a net magnetization despite the negative exchange between them. At a certain temperature the magnetic moments of both sublattices compensate each other and the magnetization is zero, this is known as the compensation temperature. Properties such as the saturation magnetization, anisotropy, coercivity, compensation temperature, Curie temperature and more can be tuned as a function of composition, growth temperature and annealing temperature. Making them very useful systems with a rich parameter space.

Chapter 4 is an investigation of the amorphous structure of ferrimagnetic a-$Tb_{16}Co_{84}$ done with fluctuation electron microscopy. This technique permits the relative quantification of medium range order (MRO) and it presents a clear correlation between changes in MRO and changes in the perpendicular magnetic anisotropy.

Chapter 5 presents further structural and magnetic characterization of a-$Tb_{18}Co_{82}$. Exchange-spring behavior was found only at low temperatures and X-ray and Rutherford backscattering measurements revealed the presence of a thin, lower density layer that forms in the initial stages of the growth, which then recovers as the growth progresses. The effect of this low/high density bilayer results in a magnetically soft/hard bilayer which is modeled via micromagnetic simulations. It also presents that capping the samples with Pt leads to higher anisotropy constants, likely due to a thin interdiffused layer of Co-Pt forming at the Tb-Co/Pt interface.

The thermally induced magnetization switching (TIMS), also known as helicity-independent all-optical switching (HI-AOS) is the subject of Chapters 6 and 7 and marks the last thermally-driven phenomena studied in this work. HI-AOS is a puzzling phenomenon in which irradiation of a ferrimagnetic material with a fs laser pulse deterministically reverses the magnetization of the material in the irradiated area. This can be done reversibly an indeterminate number of times using nothing but a randomly polarized laser pulse, i.e. there is no transfer of angular momentum as there would be from a circularly polarized laser pulse. This means that the magnetization is being reversed purely by the thermal energy delivered by the laser pulse. Its underlying physical mechanism is still unresolved, and there is an apparent exclusivity to this phenomenon being found only in Gd-TM alloys.

Chapter 6 is a study of the ultrafast magnetization dynamics of a-$Gd_{22-x}Tb_xCo_{78}$ done via time resolved magneto optical Kerr effect (TR-MOKE) measurements. It reveals that films with as little as 4 at.% Gd are still able to exhibit HI-AOS, and finds a progressive change in the magnetization reversal rate as a function of composition. Films higher in Tb composition were found to exhibit slower dynamics until only demagnetization was observed in a-$Tb_{22}Co_{78}$. An explanation for what enables this phenomenon is presented in terms of the magnetic damping and its effect on the critical fluence, the minimum threshold laser power needed to reverse the material.

Chapter 7 is a complementary study done on a-$Gd_{10}Tb_{12}Co_{78}$ using time resolved X-ray magnetic circular dichroism (TR-XMCD) at the femtoslicing facility in BESSY II. It presents prelim-

inary data on the separate, element-specific magnetization dynamics of the three magnetic sublattices, Gd, Tb and Co. An attempt is described to resolve THz oscillations that could in principle exist in AF-coupled systems such as RE-TM alloys.

Chapter 2

Effect of Strain and Thickness on the Transition Temperature of Epitaxial FeRh Thin-Films

2.1 Introduction

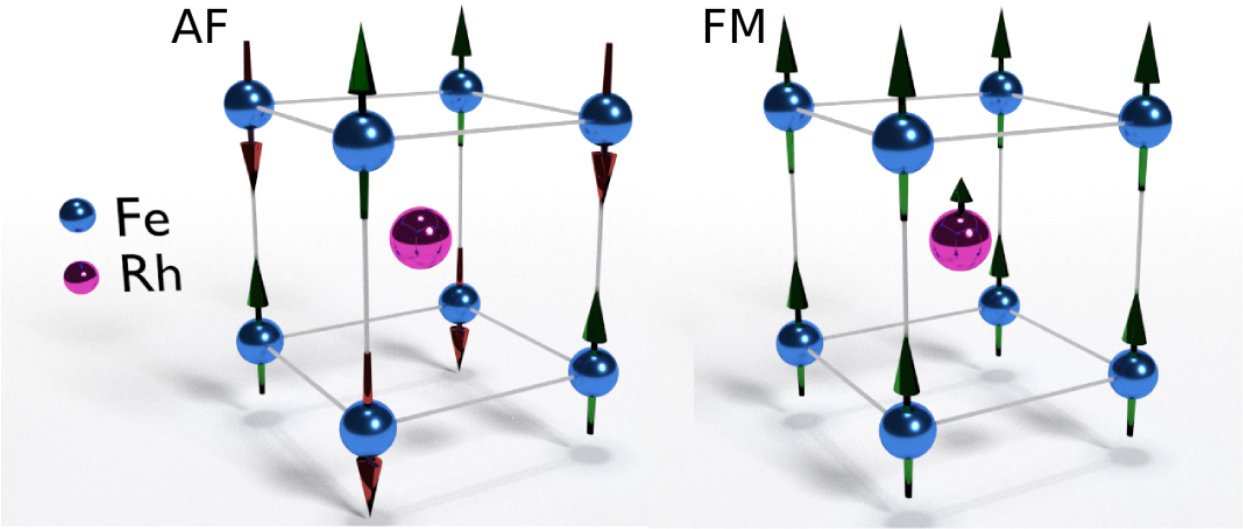

Figure 2.1: Illustration of the magnetic configuration of FeRh. In the AF state (left) the Fe moments lie parallel along the (111) planes and Rh possesses no magnetic moment. In the FM state (right) Fe and Rh are collinear.

CsCl-ordered FeRh has attracted and sustained interest since 1938 [1, 9] due to its first-order magnetic phase transition from an antiferromagnetic (AF) to a ferromagnetic (FM) state when heated above a transition temperature $T^* \approx 350$ K [10, 11]. Fig. 2.1 depicts the magnetic con-

figurations of FeRh; in the FM phase it has a collinear structure with 3.2 μ_B per Fe atom and 1.0 μ_B per Rh atom; the antiferromagnetic phase is G-type with 3.1 μ_B per Fe atom and zero Rh moment [4]. Proposed applications include heat-assisted magnetic recording (HAMR) in an exchange-spring system coupled to a hard magnetic layer,[12, 13] and magnetic refrigeration due to the large entropy change at the AF-FM transition[14, 15].

In order to employ FeRh for magnetic media applications, thin films with well-defined transitions are required[16, 17]. Reduced film thickness however leads to a lower transition temperature[18, 19], hindering the proposed storage applications. Accompanying this transition is an isotropic 1% lattice expansion, indicating that the magnetic order and the lattice of FeRh are strongly coupled. This has been further demonstrated by experiments using a ferroelectric substrate that induces strain via either an applied voltage [20], or by a structural phase transformation of the substrate[21]. Strain in FeRh films also causes a spin reorientation accompanying the AF-FM transition, as well as perpendicular anisotropy in the AF phase[22]. The effects of strain and thickness however have not been deconvolved.

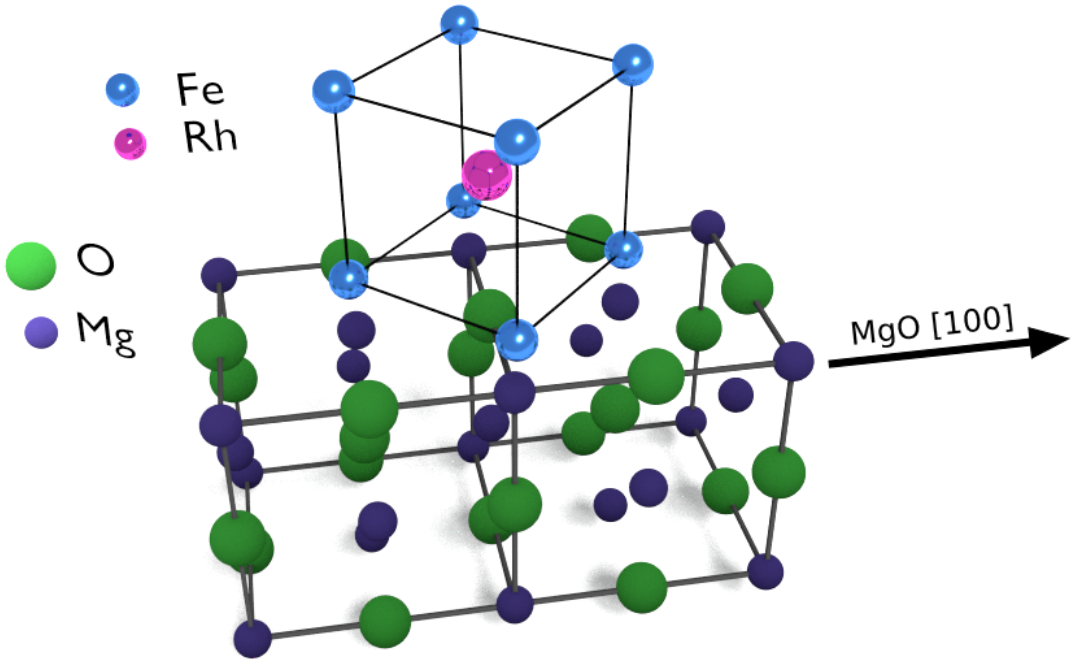

Figure 2.2: Illustration depicting how FeRh achieves epitaxy on MgO by growing at a 45 degree angle with respect to the substrate's [010] and [100] directions.

In this study we determine the separate effect of film thickness and strain from epitaxial growth of FeRh thin films deposited on substrates of varying lattice constants. The bulk FeRh lattice parameter is 2.985 Å in the AF state, and 2.995 Å in the FM state. Strain arising from epitaxial growth is modulated by lattice mismatch between film and substrate. Three substrates were used: MgO, $KTaO_3$(KTO) and $SrTiO_3$(STO) which are cubic with lattice parameters of 4.216 Å, 3.989

Å and 3.905 Å respectively. FeRh grows at a 45 degree angle with respect to the substrate's [010] and [100] in plane directions as seen in Fig. 2.2, so the effective lattice parameters of the substrates are 2.981 Å, 2.821 Å and 2.761 Å. The effect of tensile strain was studied using a 100 nm thick film grown onto high energy ion-beam-assist-deposited (001) MgO (IBAD MgO) which was found to produce significant tensile strain[22, 23].

2.2 Thin Film Growth and Characterization

Epitaxial FeRh thin films of thicknesses 10, 15, 22 and 100 nm were grown by dc magnetron sputtering deposition from a single equiatomic FeRh target at a growth rate of 0.4 Å/s. The base pressure was 8 x 10^{-8} torr, and the growth pressure was 2 mtorr of Ar. Films were grown at 873 K, and capped at room temperature with 3 nm of Pt, shown in previous work [24] to eliminate an interfacial FM phase that can form at the film/capping interface. The composition of all films was determined to be 48 at.% Fe / 52 at.% Rh using energy dispersive X-ray spectroscopy.

Epitaxial relationships and lattice parameters were obtained from θ-2θ and ϕ scans with an X-ray diffractometer (XRD) as shown in Fig. 2.3. Fig. 2.3a shows the x-ray diffraction patterns of FeRh films on the four substrates covered in this study. Shifts in FeRh's (001) and (002) peak positions are indicative of strain and this is easier to see on the film on KTO which is shifted to the left and is compressively strained. Films on MgO and STO have no shift; one because of good lattice matching as is the case with MgO, and the other due to relaxed epitaxy in which misfit dislocations have nucleated and relieved the strain. Lastly the film on IBAD MgO is shifted to the right and the film is under tensile strain. Fig. 2.3b shows that the FeRh films are epitaxial by comparing the peak positions of the film's (101) peaks with the substrates' (101) peaks; shown is a representative scan comparing an FeRh film grown on KTO. The 45 degree peak separation between film and substrate peaks in conjunction with the results from Fig. 2.3a determine the epitaxial relation: (001) FeRh // (001) substrates and [100] FeRh // [110] substrates. Finally 2θ scans of FeRh's (101) off-axis peak were used to determine the in plane lattice parameter, and a characteristic set of scans for the films grown on KTO are shown in Fig. 2.3c

The magnetic properties including the phase transition were determined using a superconducting quantum interference device (SQUID) magnetometer and a vibrating sample magnetometer (VSM). With the exception of the films grown on KTO, the magnetization (M) as a function of temperature was measured in a magnetic field of 5 T in the SQUID; this field decreases the transition temperature by -8 K/T[22, 11]. The films on KTO were measured in a VSM since their full transition could not be captured by the SQUID's maximum temperature of 400 K. The magnetization as a function of temperature for these KTO samples was measured in a 1 T magnetic field.

Because there is substantial hysteresis associated with the first order AF-FM transition, which induces significant lattice expansion which is converted to strain due to the constraint of the substrate[22], it is crucial to establish whether samples are in the FM or AF state (and not in some mixed state) when M(H) or XRD is measured. To ensure this, a specific thermal and field history was used for each sample because of different T^* and breadth of transition. For samples

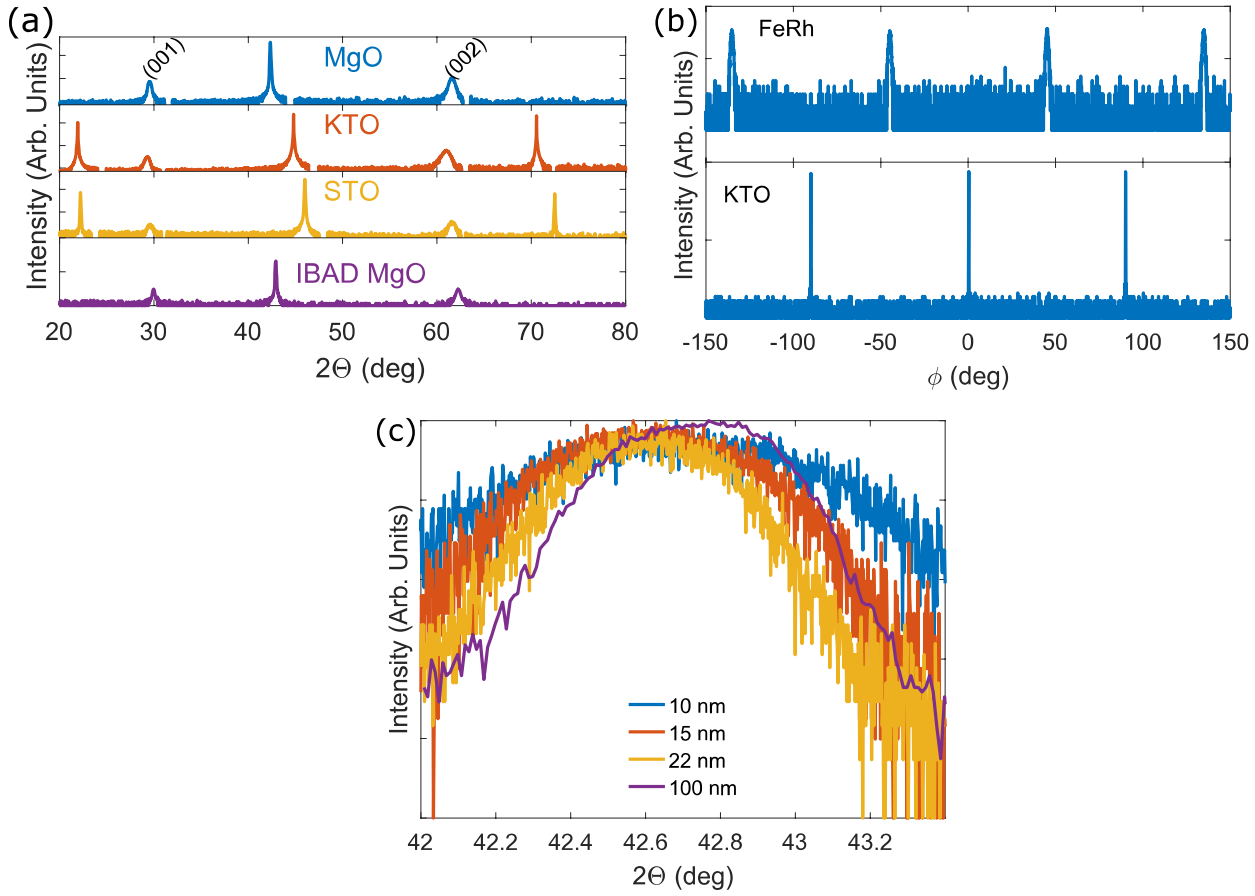

Figure 2.3: (a) Out of plane 2θ scans of FeRh films on four different substrates, MgO, KTO, STO and IBAD MgO. FeRh's (001) and (002) peaks were used to calculate the out of plane lattice parameter, the high intensity peaks correspond to the substrate's $\{001\}$ family of peaks. (b) ϕ scans about FeRh's off-axis (101) peak compared with KTO's (101) show that FeRh is epitaxial and grows at a 45 degree angle with respect to the substrate. (a) and (b) confirm the epitaxial relationship: (001) FeRh // (001) substrates and [100] FeRh // [110] substrates. (c) 2θ scans of FeRh's (101) off-axis peak used to determine the in-plane lattice parameter of FeRh films deposited on KTO.

on MgO and STO, the samples were first cooled to 100 K (in zero field), then M(T) was measured from 100 – 400 K in a 5 T field. At 400 K M(H) was measured, followed by M(T) from 400 – 100 K also in 5 T. The samples were then cooled to T $<$ 10 K and subsequently warmed up to 300 K for removal (with both sequences done under zero field). At the end of this process the 100 and 22 nm thick films on MgO and STO were fully in the AF state at room temperature, while the 15 and 10 nm thick films on MgO and STO were in a mixed state. To address this the latter films were given an extra treatment consisting of heating to 400 K, then cooling from 400 – 300 K, both in a 5 T field. This results in the 10 and 15 nm thick films on MgO and STO being in the FM state at

room temperature. The KTO samples instead were first cooled to 77 K in a liquid nitrogen bath, followed by M(T) measurement in the VSM from 310 K – 500 K in a 1 T field. This history leads all samples on KTO to be fully in the AF state at room temperature. XRD determined the epitaxial relationship of all films to be: (001) FeRh // (001) substrates and [100] FeRh // [110] substrates.

2.3 Discussion

Figure 2.4 plots the transition temperatures T^* of all films as a function of film thickness. The inset shows M(T) for a 22 nm film grown on MgO and indicates the transition temperatures upon cooling and heating in a 5 T field. Substantial hysteresis is seen in this transition, as discussed in the literature[24, 25]. The transitions on heating (T^*_{AF-FM}) and cooling (T^*_{FM-AF}) are defined as the maximum of the first derivative of M(T). The transition width is defined as the difference between T^*_{AF-FM} and T^*_{FM-AF}. The transition temperature, T^*, is then defined as the midpoint of T^*_{AF-FM} and T^*_{FM-AF}. The data is shown as measured in a 5 T field; for films on KTO the 1 T measurements were corrected to 5 T by shifting T^* down by 32 K. The zero-field T^* is approximately 40 K higher than the 5 T T^*.

Figure 2.4a shows that T^* decreases sharply with decreasing film thickness below 22 nm for all substrates. It also shows that T^* depends on substrate, which we will show below is due to a dependence on strain. For MgO and STO, T^* drops below room temperature for films thinner than 15 nm, making this material impractical for many applications. However, FeRh films grown on KTO exhibit a considerably higher transition temperature such that even the thinnest films have T^* above room temperature.

The width of the transition is presented in Fig. 2.4b Consistent with previous reports[18, 19], a broadening of the hysteresis is observed as the thickness of the film decreased. Previous work[26, 25]has shown that AF domains nucleate preferentially at crystallographic defects with very little domain growth. In contrast, while the nucleation of the FM phase is also heterogeneous, it is then followed by significant growth of the domains. The data in Fig. 2.4b suggest that both the FM and AF phases are less easily nucleated and their domain walls are more easily pinned in thinner films, but a more careful study would be required to fully understand the nucleation and growth of both phases in these thin films.

The strain of all films was extracted from XRD measurements of the *c* and *a* lattice parameters using the (002) and the off-axis (101) peaks respectively. Ratios of c/a exceeding one correspond to films under compressive strain while c/a below one corresponds to films in tensile strain. Specifically, films with compressive (tensile) strain correspond to films with an in-plane lattice parameter smaller (greater) than the bulk AF or FM lattice parameter at any given temperature.

Figure 2.5a shows that FeRh films grown on MgO and STO exhibit no strain with c/a values close to unity for all thicknesses, while films grown on KTO are compressively strained, and the film grown on IBAD MgO is tensilely strained. The films on KTO display decreasing strain with increasing film thickness, indicating the nucleation of misfit dislocations that release the strain as the film thickness is increased. The low strain of films grown on MgO is due to the close match of the lattice constant of MgO to that of FeRh. The low strain of films grown on STO, where

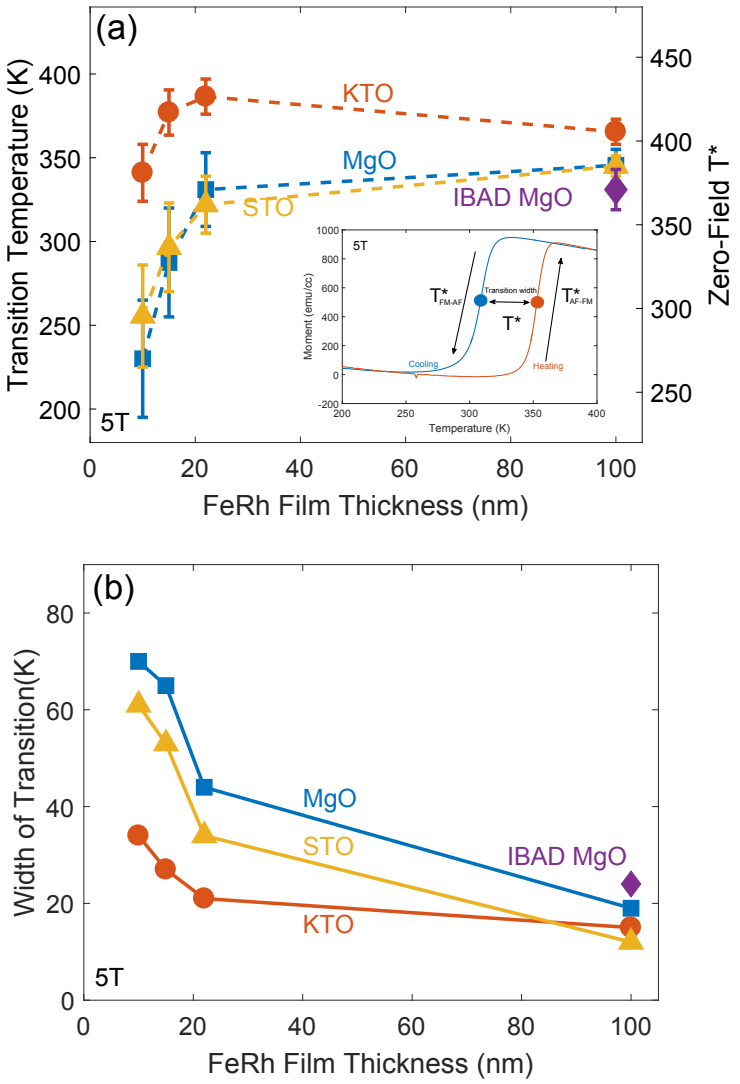

Figure 2.4: (a) Transition temperature T* as a function of film thickness as recorded under a 5 T field (left axis) and adjusted to zero field (right axis). Decreasing thickness decreases the transition temperature across all films. Inset illustrates the magnetization as a function of temperature for a 22 nm FeRh film grown on MgO. The transition temperatures on heating and cooling are indicated and their average equals the transition temperature T*. All magnetization measurements were done with the field along the plane of the film. (b) The width of the transition is the difference between the transitions on heating and cooling:T^*_{AF-FM} and T^*_{FM-AF}. All values are as recorded in a 5 T magnetic field except for films grown on KTO which were measured in a 1 T field and then corrected to 5 T by subtracting 32 K.

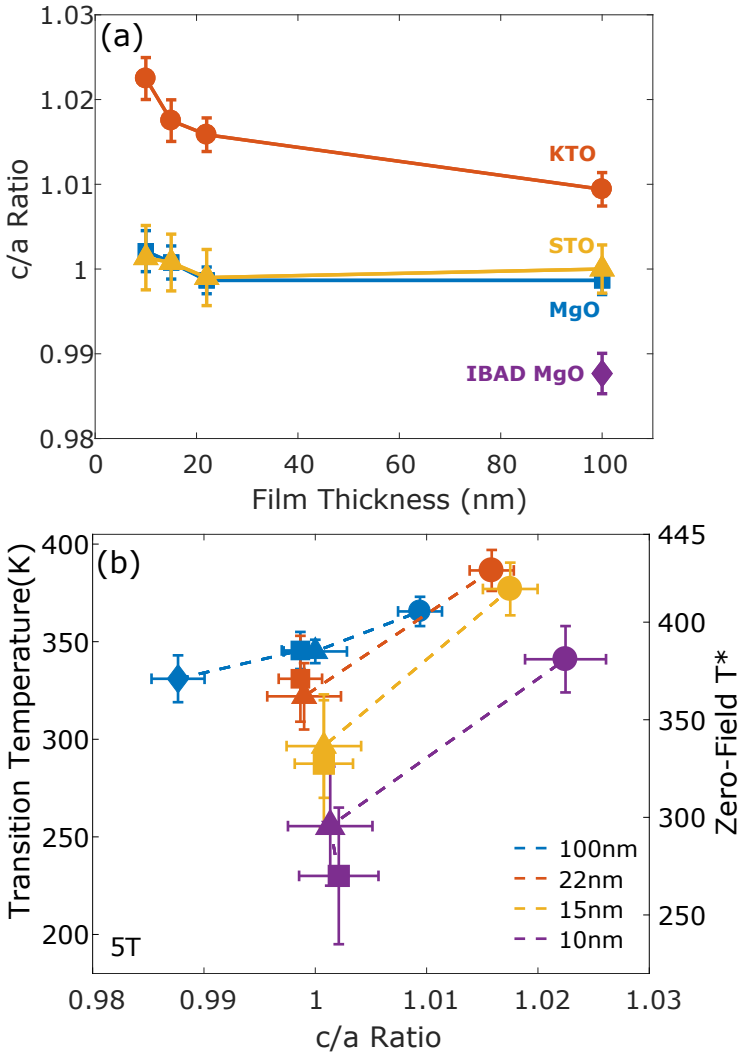

Figure 2.5: (a) Thickness dependence of the strain. Films on KTO(IBAD MgO) are under compressive(tensile) strain. (b) The transition temperature recorded in 5 T (or corrected by 32K for the KTO samples recorded in 1 T) as a function of c/a ratio for films of fixed thicknesses. Tensile strain corresponds to c/a < 1 and compressive to c/a > 1. Films 15 nm and below on MgO and STO had their c values corrected to the AF state by taking into account the 1% volume expansion (see suppl. matls.). Circles, squares, triangles and diamond correspond to FeRh films grown on KTO, MgO, STO and IBAD MgO respectively.

significant strain was expected, is due to strain relaxation occurring in even the thinnest films. The fact that the strain state of films grown on MgO and STO is similar results in comparable transition temperatures as seen in Fig. 2.5b. KTO however, has lower lattice mismatch than STO, allowing for a higher critical thickness past which the nucleation of strain-relieving defects begins; this

results in films that are somewhat compressively strained even at film thicknesses of 100 nm. For the film on IBAD MgO the strain is tensile, and the effect of tensile strain is seen to be a decrease in T^*. Notably, the 10 nm film on KTO has T^* comparable to bulk.

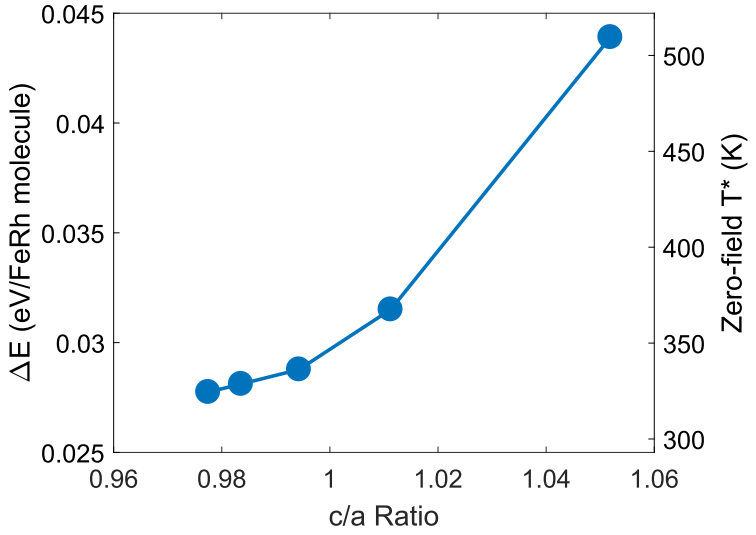

Figure 2.6: The calculated energy difference ΔE ($E_{FM} - E_{AF}$) per FeRh molecule between the FM and the AF state vs c/a ratio for a bulk (thick) sample. The extraction of the zero-field transition temperature (right axis) is described in the main text. The c/a value in the x-axis uses the lattice parameter of AF state for a selected value of $a = b$ after relaxation of c.

Density functional theory (DFT) calculations (technical details in Appendix A) allow simulation of the effect of strain and thickness on the electronic and magnetic properties of FeRh. We first perform the calculations for the bulk system at zero strain. These calculations yielded magnetic moments and spin polarized density of states (Appendix A) that agree with literature values[27, 28]. Next, the in-plane lattice parameters, $a = b$, were changed to emulate the strain produced by the different substrates and the out-of-plane, c axis, was relaxed.

The total free energy of FM and AF states was then calculated and then the energy difference ΔE ($E_{FM} - E_{AF}$) per FeRh molecule between the two states was obtained. ΔE is the difference in free energy between the two states, and hence the change in ΔE is proportional to the change in T^*, as will be discussed below.

For $c/a = 1$, ΔE = 0.03 eV/FeRh molecule. Since there is no entropy difference at zero temperature between the AF and FM states, and the difference in Gibbs free energy at T^* is zero, ΔS between the AF and FM states equals $\Delta E/T^*$ (for any c/a). This is assuming that the non-zero temperature contribution is independent of c/a as discussed in Appendix A. Since T_0^*, the transition temperature for c/a = 1, is $\sim$ 350 K, this gives ΔS_0 at T_0^* for unstrained FeRh of 0.03 eV/FeRh molecule/350 K $\sim$ 3.25 x 10^{20} eV/kg/K, about three times larger than the experimental value measured by latent heat or integration of C/T (see Appendix A) of 1.06 x 10^{20} eV/kg/K[14].

This discrepancy suggests an overestimation of ΔE which itself is very sensitive to the lattice parameters and computational methods[29, 4], however this will not affect the qualitative discussion below, nor the estimate of the shift in T* with strain, as discussed in suppl. matls. This ΔS_0 is due to vibrational, magnetic and electronic degrees of freedom as discussed in previous work[14] which showed that all three contribute, but magnetic energy differences dominate. From this, assuming that the effect of strain on the excitation spectrum is smaller than its effect on the ground state energy we approximate the change in T^* as proportional to the change in ΔE with respect to bulk using a Taylor expansion (see Appendix A): $T^* = T_0^* \left(1 + \frac{(\Delta E - \Delta E_0)}{\Delta E_0}\right)$ where ΔE_0 = 0.03 eV/FeRh molecule. The result is shown in Fig. 2.6. For $c/a = 0.994$, the change in ΔE $\approx$ -1.2 meV yielding a decrease of 14 K, consistent with the drop in T^* with tensile strain. For c/a > 1, ΔE and T^* increase, e.g. for c/a = 1.011 (close to the 100 nm film on KTO), the change in ΔE $\approx$ 1.5 meV, corresponding to an increase in T^* of 17 K, consistent with the increased T^* for compressive strain seen in the 100 nm film on KTO in Fig. 2.5b.

Note that the above ΔE is calculated without considering spin anisotropy. The anisotropy energy (i.e. energy difference between in-plane spin configuration and out-of-plane spin configuration) is sub-meV [22], much smaller than the changes in ΔE with strain. We also note that in the FM state, the in-plane spin configuration is preferred under tensile strain while the out-of-plane spin configuration is preferred under compressive strain and the reverse is seen for the AF state[22]. Thus the anisotropy energy provides a small linear correction term (i.e., proportional to c/a) to ΔE.

DFT calculations also looked at the effect of thickness. Calculations were performed on structures with two, four, six and eight monolayers (ML), each layer containing one layer of Fe atoms and one layer of Rh atoms. For each case the energy and magnetic moments of FM phase, G-type AF and A-type AF were calculated; A-type was included as it has been found to be more stable than G-type for ultra-thin films[30]. For the FM phase, Fe has 3.17 μ_B and Rh about 1.05 μ_B for all thicknesses. For G-type AF phase, Fe is 3.11 μ_B, lower than that of the FM state, and the moment for Rh is almost zero. For the A-type AF, the moment of Fe is about 3.14 μ_B, while the value for Rh is no longer zero but has a 0.87 μ_B spin-up moment in one layer and a 0.40 μ_B spin-down moment in the next layer, decreasing quickly to zero with increasing layers.

Figure 2.7 shows the energy difference ΔE between FM and AF states for different number of monolayers. The right axis is derived similarly to Fig. 3 using a Taylor expansion in 1/N (see suppl. matls.). The G-type AF is the lowest energy state in bulk, as known experimentally, with the higher energy FM state stabilized at high temperature (due to excitational, i.e. $T > 0$, entropy differences between the two states[14]). For thinner films, the energy difference is reduced and the FM state is the ground state at and below 6 layers. This dependence of energy difference on thickness corresponds to a decreasing T^* with decreasing film thickness, as seen experimentally (Fig. 2b). There is also a crossover between the G- and A-type AF states' energies at and below 2 layers, indicating that A-type is more stable than G-type in ultra-thin films (but in both cases, the FM state is more stable than the AF state).

A polynomial fit of ΔE vs the inverse of the thickness 1/N allows us to extract ΔE for a 10 nm film as seen in the inset of Fig. 2.7. Comparing this value to bulk we see a decrease in ΔE of 6.6

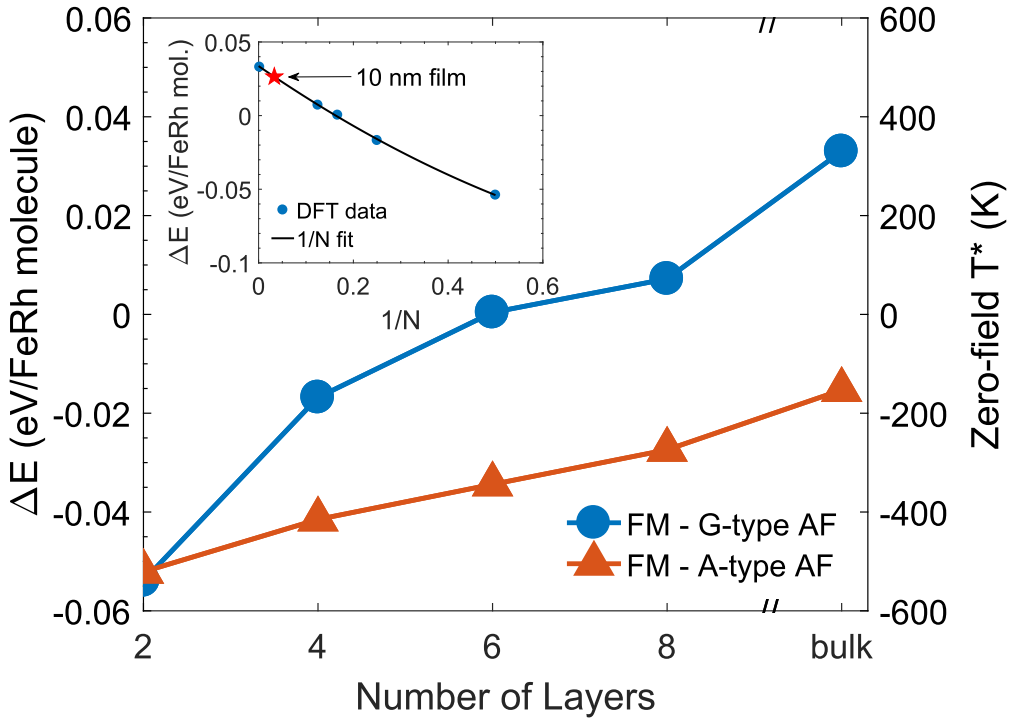

Figure 2.7: The calculated energy difference ΔE ($E_{FM} - E_{AF}$) per FeRh molecule between the FM and the AF state (G-type and A-type) as a function of number of monolayers N. The extraction of the zero-field transition temperature (right axis) is described in the main text. T* below 0 K simply indicates that no transition exists, as the FM state has lower energy. The inset shows the 1/N fit used to extract T* for a 10 nm film.

meV predicting a T* of 273 K in zero field, very close to our zero field T* of 270 K and 296 K for our unstrained, 10 nm films on MgO and STO.

2.4 Conclusion

In conclusion, the transition temperature of epitaxial FeRh films is found to depend on both thickness and strain; T* decreases with decreasing film thickness and increases with c/a ratio. For unstrained films, T* drops below room temperature for films below 15 nm in thickness. Tensile strain decreases T* and compressive strain increases T*. These effects are seen both experimentally and in DFT calculations, with excellent agreement between predicted and measured T*. For technological applications above room temperature, FeRh films epitaxially grown on KTO substrates are attractive candidates for magnetic storage applications as even 10 nm films possess a T* comparable to that of bulk FeRh.

Chapter 3

X-Ray Transparent Heater Design for Application of Temperature Gradients

3.1 Introduction

The field of spin caloritronics, or spin-caloric transport, addresses the interplay between spin current phenomena and thermal properties. For almost two centuries it has been known that heat and charge currents are coupled, causing the phenomenon of thermoelectricity. However, only recently have researchers realized that these concepts can be reconsidered by including the spin, generating completely new spin-related properties. In recent years, a zoo of spin caloritronic effects have been discovered, which are spin-dependent generalizations of the classical Seebeck, Peltier or Nernst effects in bulk materials. Indubitably, the discovery of the longitudinal spin Seebeck effect has caused the most excitement out of the three[31, 32, 33]. Here a temperature gradient over a metallic contact on a magnetic insulator generates spin currents that can be detected via the inverse spin Hall effect as a transverse voltage. Historically, the spin Seebeck effect has been discussed in two variations, distinguished by the orientation of the direction of heat flow with respect to the interface involved in detection of the spin transport. These variations are known as the longitudinal and transverse spin Seebeck effects. The former is routinely observed in magnetic insulators (such as yttrium iron garnet, YIG)/heavy metal bilayers, but not in metallic samples since it cannot be separated from the anomalous Nernst effect. Likewise, the transverse spin Seebeck effect in metallic systems is difficult to detect because the anomalous Nernst effect possesses similar symmetry and their contributions to the voltage read out is confounded.

However, following the work by Hinzke et al.,[8] it was theorized that the spin current from the spin Seebeck effect can be used to move magnetic domain walls given a large enough temperature gradient. Their prediction stipulated that a temperature gradient in the K/μm range would produce a domain wall velocity of a few m/s. The prediction elaborated that when the temperature gradient is applied to the ferromagnet, the hot end generates magnons which diffuse away towards the cooler side. As this magnonic spin current travels through the ferromagnet it will transfer angular momentum to any domain wall on its way and exert a thermal spin transfer torque that will cause

the domain wall to be dragged towards the hot side. Thus the idea for this project was borne to optically detect the spin Seebeck effect in a metallic system by applying a temperature gradient and expecting to observe domain wall motion upstream towards the hot end as illustrated in fig. 3.1.

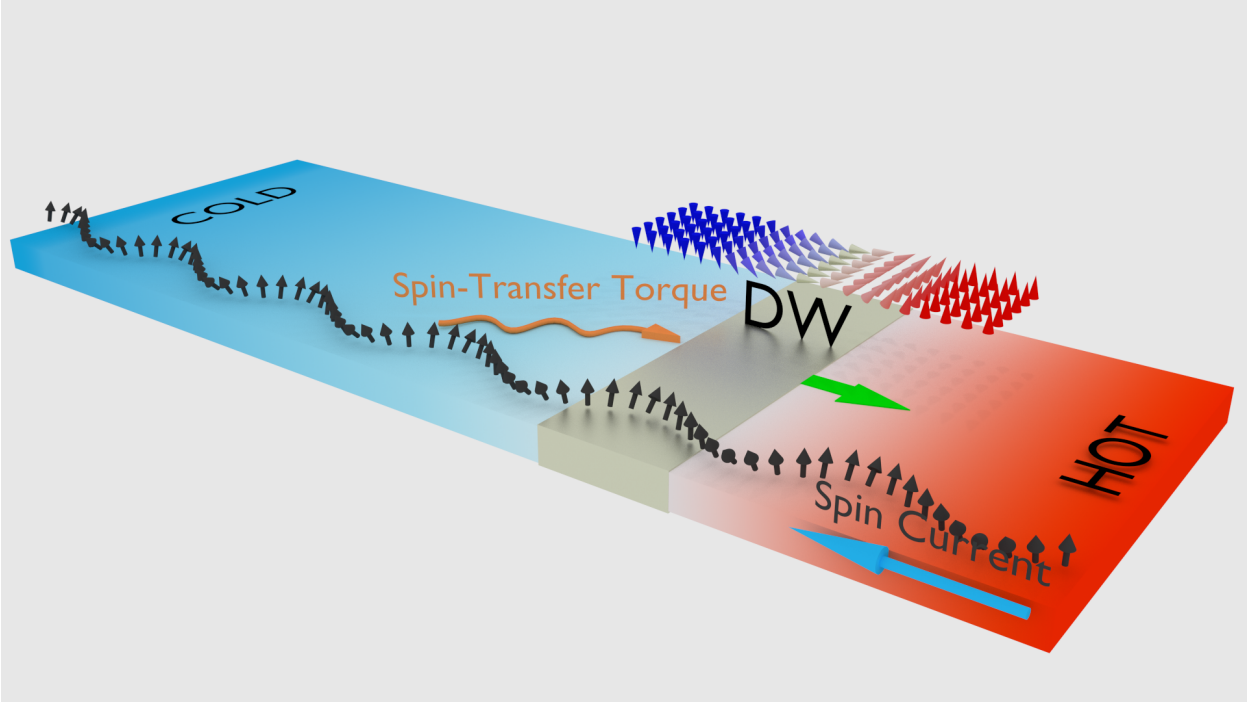

Figure 3.1: Illustration of the spin Seebeck effect. A temperature gradient in a magnetically ordered material produces a spin current that diffuses away from the high temperature side. The transfer of angular momentum produces thermal spin transfer torque which results in domain wall motion towards the hot end.

Imaging would be done at XM-1, the magnetic transmission X-Ray microscope at Beamline 6.1.2 at the ALS. An X-Ray transparent heater stage would be designed and fabricated building up on the preliminary work previously published by the lab[34], in which a heater stage had been designed to produce a homogeneous temperature distribution in the footprint of the heater. Here the isothermal region would be used instead as the hot end to produce large temperature gradients.

The metallic magnetic system selected for this study was amorphous(a-), ferrimagnetic Tb-Co. Terbium - Cobalt is part of a large family of Rare Earth (RE) - Transition Metal (TM) alloys that can be grown amorphous and yet display perpendicular magnetic anisotropy (PMA). The magnetic moments of heavy RE atoms with more than half filled f-electrons couple antiferromagnetically with those of TM atoms, resulting in a negative exchange that tends to align the RE moments anti-parallel to TM moments. As illustrated in fig. 3.2, the directions of RE moments are randomly canted from the direction anti-parallel to the TM moments because of random single-ion anisotropy of RE elements, resulting in non-collinear ferrimagnetism. In a-Tb-Co the two anti-

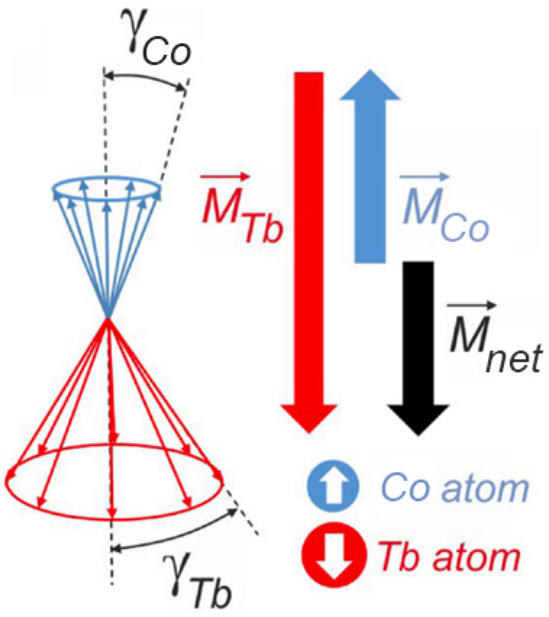

Figure 3.2: The spin configuration present in amorphous, ferrimagnetic Tb-Co alloys.Despite being antiferromagnetically coupled, the magnetization of one sublattice is greater than the other, resulting in a net magnetization. At a certain temperature the magnetization of both sublattices cancel each other out and it is said that the magnetization has been compensated, this temperature is the compensation point/temperature.

ferromagnetically coupled magnetic sublattices can cancel the other's magnetization at a specific temperature called the compensation temperature. In fig. 3.2, the terbium magnetization is greater than that of cobalt, so it is described as being Tb-dominant. If the temperature is then raised above the compensation temperature, the Co sublattice will have a larger magnetization and the alloy will be described as Co-dominant. The point is that this alloy undergoes a compensated point at which the magnetization disappears, and then nucleates with different character at either side of compensation. Therefore it would be interesting to test if under the same temperature gradient the domain wall dynamics are different depending on whether the sample is Tb-dominant or Co-dominant.

Another reason why *a*-Tb-Co was selected for this study is that the sample needs to have PMA since XM-1 is only sensitive to the out of plane component of the magnetization. While that requirement is satisfied by many other RE-TM alloys, a further constraint were the high temperatures the sample would be subjected to in order to produce the high temperature gradients (since Beamline 6.1.2 does not offer cooling capabilities). Thus a RE-TM alloy with high uniaxial anisotropy and high Curie temperature (T_C) was necessary. Hansen et al.[35] determined that of all the available heavy RE elements Tb produces the highest uniaxial anisotropy constant. Then Co was found

to be superior to Fe in Tb-TM alloys as not only did Co produce a stronger increase in T_C with increasing Co content, Fe actually has a decrease in its ordering temperature thanks to Fe-Fe anti-ferromagnetic exchange occurring in the high Fe-concentration alloys, reaching a maximum T_C of about 450 K. Thus the combination of PMA, large T_C, high anisotropy and a compensation point makes *a*-Tb-Co a very interesting material to study, not to mention that many of these properties can be tuned by composition, growth temperature and annealing temperature as will be shown in subsequent chapters.

3.2 Design and Simulation

The device to produce the temperature gradients is based off a Pt spiral design that is patterned onto a SiN membrane using a lithography mask. On the backside of the membrane a Au layer is patterned to cover the footprint of the Pt spiral and its purpose is to act as a thermal conductive layer that homogenizes the temperature. This design was characterized by Baldasseroni et al.[34] and it is ideal for steady-state heating of magnetic materials and allowing the use of X-Ray transmission techniques to study diverse effects as a function of temperature. For the purpose of this project the intent is not to uniformly heat the sample but to produce a gradient, so the design was modified to include a second heater as depicted in fig. 3.3a. By elevating the temperature of one heater the sample is subjected to a temperature gradient as the Au layers extend from one edge of the sample to the other as shown in fig. 3.3b, transferring heat through the thickness of the SiN membrane.

Since the thermal transport is influenced by the thickness of the materials a three-dimensional model had to be implemented. For this the COMSOL multiphysics software using the Joule Heating interface models Joule heating in the Pt heater by solving the time-dependent heat equation:

$$\rho C_p \frac{\partial T}{\partial t} - \nabla(\kappa \nabla T) + \varepsilon\sigma(T_{amb}^4 - T^4) + h(T_{amb} - T) = \mathbf{Q}$$

- ρ is the density (kg/m^3)
- C_p is the heat capacity (J/(kg K))
- κ is the thermal conductivity (W/(m K))
- T is temperature (K)
- t is time (s)
- ε is the emissivity
- σ is the Stefan-Boltzmann constant
- h is the convective heat transfer coefficient (W/(m^2 K))
- $\mathbf{Q}$ is the heating source (W/m^3)

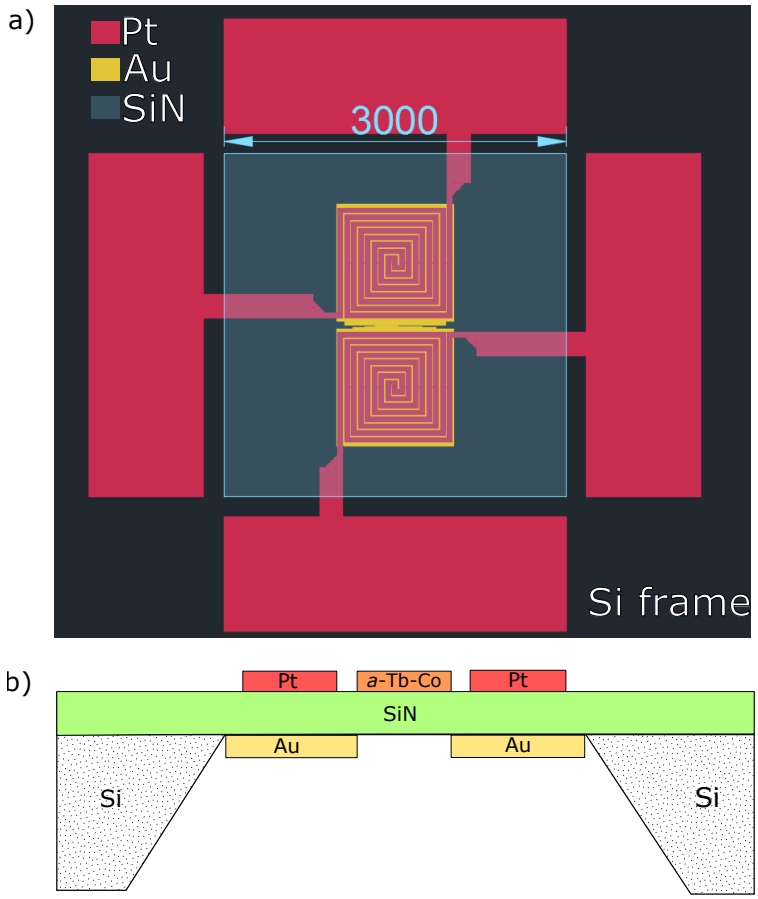

Figure 3.3: a) Top down view schematic of the two-heater design to produce large temperature gradients. The sample would be placed in between the two spiral Pt heaters. The device allows for application of temperature gradients in two opposite directions; when one heater is off it acts as a heatsink to ensure that one end of the sample is as cool as possible. The length scale is in units of μm. b) Cross-sectional view of the device illustrating the position of the sample between the two Pt heaters, and Au thermal conduction layers. The Pt and Au layers are electrically insulated by the intermediary SiN membrane. Not shown are the Pt contact pads used to power the heaters.

The first term of the equation describes the time-dependence of the temperature, the second term is conduction which represents the heat lost by conduction through the different layers of materials that constitute the device. Third term is heat lost by radiation via Pt and Au, and finally the fourth term is heat lost by convection through the surrounding air.

The density, heat capacity, and thermal conductivity of Au and Pt were assigned via COMSOL's built-in material library which takes into account the changing material properties as a function of temperature. The emissivities assigned were 0.15 and 0.09 for Pt and Au respectively as measured in [34], and the convective heat transfer coefficient was 137 W/(m^{2}K) as described in Baldasseroni's work as well.

For silicon nitride the thermal conductivity, density and heat capacity were defined as 25 W/(m K), 2330 kg/m^3, and 700 J/(kg K) as measured previously in the lab[36]. Finally the thicknesses for Au and SiN were set to 100 nm whereas for Pt the thickness was set to 20 nm.

The results of the simulation are shown in fig. 3.4 which shows identical temperature profiles and near identical temperature gradients across the sample region, with the bottom heaters (fig.3.4c and fig.3.4d) producing a slightly greater temperature gradient with a max of 35 K/μm compared to the top heaters (fig.3.4a and fig.3.4b). This difference is due to the design of the Au layer, which is shaped into terraces as shown in fig. 3.5. The Au terraces of the top and bottom heaters are highlighted in yellow in fig. 3.5a and b, with b) being a close up to better illustrate the step-like shape of the bottom Au terrace compared to the top which is flat. The terrace structures allow for different distances and therefore gradients to be applied as shown in fig.3.6a, which lists the distances between Au conductive layers in μm. This asymmetry in the design is why the bottom heater produces a slightly larger temperature gradient. These simulations were run with a current source of 4 mA for a simulated time of 5 ms. The temperature reaches its maximum after 4 ms.

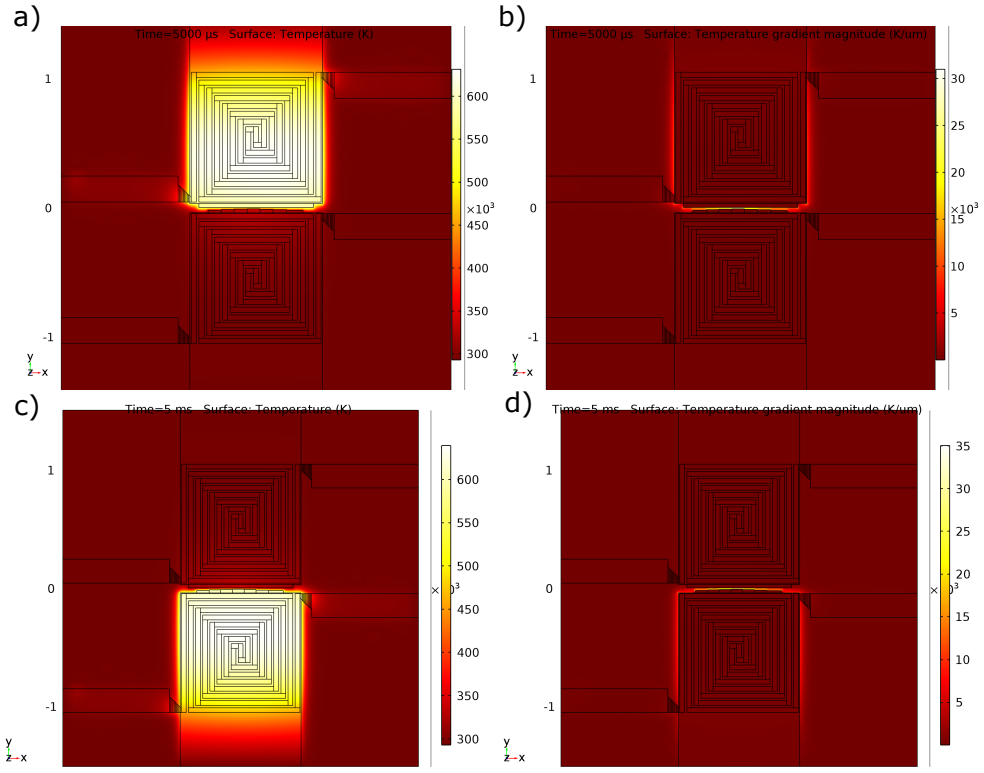

Figure 3.4: a) and b) are the temperature and temperature gradient profiles respectively of the top heater. c) and d) are those of the bottom heater. Simulation run with 4 mA as input heating source for 5 ms of total simulated time.

The design of the patterned *a*-Tb-Co samples with legs of decreasing width are illustrated in fig. 3.6b, these allow for the possibility of confining a single domain wall whose width depends

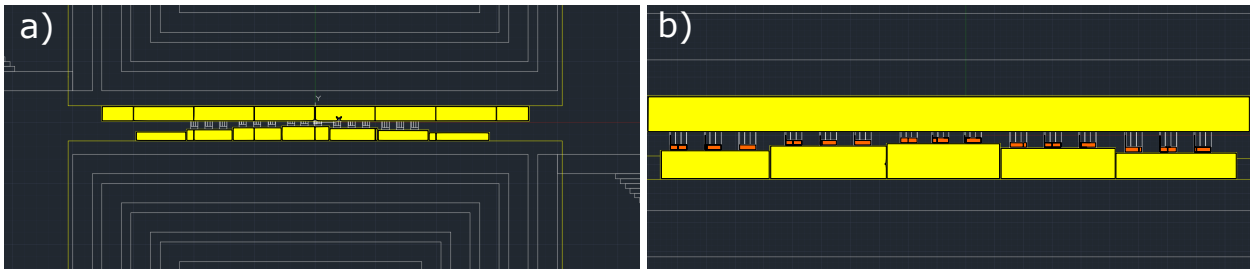

Figure 3.5: a) Highlighted in yellow are the relevant ends of the Au thermal conductive layers where the magnetic sample will be deposited in between them. The bottom terraces offer different distances from the flat-ended top terrace. b) is a close-up of the area between the terraces displaying the location of patterned *a*-Tb-Co samples (highlighted in orange) which can be subjected to different temperature gradients as a function of the distance between the two Au conductive layers.

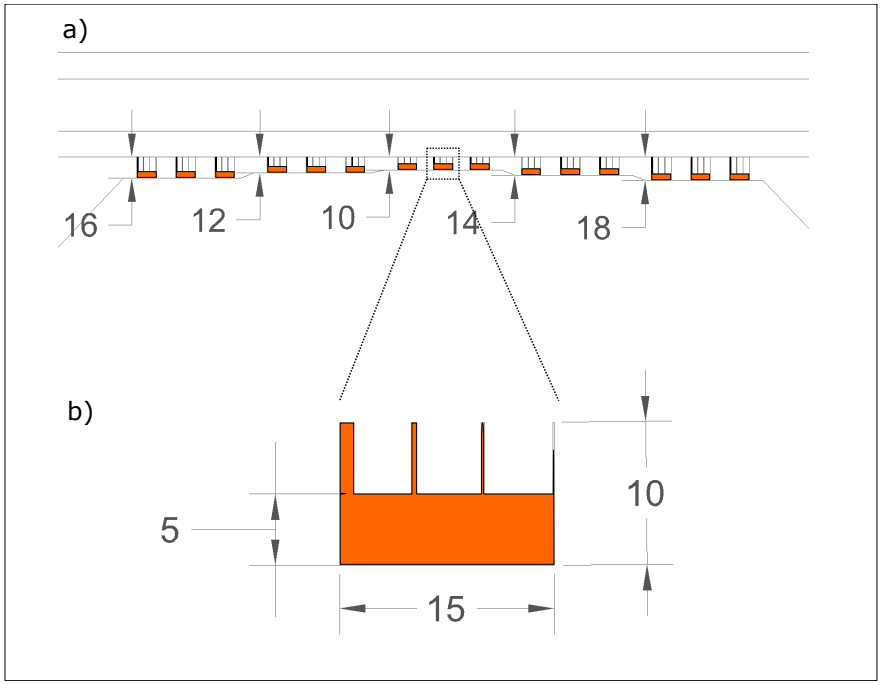

Figure 3.6: a) Simplified view of the terraces with the listed distances between Au conductive layers in units of μm. b) Close up of the patterned *a*-Tb-Co sample. The width of the legs are in decreasing order: 1 μm, 500 nm, 200 nm and 100nm. All listed distances are in μm.

on the anisotropy constant of the sample which itself depends on composition and temperature. The temperature gradients achieved between the Au layers are plotted in fig. 3.7 for the different distances between Au layers and as expected the greatest gradient is achieved when the distance between Au layers is minimized. Each plot corresponds to a different cut line as illustrated in the inset that runs from one Au layer, through the sample, and onto the other Au layer. Thus the

simulations show that the design of the device and the patterning of the sample allows for the application of different and reversible temperature gradients on samples that permit the confinement of a single domain wall for ease of observation.

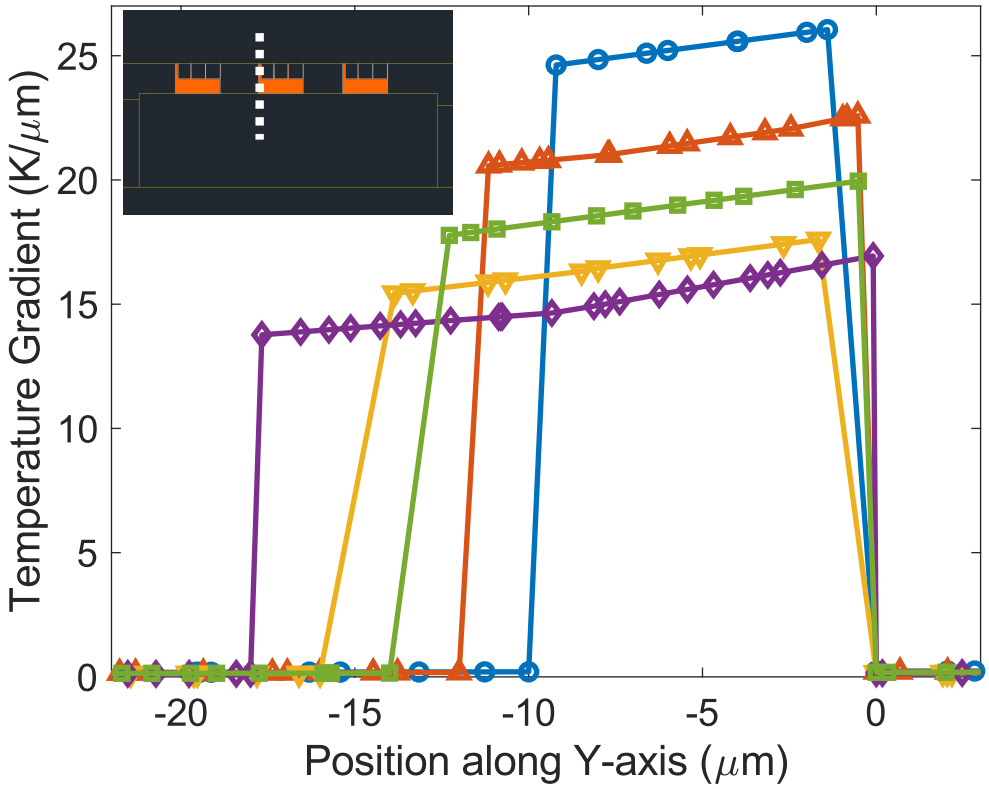

Figure 3.7: Temperature gradients across different cut lines as exemplified in the inset (dotted white line is the cut line) for different step heights.

3.3 Fabrication

A prototype to test the viability of the heater device was fabricated at the Nanolab taking advantage of the available masks and recipes for the heater described in [34]. The prototype consisted of a single Pt spiral heater and two Au thermal conductive layers, one underneath the heater shaped as a square and the other next to the heater as indicated by the arrow in fig. 3.8 shaped like a blunt tip. Note the presence of strain bands present in the SiN membrane around the patterned Pt device, this would lead to several device failures as the membrane would pop from the thermal load of operating the device. Annealing the Pt heater post lift-off relieved some of the stress present in the membrane, but there were certain regions such as at the corners of the spiral and the contact

where strain would mostly be present. The Pt was 20 nm thick with a heater line-width of 40 μm and a heater line spacing of 20 μm. The Au conductive layer was 100 nm thick on a 100 nm SiN membrane.

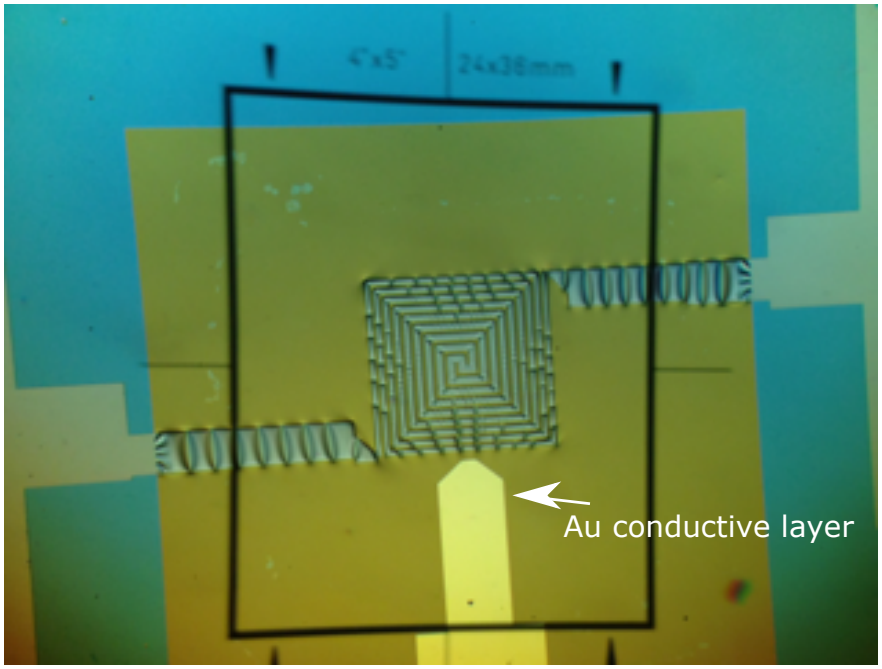

Figure 3.8: The prototype device with a single heater and two gold conductive layers. The *a*-Tb-Co sample would be deposited and patterned onto the gap between the heater and the tip-shaped Au conductive layer indicated by the arrow. The second Au conductive layer is underneath the square Pt spiral heater and is not visible in this view. Note the strain bands surrounding the heater.

Amorphous Tb-Co with a composition of 23% Tb - 77% Co was deposited onto test membranes patterned via e-beam lithography to test doses and liftoff before patterning and depositing onto the prototype heater. This atomic composition yielded films with a compensation temperature of $\sim$ 450 K so that the film could traverse compensation during operation of the heater if so desired. The film was planned to be grown at 300 ^{o}C in order to stabilize the magnetic anisotropy and prevent it from decaying. However, it was learned after one test growth onto patterned membranes that the PMMA resist used in e-beam lithography undergoes a glass transition at 110 ^{o}C. As can be seen in fig. 3.9a and b the results are irredeemable. Fig. 3.9a and b picture the general degradation of the photoresist after undergoing its glass transition. Lift-off was attempted by soaking the chip in acetone for 17 hours to no avail. The chip was then placed in a sonicator and unsurprisingly this popped the membrane. The test growth aimed at determining the optimal e-beam dose for lift-off. Fig. 3.9b shows that seven columns with repeating patterns like those shown in fig. 3.6 were written onto the membrane. Each column was written with a different dose, ranging from 320 to 440 μC/cm^2 in 20 μC/cm^2 steps. Subsequent test growths permitted depositions at 100 ^{o}C with successful lift-off at a dose of 400 μC/cm^2.

Heaters were tested with a DC current and showed that 4-6 mA of applied DC current lead to stable operation of the heater as long as the heater's resistance was near 7 kΩ. Heaters with resistances much smaller than this were correlated with devices that exhibited more stress and were thus prone to breakage. Exceeding the current limit was found to lead to the membrane popping due to thermal stresses that cause the membrane to buckle.

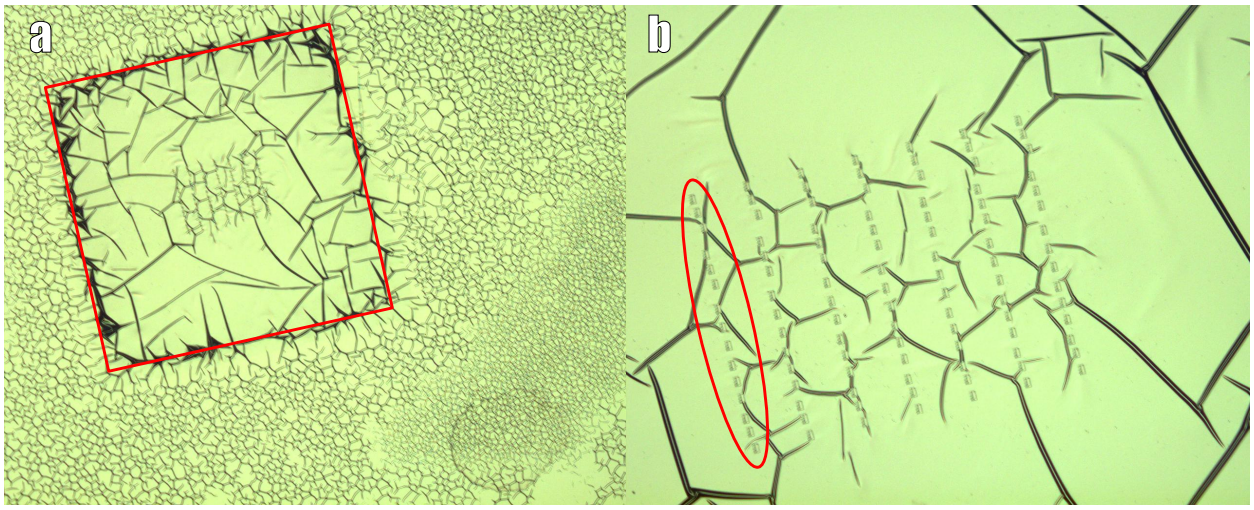

Figure 3.9: a) Zoomed out view of a test SiN membrane (the off-centered square highlighted in red) with 7 columns of repeating e-beam patterns done at different doses to test what electron beam dose yields successful lift-off after a 20 nm thin film growth at 300 ^{o}C of a-$Tb_{23}Co_{77}$. The cracks are from the degraded photoresist that failed to lift-off and this is the resulting image after leaving the sample in acetone for 17 hours. Outside the square is a-TbCo on photoresist on SiN on Si substrate. b) Close up of the columns of e-beam patterns, one of the columns of repeating e-beam patterns is highlighted in the red oval.

A completed device with patterned a-$Tb_{23}Co_{77}$ samples is shown in fig. 3.10. The sample is 50 nm thick with a capping layer of Al 10 nm thick to prevent oxidation. Since Tb-Co grows amorphous, it can be grown directly onto the SiN membrane.

3.4 Results

Heater devices were taken to XM-1 at the ALS on three separate occasions with no evidence of domain wall motion. Samples were imaged in the as-grown state in order to ensure that the sample was in a multi-domain state with X-Rays tuned to the Co L3 edge. There are several reasons that could explain why no domain wall motion was observed. The first is that a-$Tb_{23}Co_{77}$ has very strong domain wall pinning. As evidenced by the initial magnetization curve of the sample in fig. 3.11, the main mechanism of coercivity is pinning of domain walls. Thus it's possible that the spin Seebeck effect was not sufficient to overcome the pinning intrinsic to a-$Tb_{23}Co_{77}$.

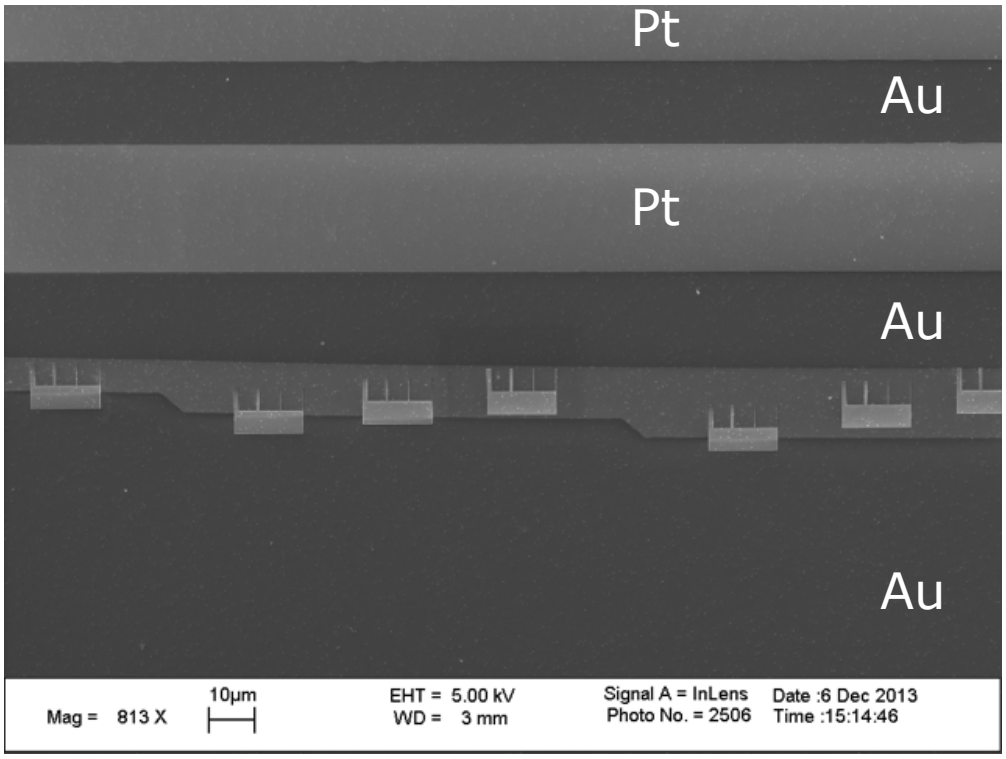

Figure 3.10: Scanning electron microscope image of the successfully patterned a-$Tb_{23}Co_{77}$ samples. The dark grey corresponds to the Au conductive layers as labeled and the two, top lighter gray horizontal stripes are two of the Pt heater lines as indicated.

It was also observed that magnetic contrast was lost during operation of the heater at 4 mA and above. Since this would be expected if we approach compensation, a separate device with a-$Tb_{19}Co_{81}$ with compensation below room temperature was tested, but it led to similar results. Thus it became apparent that the sample was losing its magnetic anisotropy during operation. Since PMMA degrades with growths above 100 ^{o}C, this was a hard limitation that could not be circumvented in a-Tb-Co.

Asides from the technical difficulties experienced, on a more fundamental level reports questioning the existence of the spin Seebeck effect in metallic ferromagnets were published near the time, explaining that the anomalous Nernst effect and other parasitic thermomagnetic effects can easily produce the voltages detected via ISHE [37]. Hinzke's work [8] predicates that a magnonic spin current in a metal could have both electronic and magnonic character, but that is still an open question since so far it is not clear how big the two contributions, charge-based and magnonic, are to the spin Seebeck effect. In a metal the spin-diffusion length is in the order of 10 nm[38], so it's hard to believe that a coherent spin wave will propagate through the length of 15 μm. Finally, the studies on spin Seebeck effect as well as the general theory indicate a stronger manifestation of a spin wave if the sample is uniformly magnetized. In our experiment the starting point was a multi-domain state, and uniformly magnetizing the sample would mean staring at a black or

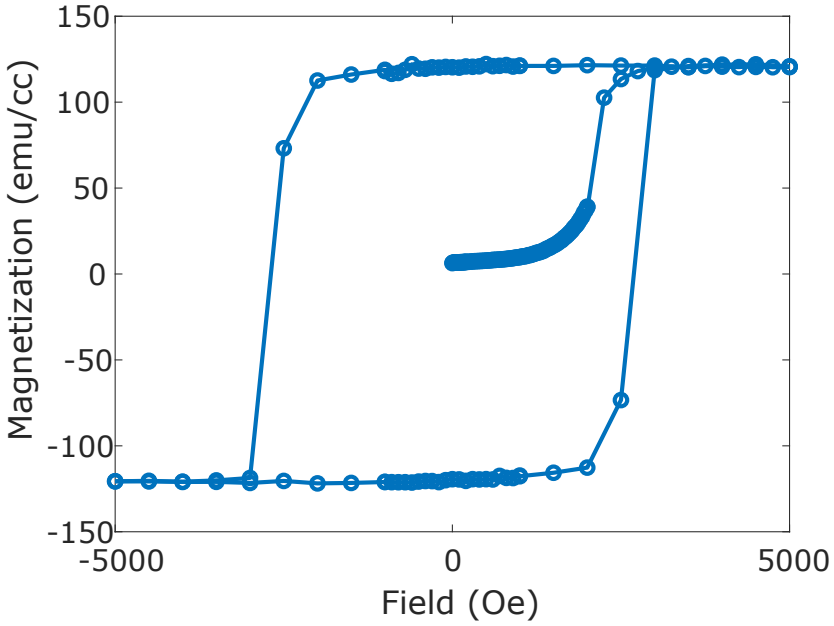

Figure 3.11: Magnetization as a function of applied field as measured in a SQUID magnetometer. The initial magnetization curve demonstrates that the main source of coercivity is via pinning of domain walls.

white image. In the end, it became difficult to motivate overcoming the technical challenges when the theoretical support started to falter. Today, the spin Seebeck effect is the exclusive domain of magnetic insulators.

3.5 Conclusion

The combination of early negative results in conjunction to the discouraging reports that removed or questioned the initial motivation and theoretical support led to the cancellation of the project. Nonetheless the devices designed allow for application of large temperature gradients and work just as well for temperature-based experiments with synchrotron techniques that require X-Ray transmission.

Chapter 4

Fluctuation Electron Microscopy on *a*-$Tb_{16}Co_{84}$ Thin Films

4.1 Introduction

For a homogeneous, amorphous material there should be no anisotropy in the structure and therefore no magnetic anisotropy. However, it has been known since the early 1970s that sputtered, amorphous rare earth (RE) - transition metal (TM) alloys can exhibit a uniaxial anisotropy perpendicular to the film plane[39, 40, 41] with values of the uniaxial anisotropy constant, K_u, in the range of 10^4 to 10^7 ergs/cm^3. This subject has been quite a controversial one and hundreds of papers have been written in an attempt to explain the origins of this perpendicular anisotropy. A review of the literature shows that there have been several favored models for this perpendicular anisotropy. They include: 1) a pair-ordering model or an atomic or nanoscale structural anisotropy, 2) a form of microstructural anisotropy having to do with columnar growth or other defect structures, and 3) magneto-elastic interactions involving strain due to a substrate plus inverse magnetostrcition. For pure rare earths with orbital-angular momentum, i.e. a non-zero L value such as in Tb, it is well-known that the single-ion anisotropy is the main source of anisotropy. It has also been found that increasing the RE atomic percent increases the anisotropy when alloyed with a TM[42], and that Tb-based alloys yield the RE - TM systems with greatest anisotropy constants [43].

An important result on the structural origins of perpendicular magnetic anisotropy (PMA) in sputtered, amorphous RE-TM films is that of Harris et al.[44]. The authors performed Extended X-ray Absorption Fine Structure (EXAFS) measurements to study the structure of several *a*-Tb-Fe films prepared by ion-beam sputtering. Their results showed a distinct difference for the coordination numbers parallel and perpendicular to the film, with an excess number of Fe/Fe and Tb/Tb pairs in the plane of the film and an excess number of Tb/Fe pairs perpendicular to the plane of the film. This indicates that the strong uniaxial anisotropies occurring in RE-TM alloys are due to the deposition process (evaporation, sputtering) causing local anisotropic atomic arrangements that lead to a preferred magnetic axis parallel to the film's normal.

Work by Hellman et al. found that the anisotropy increased with increasing growth temperature[45].

The authors hypothesized a rearrangement of local adatom configurations into energetically favorable orientations which minimize surface energy during the growth, termed a surface-mediated amorphous texturing of the film. It was also found that the anisotropy was independent of the state of stress in the film during the growth and thus suggested that magneto-elastic effects are relatively small compared to the basic growth-induced structural anisotropies. Thus, growth-induced anisotropic pair correlations plus single-ion anisotropy have emerged as the dominant explanation of PMA in RE-TM alloys.

Recent advances in technique and hardware of transmission electron microscopy (TEM) permit for detection of changes in the medium range order (MRO), ordering on the 1-4 nm scale which has yet to be properly characterized in RE-TM systems. Fluctuation electron microscopy (FEM) is a scanning nanodiffraction technique sensitive to MRO. By calculating the variance in intensity as a function of spatial frequency using a series of diffraction patterns, relative MRO can be determined. In this work, FEM was used to determine if MRO can be correlated to perpendicular magnetic anisotropy changes in heat treated *a*-$Tb_{16}Co_{84}$ thin films. This investigation evaluates whether FEM can be used as a more accessible alternative to synchrotron-based structural characterization methods.

4.2 Thin Film Growth and Characterization

Thin films of *a*-$Tb_{16}Co_{84}$ 30 nm in thickness were grown by sputtering deposition onto TEM windows and solid silicon nitride substrates. Samples were grown by co-sputtering from separate Tb and Co targets at a background pressure of 8.8 x 10^{-8} torr, with 1 mtorr of Ar. Samples were capped with 7 nm of Ta to prevent oxidation. Two series of growths were done; the first was grown at room temperature and then annealed at 200 ^{o}C and 350 ^{o}C for 1 hour. The second series varied the growth temperature, producing films grown at room temperature, 200 ^{o}C and 350 ^{o}C. Paralleling these growths were Ta controls 7 nm in thickness grown directly onto TEM windows that followed the same thermal treatment as described above. Atomic composition was measured via Rutherford Backscattering Spectrometry, while the amorphous quality was measured via TEM as shown in fig. 4.1 showing the lack of crystalline order in both real and reciprocal space.

The magnetization as a function of applied magnetic field along the sample's normal is plotted for the samples grown at room temperature and subsequently annealed in fig. 4.2. As the annealing temperature increases a decrease in coercivity is observerd, while the saturation magnetization remains constant. This indicates that no phase segregation or compositional inhomogeneities have been introduced by annealing since these would degrade the magnitude of the magnetization.

The magnetization loops for the samples grown at different substrate temperatures are shown in fig. 4.3. Increasing the growth temperature does not seem to have a drastic effect on the coercivity. The constant saturation magnetization across the three different growths is a good indicator of the reproducibility of atomic composition and good compositional homogeneity.

Compositional homogeneity is further confirmed by the near-constant compensation temperature of the films. Shown in fig. 4.4 is the remanent magnetization as a function of temperature,

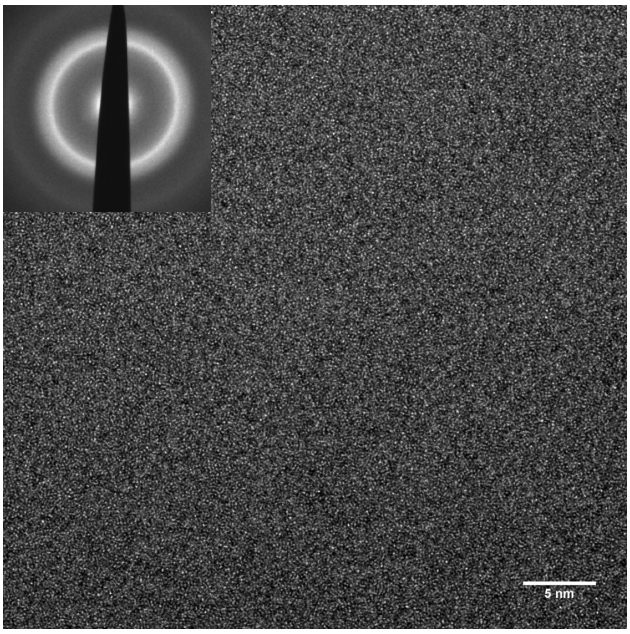

Figure 4.1: High-resolution TEM image of 30 nm of a-$Tb_{16}Co_{84}$ after annealing at 350 ^{o}C. No visible lattice fringes are observed, nor signs of nanocrystallites. The inset is the selected area electron diffraction pattern showing a diffuse halo representative of an amorphous material. The scale bar is 5 nm.

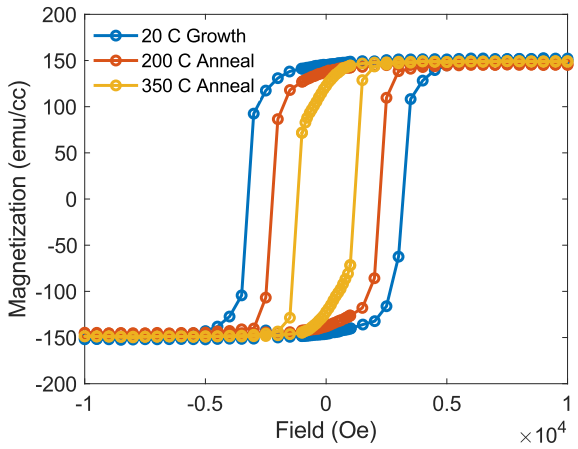

Figure 4.2: Magnetic hysteresis for the sample grown at room temperature and subsequently annealed at 200 ^{o}C and 300 ^{o}C. The coercivity decreases as a function of increased annealing temperature.

indicating that all samples have a compensation temperature of 200 K. Thus the samples' magnetization and compensation point are fairly robust against the temperature treatments applied.

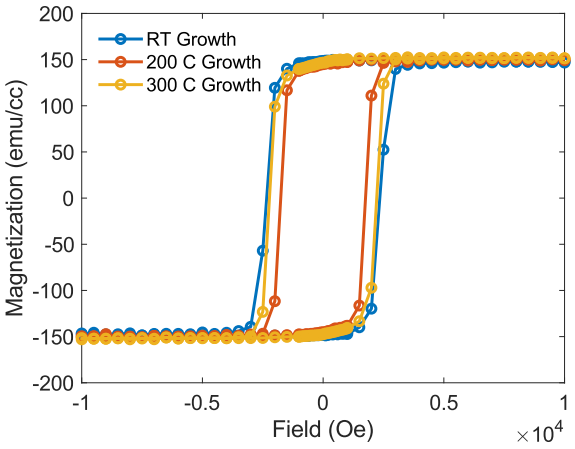

Figure 4.3: Magnetic hysteresis for the samples grown at room temperature, 200 ^{o}C and 300 ^{o}C. The hysteresis does not exhibit drastic changes as a function of growth temperature.

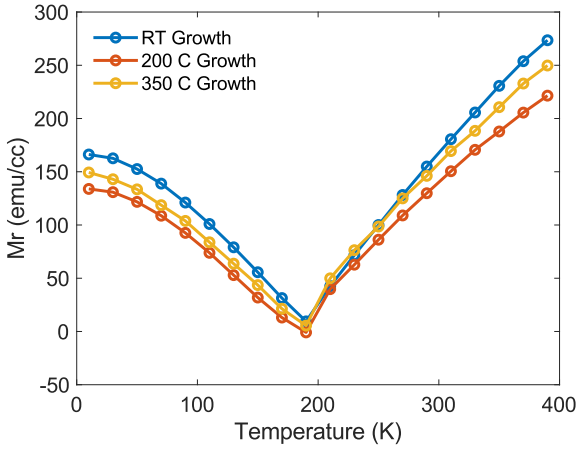

Figure 4.4: Temperature dependence of the magnetization for the samples grown at room temperature, 200 ^{o}C and 300 ^{o}C. The constant compensation temperature is indicative of compositional homogeneity. The remanent magnetization was measured after saturating the film with an applied 5 T field at every temperature point.

The intrinsic uniaxial anisotropy constant, K_{ui}, was extracted using the relation $K_{ui} = H_k M_s/2 + 2\pi M_s^2$ where H_k is the anisotropy field and M_s the saturation magnetization. The anisotropy field is measured as the field required to saturate the magnetization along the hard axis, which for these samples lies along the plane of the film. The anisotropy constants are shown in fig. 4.5 as both a function of annealing temperature and growth temperature. The samples grown at room temperature has a rapidly decreasing anisotropy constant with annealing, which can also be inferred secondarily by the reduction in coercivity as seen in fig. 4.2. The sample grown at 200 ^{o}C posseses

an anisotropy constant that is stable until the annealing temperature exceeds the growth temperature. This is consistent with previous reports [46], as well as with the model[45] that relaxations of the local atomic structure occur only once sufficient thermal energy has been provided. Finally the samples grown at the highest temperature did not receive any annealing treatment due to concerns of inducing crystallization of the sample, but it can be seen that the anisotropy constant is the greatest when the growth temperature is the highest.

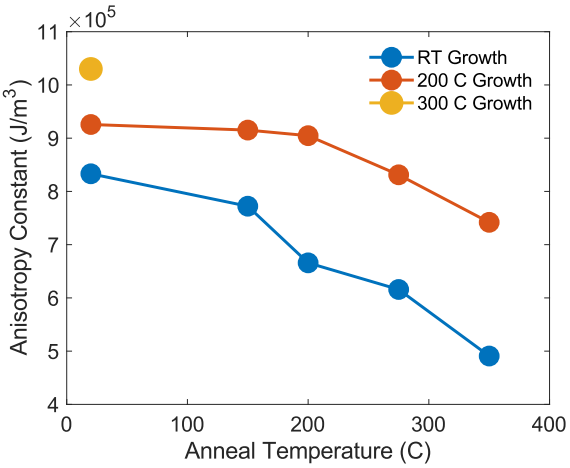

Figure 4.5: Intrinsic uniaxial anisotropy constant as a function of annealing temperature, and growth temperature.

4.3 Fluctuation Electron Microscopy

Fluctuation electron microscopy is a diffraction and/or imaging technique that quantifies medium range order in the roughly 1 to 4 nm range[47]. This method requires a converged probe with a diameter of a few nanometers to be rastered across the sample, collecting data at 5 nm intervals (in our case). The image by image variance is calculated with respect to the scattering vector (**k**), position (**r**) on the sample and probe size Q as follows:

$$V(\mathbf{k},\mathbf{r},Q) = \frac{< I^2(\mathbf{k},\mathbf{r},Q) > - < I(\mathbf{k},\mathbf{r},Q) >^2}{< I(\mathbf{k},\mathbf{r},Q) >^2}$$

The fluctuations of the intensity are maximally sensitive when the electron probe size is of comparable length to the structural MRO being probed. So the extent of MRO is quantified through the magnitude of the variance of the diffracted intensity, as a function of scattering vector over a length scale determined by the size of probe used.

FEM measurements were performed on the TEAM 1 transmission electron microscope at the National Center for Electron Microscopy at Lawrence Berkeley National Laboratory. The microscope was operated in scanning transmission electron microscopy (STEM) mode with an accelerat-

ing voltage of 300 kV. The microscope was operated with three condenser lenses in the nano-probe mode, with a 10 μm aperture, and a convergence angle of 0.91 mrad. The probe was measured in real space to have a full width half maximum diameter of 1.47 nm. At this probe resolution the resulting diffraction patterns from amorphous Tb-Co take the form of speckly distributions of diffracted intensity as depicted in fig. 4.6a – as is typical of such FEM experiments – as opposed to the diffuse rings that are conventionally associated with diffraction from larger volumes of amorphous materials seen in fig. 4.6b. Note that simply adding up many speckle patterns from different regions would produce a pattern like that in fig. 4.6b.

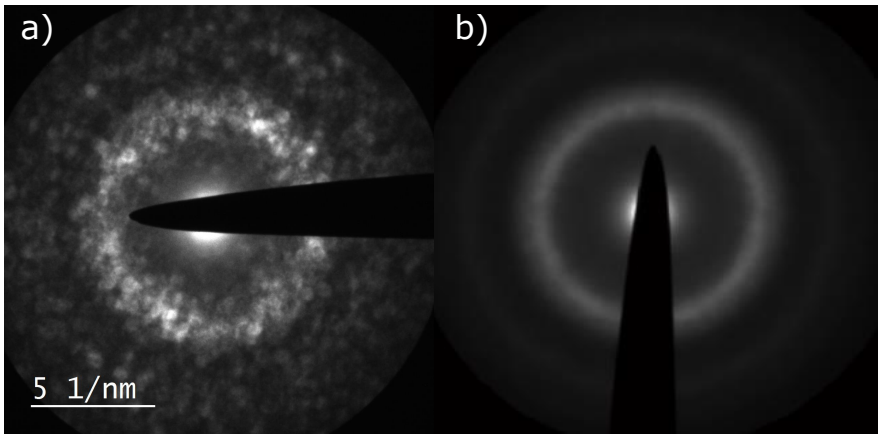

Figure 4.6: a) Typical a-$Tb_{16}Co_{84}$ FEM diffraction pattern using a 1.47 nm probe. b) typical a-$Tb_{16}Co_{84}$ diffraction pattern using a 20 nm probe.

Fig. 4.7a shows the results of the average variance of five data sets, each using $\sim$ 1000 diffraction patterns, computed for the samples grown at room temperature, 200 ^{o}C and 350 ^{o}C, with the error bars showing the standard deviation of the variance computed over the five data sets. The data confirms both the presence of MRO by the existence of a peak, and changes in MRO by the magnitude of the peak; indicating that local atomic structures are changing as a consequence of growth temperature. However, as can be seen in fig. 4.7b, the Ta controls reveal that a fairly significant overlap of the peaks of Ta and Tb/Co is occurring. Therefore although it is true that the MRO is increasing as seen by the increase of the variance, it cannot be ascertained whether this MRO contribution is coming from both Ta and Tb-Co or exclusively from the film or the capping.

Thus although Ta is a good capping material that grows amorphous and prevents oxidation, its high Z number is similar to Tb and it yields overlapping peaks in the variance data. Alternative capping layers such as Al and Pt were attempted, but these resulted in worse spectra since both Al and Pt grow polycrystalline and their sharp diffraction spots overwhelm the faint speckle pattern.

The ideal capping material for FEM then is one that grows amorphous and has a Z number far removed from the elements under study. A new series of samples were grown as before, but capped with SiN_x, a material that grows amorphous at room temperature and has a low Z number. The samples were grown at room temperature, 200 ^{o}C and 300 ^{o}C, and capped with 10 nm of SiN_x at room temperature after waiting one hour under vacuum. For these new samples the annealing

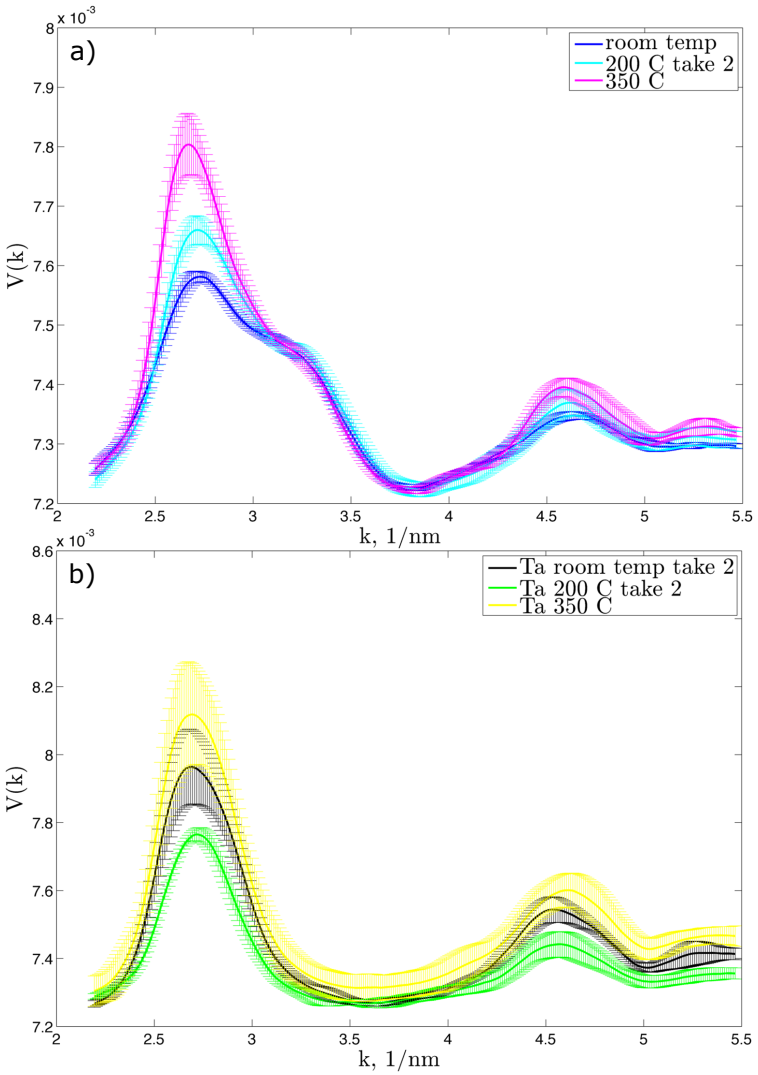

Figure 4.7: a) Comparison of the variance of the a-$Tb_{16}Co_{84}$(30)/Ta(7) series grown at different temperature. b) Comparison the variance of the accompanying 7 nm thick Ta controls grown at the same temperatures as the Tb-Co films. Clearly the Ta peaks overlap with those of the samples. The error bars correspond to the standard deviation.

study was not possible at first as it was discovered that annealing results in the formation of silicides that have a paramagnetic contribution to the magnetization, modify the composition of the underlying a-$Tb_{16}Co_{84}$ and are thus riddled by inhomogeneities. To circumvent this issue another set of samples was grown and annealed before capping with silicon nitride, this study is currently underway. The SiN_x was deposited at room temperature, to prevent the formation of silicides. The SiN_x was grown using RF sputtering, and it appears to be nitrogen-deficient as evidenced by the higher than usual levels of N_2 present in the sputtering chamber after deposition as measured with

a residual gas analyzer.

The variance data of the SiN-capped set of films is shown in fig. 4.8. Since MRO is proportional to the magnitude of the peak in the variance, it can be seen that the MRO is increasing with increasing growth temperature, indicating that the sample is acquiring a more ordered structure, even though conventional TEM imaging such as that shown in fig. 4.1, shows an amorphous structure in both real and reciprocal space. Therefore the sensitivity in FEM permits better discrimination of the amorphous quality in a sample by measuring the MRO, which allows for a correlation between structure and magnetic anisotropy to be established. In this case, the high temperature growth leads to a higher MRO which is correlated with a higher magnetic anisotropy. Qualitatively, it can be concluded that the sample grown at RT is more amorphous than its higher growth temperature counterparts, and because it is more structurally isotropic the magnetic anisotropy is smaller.

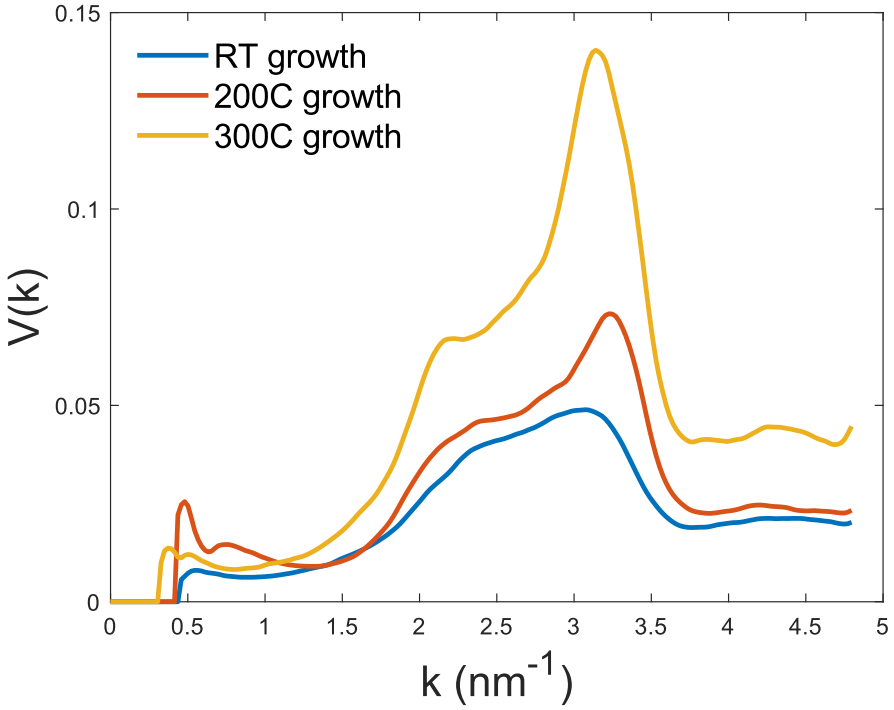

Figure 4.8: Variance data of a-$Tb_{16}Co_{84}$(30)/SiN(10) grown at room temperature, 200 ^{o}C and 300 ^{o}C.

FEM scans were also performed as a function of angle as measured from the normal of the film's plane. This helps identify if there are directions in the film that exhibit higher MRO than others. The results of the variance as a function of tilt angle are presented in fig. 4.9. Fig. 4.9a corresponds to the sample grown at room temperature and it can be seen that the variance is very stable as a function of tilt angle, with a minimum variance found at 40 degrees, meaning that the MRO is lower as more of the in-plane atomic structure is probed. Fig. 4.9b is the variance of the sample grown at 300 ^{o}C, and it can be seen that minimal variance is again observed at 40 degrees,

indicating that the in-plane atomic structure is more homogeneous than the out of plane as seen in the room temperature growth sample. Interestingly, in both samples a maximum of the variance is observed at a tilt angle of 10 degrees, indicating that the MRO is highest along that direction. This could be supportive of the EXAFS work[48] that established a pair-correlation of Tb and Fe atoms along the growth direction, except that this work presents finer angular resolution than the EXAFS measurements which were only done at 0 and 90 degrees.

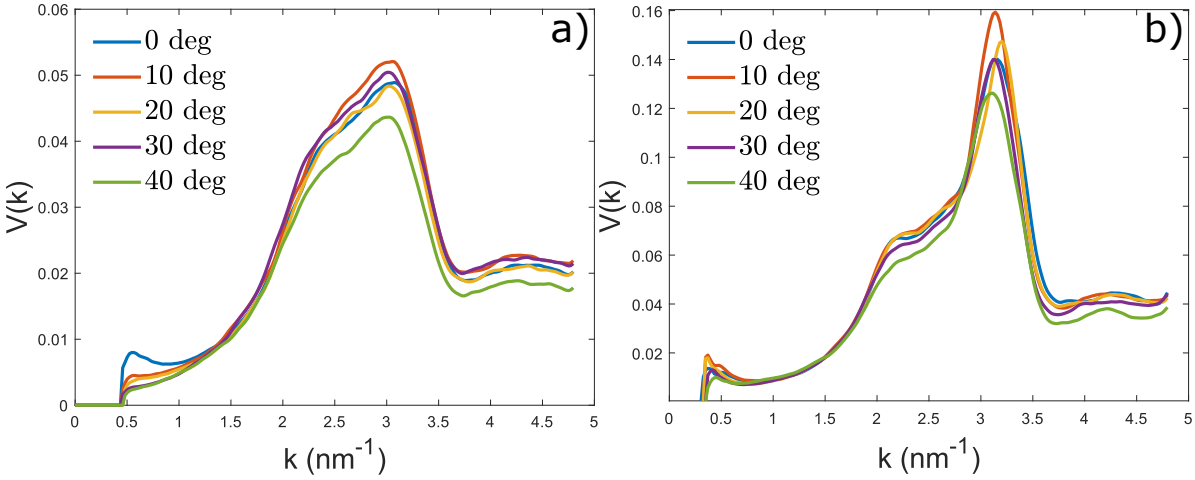

Figure 4.9: Variance data of a-$Tb_{16}Co_{84}$(30)/SiN(10) taken at tilt angles from 0 - 40^o for the samples grown at room temperature (a), and 300 ^{o}C (b).

Thus it is very possible that FEM is confirming this pair-ordering by indicating that there is a higher MRO at 10 degrees than any other direction probed, and that the in-plane atomic structure is less ordered. Therefore this asymmetry of order can be used to explain the PMA in these alloys. As to why 10 degrees is higher in MRO and not 0 degrees, this could be a consequence of the geometry of the sputtering guns during the growth. The high sensitivity to the in plane vs out of plane MRO of this technique may enable an improved understanding of the effects of vapor deposition on the structure of amorphous films.

4.4 Conclusion

FEM measurements of a-$Tb_{16}Co_{84}$ revealed a distinct difference in MRO as a function of growth temperature and tilt angle. It was shown that the material becomes more ordered as the growth temperature increases, and it orders along a specific direction: normal to the film's plane. This preferential ordering along the growth direction correlates with the higher anisotropy constants found in these samples, and are consistent with the models and measurements of the early 1990s. Angle-resolved FEM is a powerful technique that could usher a new paradigm in the structural characterization of amorphous materials.

Chapter 5

Coexistence of soft and hard magnetic phases in single layer amorphous Tb-Co thin films

Amorphous(*a*-), ferrimagnetic Tb-Co thin films prepared with a thin Ta underlayer and either a Ta or Pt overlayer show evidence of both a soft and a hard magnetic phase despite no sign of this at room temperature. Low temperature magnetometry measurements reveal the decoupling of the two magnetic phases with decreasing temperature due to increased anisotropy energy of the hard layer at lower temperatures.Decreasing the film thickness to 2 nm, slightly above the superparamagnetic limit found at 1 nm, a soft, low density phase was isolated and found to be present in all the films as confirmed with x-ray reflectivity (XRR) and Rutherford backscattering spectrometry (RBS) measurements. For greater thicknesses, the bottom layer retains its soft magnetic nature, while the remainder of the film is denser and has strong perpendicular magnetic anisotropy, leading to exchange-spring behavior when the anisotropy becomes large, either at low temperatures or via a Pt overlayer which adds a strong interfacial anisotropy to the layer. Micromagnetic simulations reproduced the experimental hysteretic behavior by incorporating the experimentally-determined anisotropy and magnetization parameters into a soft/hard bilayer model. The Pt capping layer produces a slightly larger anisotropy constant than the Ta capping.

5.1 Introduction

With the increasing pressures for faster, denser and more energy-efficient magnetic data and logic devices comes the necessity to study reduced dimensions and interfacial phenomena in magnetism. Amongst the many magnetic materials being proposed, ferrimagnetic rare-earth (RE) - transition metal (TM) alloys have received increased attention due to their wealth of magnetic properties, situating them at the center of many proposed magnetic devices. Studies of these systems include spin-orbit torque measurements of ferro(i)magnet/heavy metal (HM) bilayer systems;[49, 50, 51, 52, 53] imaging of exotic spin textures such as skyrmions in multilayered HM/RE-TM alloys,[54]

and ultrafast magnetization dynamics in Gd-Fe-Co and Gd-Co alloys.[55, 56, 57, 58, 59] All of these studies take advantage of amorphous RE-TM alloys' growth-induced perpendicular magnetic anisotropy (PMA), relatively high Curie temperature, and tunability of their magnetic properties, including the magnetic anisotropy, dipole coupling, coercivity, Dzyaloshinskii-Moriya interaction, damping and spin-orbit coupling by modifying the composition, growth temperature, anneal temperature and interfacial engineering.[46, 60] This tunability makes these systems highly desirable testbeds at the forefront of applied and basic research.

The amorphous structure of these RE-TM alloys introduces an added challenge when it comes to characterizing the structure of ultra thin films. In addition, at a given point certain film thicknesses cannot be achieved without reaching undesirable thresholds such as the superparamagnetic limit, and at other points it can become difficult to distinguish a film from an interface.

This study shows that amorphous, ferrimagnetic Tb-Co thin films which appear to be regular ferrimagnets at room temperature, exhibited unexpected magnetic hysteretic behavior at low temperatures. This result is shown to be due to the coexistence of a low density/high density bilayer arising from growth effects.

5.2 Thin Film Growth and Magnetic Characterization

The samples consist of trilayers of Ta(2 nm)/*a*-$Tb_{18}Co_{82}$(*t* nm)/Pt or Ta (7 nm) with *t* ranging from 2 to 16 nm for the Ta-capped samples, and 2 - 4 nm for the Pt-capped samples. The thin films were deposited using a confocal DC magnetron sputtering system by co-sputtering separate Tb, Co, Ta and Pt targets. All samples were grown at room temperature in 1 mtorr of Ar and a base pressure of 8 x 10^{-8} torr at a growth rate of $\sim$ 1.0 *Å*/s. Samples were grown on 300 nm of amorphous SiN_x on Si substrates and were determined to be amorphous via electron diffraction in a TEM. The magnetic properties of the films were studied using a SQUID magnetometer in a temperature range of 10-400 K, the layer thickness and densities were determined via XRR and RBS, and the films' chemical composition was measured to be 18 at.% Tb, 82 at.% Co via RBS. At this composition the samples possess a compensation temperature of $\sim$ 150 K; at room temperature the net magnetization is parallel to the Co sublattice and is said to be Co-dominant, while below 150 K the magnetization is Tb-dominant.

Figure 5.1 shows the out of plane (OOP) magnetic hysteresis for all samples. At 300 K every sample exhibits hysteretic behavior indicative of a homogeneous magnetic film. However upon decreasing the temperature to 100 K a step in the hysteresis is observed which is indicative of the coexistence of a decoupled soft and a hard magnetic phase. All samples exhibit this low temperature step except for the Ta-capped 2 nm film as shown in fig. 5.1b. The magnitude of the step in the hysteresis is significantly reduced in the Ta-capped 8 and 16 nm samples as seen in fig. 5.1e and fig. 5.1f respectively. This will be shown to be associated with a soft magnetic layer that is unaffected by the total film thickness. Fig. 5.1a and fig. 5.1d show the magnetization of the Pt-capped samples which show similar behavior to their Ta-capped counterparts. These measurements also show that the coercivity increases with decreasing temperature and that the films possess perpendicular magnetic anisotropy.

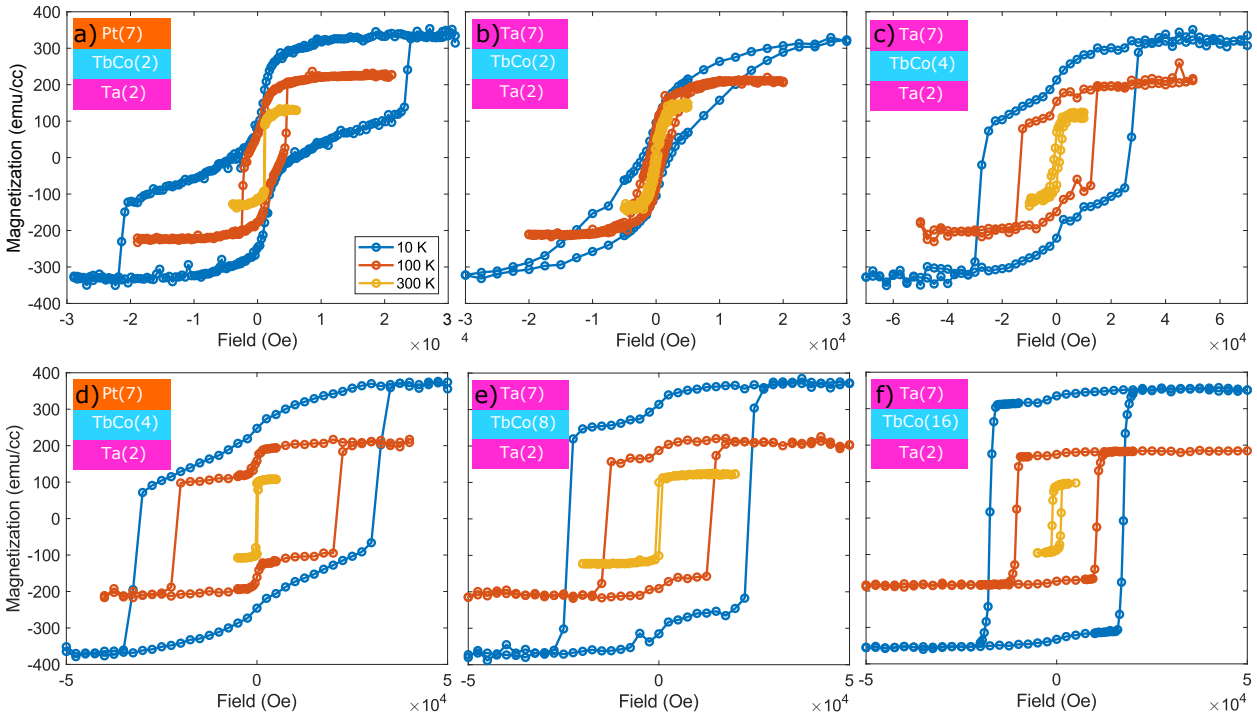

Figure 5.1: Out of plane magnetization hysteresis for a-$Tb_{18}Co_{82}$ samples at room temperature (yellow), 100 K (orange) and 10 K (blue). a) and d) correspond to the 2 and 4 nm Pt-capped samples while b),c),e) and f) correspond to the 2 - 16 nm Ta-capped samples respectively. Coercivity increases with decreasing temperature and steps are seen in all samples at 10K except the 2 nm film, in some at 100K, and in none at 300K.

The in-plane (IP) and OOP magnetization loops of the Ta-capped 2 nm film at 10 K are shown in figure 5.3. It reveals that unlike all other samples in this study, this sample possesses no effective magnetic anisotropy as it has no preferred magnetization direction. Film thickness of 1 nm results in superparamagnetism as shown in fig. 5.2, at 2 nm the film overcomes the superparamagnetic limit. However, despite achieving ferromagnetic order the sample lacks the strong PMA seen in the other samples as shown clearly in figure 5.4.

The intrinsic anisotropy constant (K_{ui}) is extracted from IP and OOP magnetization measurements using the relation $K_{ui} = H_k M_s/2 + 2\pi M_s^2$ where H_k is the anisotropy field and M_s the saturation magnetization. It is seen that the anisotropy is influenced by three factors: increasing film thickness increases PMA, decreasing temperature increases PMA, and capping with Pt slightly enhances the PMA. The zero effective anisotropy seen in the Ta-capped 2 nm sample is not due to K_{ui} being zero, but rather to K_{ui} being very close in value to the shape anisotropy energy.

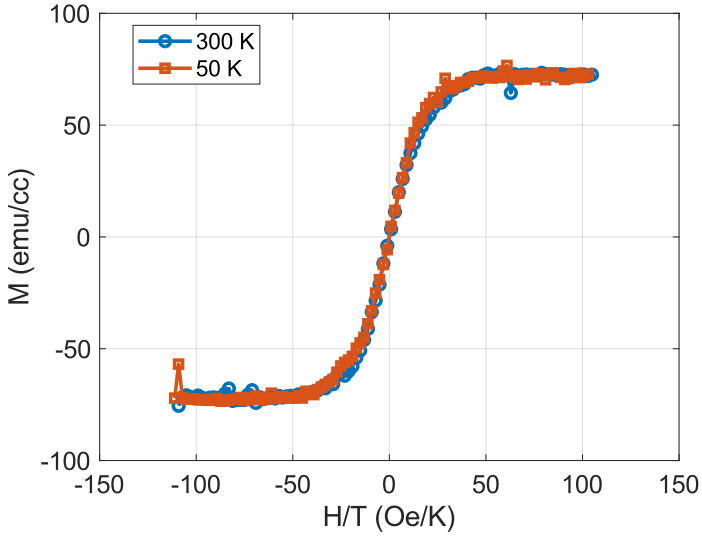

Figure 5.2: Magnetization curves at 300 K and 50 K of a 1 nm thick *a*-$Tb_{18}Co_{82}$ film. The lack of a remanence and zero coercivity in addition to the mutual collapse of both curves as a function of H/T are clear indicators that the sample is superparamagnetic.

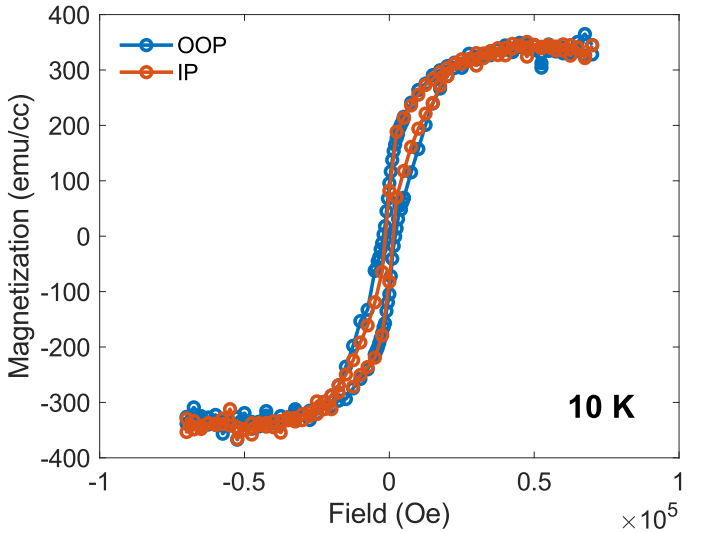

Figure 5.3: Out of plane and in plane magnetization loops of the Ta-capped 2 nm sample shows no effective magnetic anisotropy, meaning that shape anisotropy is balanced by an intrinsic growth induced PMA of magnitude approximately 7 x 10^5 ergs/cc.

5.3 XRR and RBS Structural Characterization

Structural characterization via XRR allows determination of sample thickness, roughness and density. XRR measurements were conducted with a PANalytical X-Ray diffractometer (Cu-kα radi-

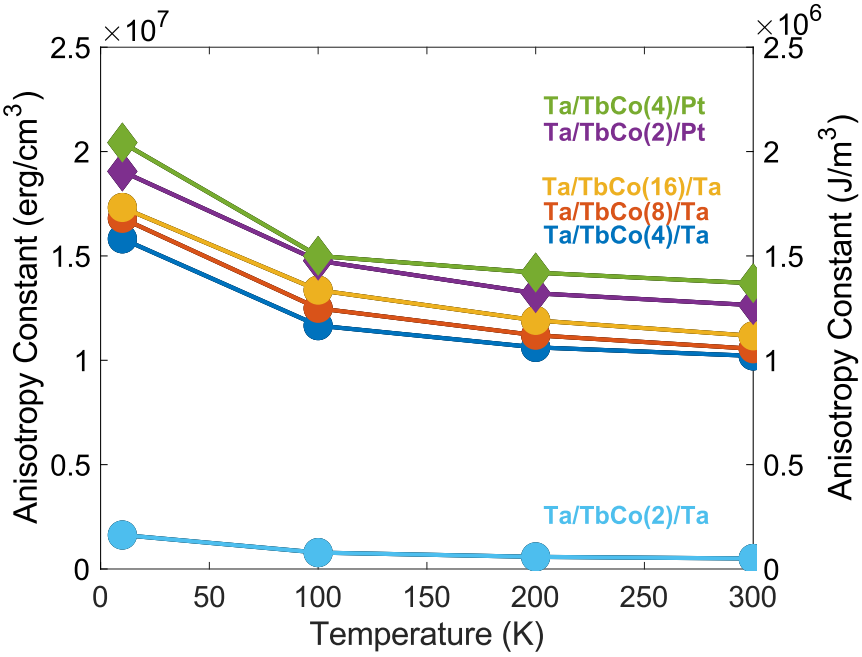

Figure 5.4: Intrinsic anisotropy constant (Kui) as a function of temperature. Decreasing the temperature results in increased PMA. PMA also increases with film thickness as well as by capping with Pt as seen in the Pt-capped series.

ation, 0.154 nm). XRR curves were analyzed using the GenX software,[61] in which a layered model of the samples is composed as input and the GenX program varied the thickness, roughness and density of each layer until the difference between the simulation and the experimental data was minimized. For the Ta-capped samples the layered model consisted of air/TaO_x/Ta/*a*-Tb-Co/Ta/SiN whereas for the Pt-capped samples it consisted of air/Pt/TbCo/Ta/SiN. Figure 5.5 shows the XRR curve of the Ta-capped 4 nm sample and its accompanying simulation. Fig. 5.5a presents the simulation done with a single layer of *a*-Tb-Co and it is evident that it does not yield a very good fit. Fig. 5.5b shows the result of simulating a bilayer consisting of a lower density bottom layer and a higher density top layer of *a*-Tb-Co, resulting in a much improved fit. This bilayer approach had to be implemented in all films except for the 2 nm Ta-capped and Pt-capped samples in order to achieve good fits. Comparing the densities of the bottom layers across all samples revealed that the bottom layer was always $\sim$ 2 nm thick with a density that matched that of the 2 nm films as will be discussed below.

To further characterize the low/high density bilayer the samples were probed with RBS. RBS uses MeV helium ions to depth profile information about a thin film. The helium ions recoil from classical collisions with the film's atoms, and the energy of the recoiled atoms can be modeled to tell the atomic composition and thickness or density of a thin film. Either thickness or density is required for proper RBS fitting and calculating density requires a precise measure of a film thickness which in this case is provided by the XRR analysis. Thus XRR and RBS are very

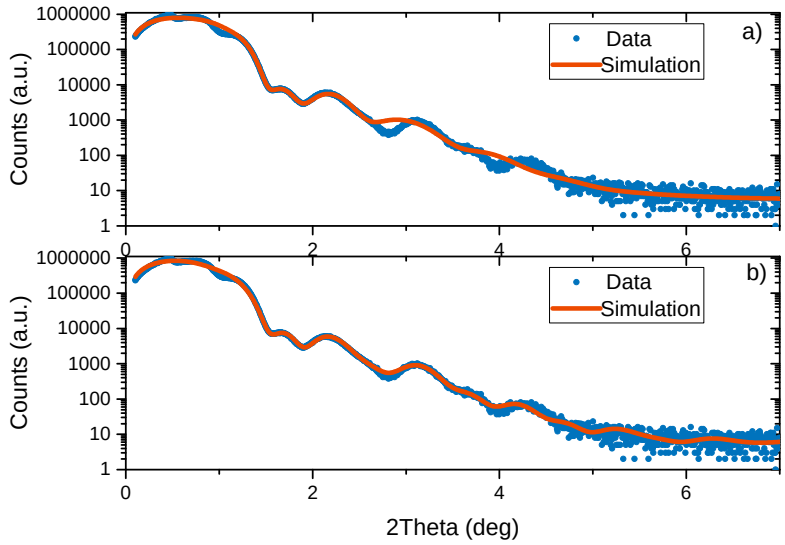

Figure 5.5: XRR measurements on the Ta-capped 4nm sample. a) Shows the inadequate fitting resulting from using a single 4 nm Tb-Co layer. b) Shows the improved fit when breaking the nominal 4 nm Tb-Co film into a bilayer of different atomic densities.

	XRR			RBS	AFM
Ta-capped Stack	Thickness (nm) Lower layer/Top layer	Roughness (nm) Lower layer/ top layer	Density (10^{22} at/cm3) Lower layer / Top layer	Density (10^{22} at/cm3) Lower layer/ Top layer	Roughness (nm)
2 nm	1.6 ± 0.3	0.54 ± 0.07	5.1 ± 0.4	4.9 ± 0.7	0.49 ± 0.07
4 nm	$1.4 \pm 0.3/2.2 \pm 0.2$	$0.41 \pm 0.08/0.52 \pm 0.06$	$4.9 \pm 0.4/6.2 \pm 0.3$	5.5 ± 0.3	0.45 ± 0.06
8 nm	$1.6 \pm 0.3/6.2 \pm 0.2$	$0.47 \pm 0.09/0.53 \pm 0.08$	$5.2 \pm 0.4/5.1 \pm 0.4$	$5.1 \pm 0.5/5.9 \pm 0.2$	0.39 ± 0.05
16 nm	$1.5 \pm 0.3/14.2 \pm 0.2$	$0.49 \pm 0.06/0.56 \pm 0.07$	$5.0 \pm 0.4/6.2 \pm 0.4$	$4.9 \pm 0.3/6.0 \pm 0.2$	0.54 ± 0.07
Pt-capped Stack					
2 nm	1.8 ± 0.3	0.53 ± 0.08	4.9 ± 0.4	5.0 ± 0.5	0.41 ± 0.06
4 nm	$1.4 \pm 0.3/2.3 \pm 0.3$	$0.42 \pm 0.07/0.57 \pm 0.08$	$5.21 \pm 0.4/6.0 \pm 0.4$	5.6 ± 0.3	0.52 ± 0.05

Table 5.1: The thickness, roughness and density of the *a*-Tb-Co bilayers as obtained from XRR. Densities obtained from RBS are consistent with those found with XRR and confirmed the presence of a low density/higher density bilayer. The RMS surface roughness measured in AFM is consistent with that obtained via XRR.

complementary and powerful techniques. The RBS spectra was taken in the Cornell geometry with a 3 MeV He^{4+} ion beam incident at 35^o from the sample's normal. Higher angles of incidence were tested in order to improve the surface sensitivity but it was found that the Ta or Pt peak considerably overlapped with the Tb peak. Thus 35^o was chosen as the optimal angle of incidence. The RBS spectra was analyzed using the SIMNRA software[62] and the densities from both XRR and RBS are plotted in fig. 5.7, where the "bottom" and "top" labels denote the separate densities of the

bilayer. To obtain the density from RBS the SIMNRA simulation's areal density was divided by the film thickness as extracted from XRR. The XRR bilayer thickness, roughness and density are tabulated in Table 5.3 as well as the RBS density and RMS surface roughness as measured with an atomic force microscope (AFM) as seen in fig. 5.6. Note that the RMS roughness is of the film's surface as measured via AFM, and since the capping layer of these samples is 7 nm the images are depicting the microstructure of the Ta and Pt capping layers, and are not representative of the microstructure of Tb-Co. The XRR roughnesses reported in Table 5.3 correspond to the top interfaces of the Tb-Co bilayers. So the roughness of the lower layer belongs to the interface between the lower and top Tb-Co layers, while the roughness reported for the top layer is that of the interface between the top layer and the capping (Ta or Pt) layer. Neither of which is probed by the AFM images. Nonetheless there is good agreement between the two techniques as the roughnesses reported are within 0.1 nm from each other.

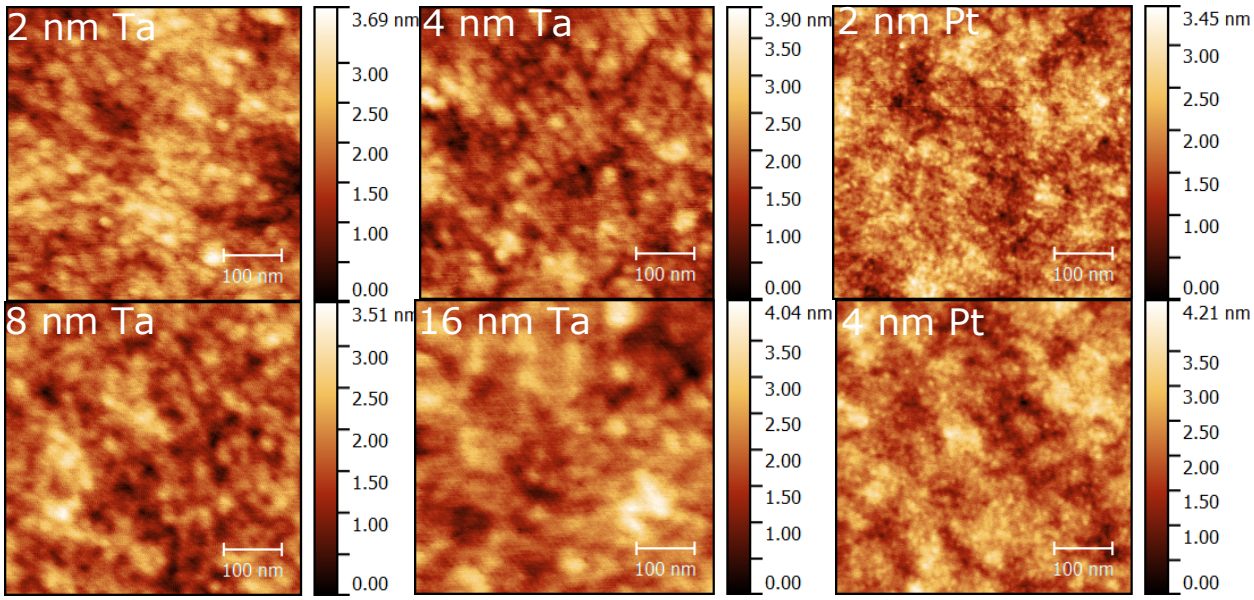

Figure 5.6: Atomic force microscopy images of the Ta-capped and Pt-capped samples depicting the microstructure of the Ta and Pt capping layers. Thinner samples are less rough, and Pt has finer grains than Ta. Ta is amorphous while Pt is nanocrystalline (determined via electron diffraction in Ch. 4) and the structure seen by AFM shows larger in plane structure for Ta than for Pt but with similar vertical roughness. These images are not representative of the microstructure of *a*-Tb-Co but the roughnesses extracted from these scans are consistent with those extracted via XRR as compared in Table 5.3.

The XRR data in fig. 5.7 shows that a bilayer was found for all samples except the 2 nm Ta-capped and Pt-capped samples, which possess a density that is similar to that found in the initial $\sim$ 2nm in all the other films as seen within the region labeled "Bottom Layer". Table 5.3I shows that the thickness of this lower density bottom layer is in the 1.4 - 1.8 nm range. The RBS data confirmed the presence of a bilayer in the 8 and 16 nm Ta-capped samples, and a single layer fit

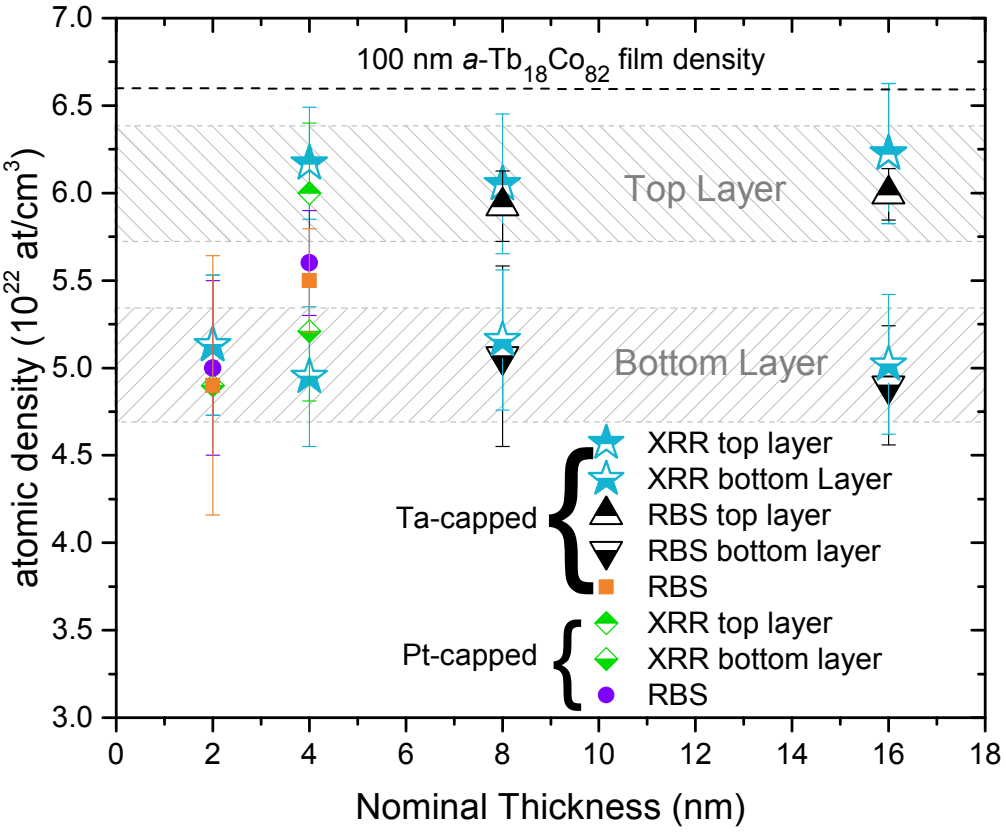

Figure 5.7: Atomic density as a function of the nominal film thickness as extracted from both XRR and RBS. The rectangular regions are guides to the eyes to show the agreement of both XRR and RBS in determining the film density and confirming the bilayer model. The RBS density of the 4 nm samples lies between the two regions because it is averaging the low/high density values of the bilayer as discussed in the main text. Points labeled "RBS" indicate that a single layer was used for the fitting.

was sufficient for the Ta-capped and Pt-capped 2 - 4 nm samples. The density extracted from RBS, is in good agreement with the density found via XRR. The RBS density found for the 4 nm samples is in between that found with a bilayer model in XRR, suggesting that a bilayer is present and its densities are being averaged in RBS. Both XRR and RBS also found a near constant density for the top layer, as seen in the gray box labeled "Top Layer" depicting a somewhat flat density trend with increasing film thickness. The dotted line at the top of fig. 5.7 is the measured density of a 100 nm thick a-$Tb_{18}Co_{82}$ film showing that the density increases slightly with increasing thickness.

5.4 Micromagnetic Simulations

A soft/hard bilayer is a common recipe for exchange-spring systems which have aroused much interest in the past two decades because of their potential in achieving giant energy products as well as their rich variety of magnetic behaviors.[63, 64, 65, 66, 67]. Exchange-spring systems are based on interfacial exchange coupled soft and hard ferromagnetic nanocomposites or layers, that combine the high magnetization of the soft phase with the high anisotropy of the hard phase to attain a high energy product. Micromagnetic simulations that incorporate the anisotropy and magnetization values measured at 10 K were done using the MuMax3 software[68] in order to verify that a soft/hard bilayer system is responsible for the observed step in the hysteresis.

The modeled system consisted of two cylinders of 40 nm in diameter and a fixed thickness of 2 nm for the bottom cylinder to represent the low density layer, and variable thicknesses for the upper layer ranging from 2 - 14 nm. The 40 nm diameter is based on the average grain size as measured via AFM on an uncapped 2 nm thick a-$Tb_{18}Co_{82}$ film as shown in fig. 5.8. A cell size of 2 nm was chosen in the x and y directions which correspond to the plane of the face of the cylinder, while a cell size of 0.5 nm was chosen for the z direction in order to better resolve the dynamics through the thickness of the film. The two regions were modeled to have the same values of $M_s = 4 \times 10^5$ A/m, and exchange stiffness $A_{ex} = 1 \times 10^{12}$ J/m and differed only in the anisotropy constant; with the upper layer having a uniaxial anisotropy constant equal to that measured in fig. 5.4 at 10 K and the bottom layer was given a value of zero effective anisotropy, as measured in the 2 nm film at 10K. The results of the effect of anisotropy constant on the magnetization reversal for the thinnest bilayer are shown in fig. 5.9a, illustrating that as the anisotropy energy increases the soft/hard bilayer decouples and results in the step in the hysteresis. The inset of fig. 5.4a shows the side and bottom view of the modeled bilayer which shows that reversal occurs by curling of the magnetization, also known as a magnetic vortex.

The effect of increasing thickness of the top, higher density layer is seen in fig. 5.9b, where the magnitude of the step is reduced as the top layer's thickness t is increased, in complete agreement with the magnetization measurements of fig. 5.1e and 5.1f.

Since the soft and hard phases are only exchange coupled at the interface, the reorientation of the soft, low density layer should be fully reversible for fields below the switching field of the hard layer. This is the namesake of the "exchange-spring" term, indicating that as long as the applied field is below that of the hard layer, the magnetization of the soft layer will spring back to orient itself with the hard phase once the field is removed. In order to confirm that the soft/hard bilayer found in the films make up an exchange-spring system, magnetization recoil curves were measured. Recoil curves are obtained from the successive removal to remanence and reapplication of an increasingly negative field from the major demagnetization. The recoil curves shown in fig. 5.10 were measured on the Pt-capped 4 nm a-$Tb_{18}Co_{82}$ sample, and illustrate that the soft layer is reversible as expected of an exchange-spring system. The inset zooms into the reversible region and shows that there is slight hysteretic behavior as the applied negative field increases. As reported in [66], the source of the hysteresis is likely due to reversal of the polarity of the magnetic vortex that forms according to the micromagnetic results depicted in fig. 5.9a. Although this system falls short from the best exchange-systems recorded, it is nonetheless quite interesting that such an

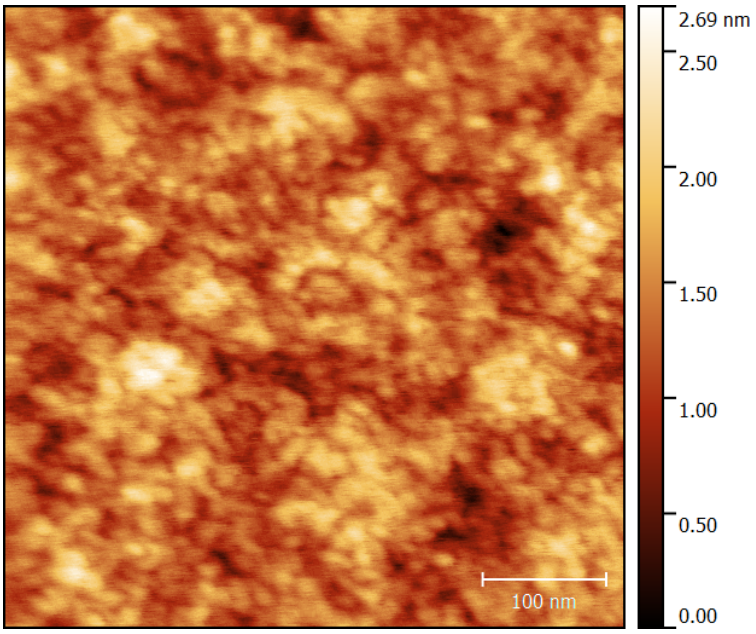

Figure 5.8: AFM scan of an uncapped 2 nm thick *a*-$Tb_{18}Co_{82}$ film. Sample was measured 30 minutes after deposition which is enough for oxidation to occur and may affect the microstructure. The Ta and Pt cappings were 7 nm thick on the main samples studied, so their AFM scans are not representative of the microstructure of *a*-Tb-Co.

esoteric phenomenon would arise in a film meant to be a single, homogeneous single layer.

5.5 Discussion

The successful reproduction of the experimental hystereses via micromagnetic simulations of a soft/hard bilayer, in conjunction with the density findings from XRR and RBS, leads to the following interpretation of the growth effect. The initial couple of nanometers of the film deposition grow at a lower density which leads to a magnetically soft phase. As the growth progresses the film densifies and acquires the more typical magnetic behavior of ferrimagnetic RE-TM alloys. The bilayer model is an approximation of what is bound to be a more gradual change as the deposition progresses. It is very likely that this type of growth effect is present in many other systems but its effects remain hidden due to experiments at room temperature, where the anisotropy is low enough to couple both phases so the magnetization reverses coherently and often on thicker films. This model accounts for the formation of the step in all films except for the 2 nm Pt-capped, which exhibits a formidable step at low temperatures. It is quite possible that the Pt interface is responsible for the formation of the step. Since it was seen that both Pt-capped samples exhibit higher anisotropy than the Ta-capped ones, likely due to the Tb-Co/Pt interface. Thus the bilayer here would consist of soft Tb-Co and a hard Tb-Co/Pt interface. In the Pt-capped 4 nm sample, three

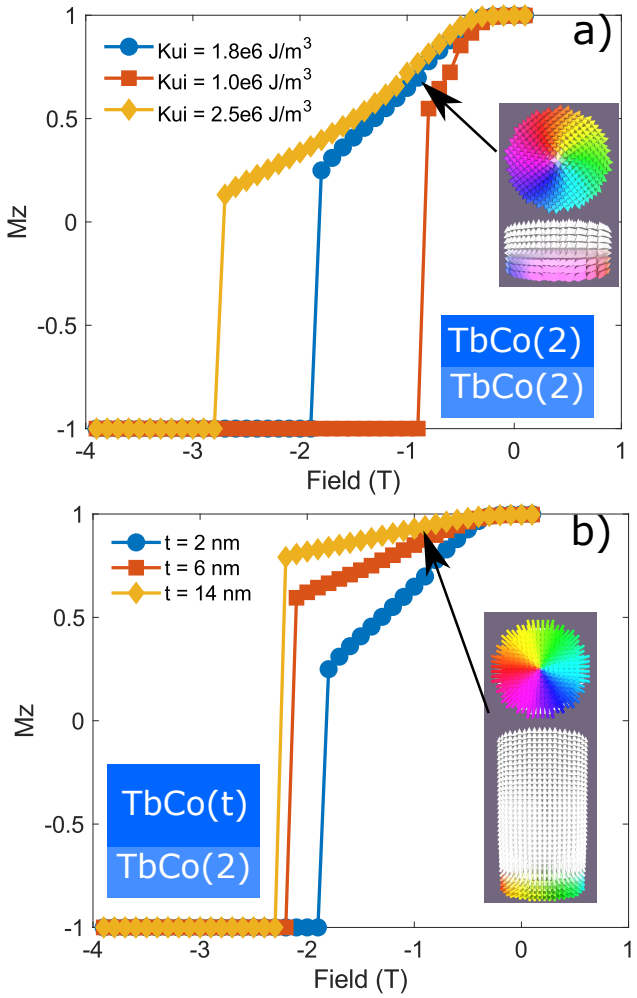

Figure 5.9: a) Magnetization along the z-component (OOP orientation) as a function of increasingly negative applied field for different values of anisotropy constant in a soft/hard bilayer of equal thickness. The inset depicts the domain structure at an applied field of -0.9 T and shows a magnetization reversal process occurring via curling of the magnetization as seen from both the side of the cylinders and from the bottom. b) The effect of increasing top layer thickness with a fixed uniaxial anisotropy constant of 1.8 x 10^6 J/m^3. The inset shows that magnetization reversal initiates via curling of the soft phase. Depicted is the side and bottom view at an applied field of -0.9 T for film thickness of 16 nm.

steps are not observed because both the hard Tb-Co and the hard Tb-Co/Pt phases are close enough in anisotropy to reverse together.

Tthere are several non-exclusive possibilities for the causes of the lower density initial layer. It is not uncommon for the initial layer of growth to show a reduced density, as the film grows by coalescence. A substrate effect could also be responsible, with the initial Tb-Co atoms seeing a

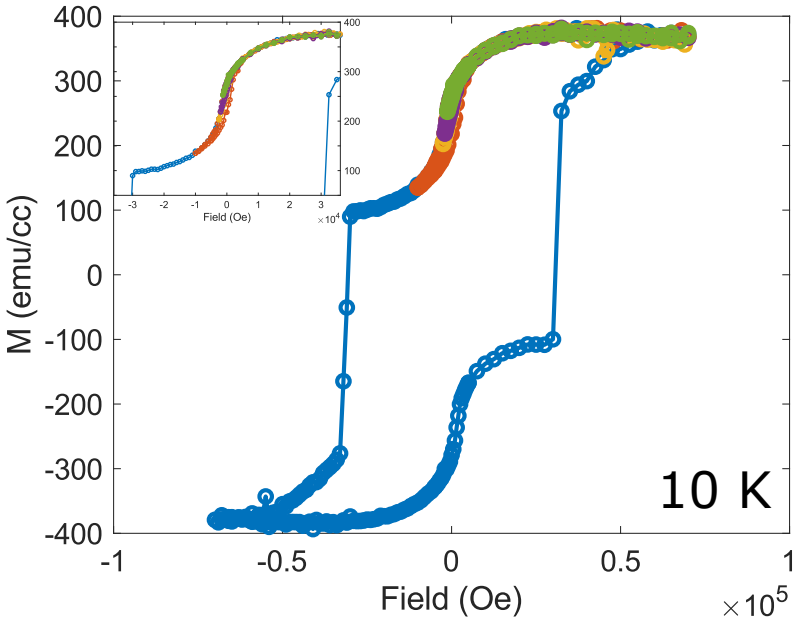

Figure 5.10: Magnetization recoil curves illustrating the hysteretic reversal of the soft, low density 4 nm Pt-capped a-$Tb_{18}Co_{82}$ layer at 10 K. Inset: Magnification of the reversible region.

different energy landscape upon arrival to the substrate than the next layer.

5.6 Conclusion

In conclusion, the coexistence of a soft/hard bilayer in compositionally homogeneous, single layer, amorphous, ferrimagnetic Tb-Co thin films has been found to arise from a growth effect that creates a low density/high density bilayer which behaves as an exchange-spring magnet at low temperatures. The lower density bottom layer is magnetically soft, and for film thickness near 1 nm, the film is superparamagnetic. For film thickness near 2 nm, the film is a soft ferromagnet. For thicker films, the 2 nm thick lower soft ferromagnet continues to influence the overall magnetic properties, causing steps in the magnetic hysteresis loops at temperatures below room temperature when the anisotropy of the hard layer becomes large. XRR and RBS provided direct structural evidence of this bilayer structure for all films thicker than 2 nm. This hidden low density layer is likely present in many other material systems, but the associated soft and hard magnetic phases will decouple only when the difference in anisotropy energy is large enough, which typically occurs at low temperatures only. The presence of a Pt interface enhances the anisotropy constant.

Chapter 6

Ultrafast magnetization dynamics in *a*-Gd-Tb-Co alloys

Amorphous (*a*-) ferrimagnetic $Gd_{22-x}Tb_xCo_{78}$ thin films with perpendicular magnetic anisotropy show ultrafast helicity-independent all-optical switching (HI-AOS) from x = 0 to x = 18. Increasing Tb content causes increasing values of the magnetic anisotropy constant, slower remagnetization rates and higher critical fluences. Magnetic anisotropy and saturation magnetization do not correlate with magnetization reversal upon irradiation. The ultrafast magnetization measurements show that the dynamics of reversal are fastest in pure *a*-$Gd_{22}Co_{78}$ and progressively slow down as Tb at.% increases until only demagnetization occurs in *a*-$Tb_{22}Co_{78}$. Annealing reduces the anisotropy, increases the damping and causes slower remagnetization rates. Combined atomistic spin dynamics simulations and two-temperature model simulated and reproduced the experimental dynamics as well as the increased critical fluence required for switching. Increased damping from greater spin-orbit coupling arising from Tb's $L = 3$ value is responsible for the slower dynamics and greater critical fluence and explains why switching has not been observed in Tb-Co alloys. The high anisotropy in *a*-$Gd_{22-x}Tb_xCo_{78}$ thin films for x $\geq$ 12 makes them excellent candidates for new high-density memory devices taking advantage of ultrafast magnetization reversal mechanisms.

6.1 Introduction

The study of magnetization dynamics in the femtosecond timescale began in 1996 when Beaurepaire et al. discovered that Ni demagnetized within a ps after irradiation with a 60-fs laser pulse.[69] This was surprising since it had been observed that the characteristic time for establishing thermal equilibrium between the lattice and the spin system was on the order of 30 - 100 ps.[70, 71, 72] This discrepancy between the dynamics triggered by a thermal heat source versus those set off by a short laser pulse is what gave rise to the field of ultrafast magnetization dynamics, also known as femtomagnetism. Among the many phenomena studied in this field, the ability to all-optically switch (AOS) the magnetization is one of most promising technological developments as it could enable unparalleled read/write speeds in memory storage devices.[73, 60] Two

distinct techniques currently exist to achieve AOS. The first reverses the magnetization by using multiple circularly-polarized laser pulses and is known as helicity-dependent all-optical switching (HD-AOS). The need for multiple pulses[74] makes the overall mechanism of HD-AOS slow and energy inefficient. The second technique is independent of the laser pulse polarization and is known as helicity-independent all-optical switching (HI-AOS).[56] HI-AOS describes a thermally-induced magnetization reversal phenomenon in ps and sub-ps timescales in which a ferrimagnetic material reverses its magnetization upon being irradiated by single ultrafast laser pulses of any polarization. As it is a thermally driven process, a minimum thermal energy has to be delivered by the optical pulse in order to reverse the magnetization; this threshold value is known as the critical fluence.

The time-resolved X-Ray Magnetic Circular Dichroism (XMCD) experiments of Radu et al. revealed that the magnetic sublattices in ferrimagnetic *a*-Gd-Fe-Co reverse at different rates, with the transition metal (TM) demagnetizing at a faster rate than the rare earth (RE) following laser irradiation, raising the electron temperature above the phonon temperature.[55] Importantly, it revealed a transient, non-equilibrium ferromagnetic (FM) alignment of the TM and the RE for a few ps during the demagnetization process, after which angular momentum exchange between the RE-TM sublattices drives the reversal of the antiferromagnetically coupled sublattices. It is unclear if this transient FM state is necessary for switching[75] and a complete microscopic theory has yet to explain the intrinsic fundamental physics of this phenomenon, including addressing the apparent exclusivity of Gd in enabling HI-AOS in Gd-TM alloys. Systems exhibiting HI-AOS include Gd-Fe-Co[56, 55, 57], Pt/Co/Gd[58] and Co/Pt/Co/GdFeCo[59]. Similar RE-TM alloys and multilayers with Tb as the RE element, like *a*-Tb-Co and Tb/Co multilayers[74] have so far only shown HD-AOS, or transient reversal with a single, linearly polarized laser pulse[76], wherein the magnetization reverts back to its original direction after a short reversal of a few ps. Single-shot HI-AOS was demonstrated in *a*-Tb-Fe-Co alloys[77], but it required patterning of nanoscale antennas to enhance the optical field, thereby confining the switched region to less than 100 nm in areas near and around the antennas. Absolute spatial control of the switched area could not be achieved, and the time dynamics of the switching was not reported. Another exception to the use of Gd was found in ferromagnetic Pt/Co/Pt[78], but the magnetization dynamics occur in μs instead of ps, and switching is only seen when the laser spot size is comparable to the intrinsic domain size of the ferromagnetic film. The slower dynamics found in this system indicate that the underlying physical mechanism is distinct from that found in Gd-TM alloys. Notwithstanding this lack of fundamental understanding, HI-AOS is one of the fastest magnetic reversal mechanisms known to date and is of interest for potential applications in memory storage and communications devices. However, Gd-based alloys lead to material systems with low perpendicular magnetic anisotropy (PMA), limiting their potential for magnetic memory applications compared to more strongly anisotropic systems which allow for greater memory storage density and longer retention time.

In this work we investigate experimentally and theoretically the role of Gd in enabling HI-AOS by studying *a*-$Gd_{22-x}Tb_xCo_{78}$ thin films. By systematically varying the RE composition as well as post-growth annealing, the magnetization, anisotropy, Gilbert damping and spin-orbit coupling are modified, permitting to study their effects on the ultrafast magnetization dynamics and their

influence on HI-AOS.

6.2 Thin Film Growth and Magnetic Characterization

Amorphous, ferrimagnetic thin-films of Ta(3)/Pt(3)/*a*-$Gd_{22-x}Tb_xCo_{78}$(10)/Pt(3) (units are nm) heterostructures were grown onto substrates of Si(525μm)/SiO_2(50nm)/SiN_x(300 nm). Films that are too thin do not yield a strong signal in MOKE, and films that are too thick do not heat up homogeneously through its thickness, hindering switching. Samples were deposited at room temperature using a magnetron sputtering system by co-depositing from separate Tb, Gd and Co targets at an Ar pressure of 1 mtorr and a background pressure of 6×10^{-8} torr. Layer thicknesses were monitored with a quartz mass balance during growth and then confirmed via X-Ray reflectivity analysis. Rutherford backscattering spectrometry was used to measure the composition. Energy dispersive spectroscopy images taken with a scanning transmission electron microscope found no evidence of inhomogeneities at the 10 nm scale as reported in *a*-Gd-Fe-Co[79] (See Appendix B).

The magnetization was measured with a SQUID magnetometer and found the compensation temperature (T_M) of all samples to be near 400 K, as shown in fig. 6.1, due to the 22 at.% RE content, allowing to maintain nearly constant values of saturation magnetization ($\sim$ 100 emu/cc, see fig. 6.2) and T_M while varying the Gd/Tb ratio. Thus at room temperature the magnetization is RE-dominant. A vibrating sample magnetometer found the Curie temperature to lie above 600 K. This lower limit is given because as the temperature increases the PMA decreases and is eliminated in the 620 - 670 K range.[80] At these high temperatures nucleation of crystallites is possible and undesirable for this work.

An additional film consisting of *a*-$Gd_{19}Co_{81}$ was also grown to verify whether or not crossing the compensation point is relevant for HI-AOS. Much has been made about the role which the magnetization compensation point plays in switching, and it has been suggested that heating across this point is a requirement for HI-AOS.[81] This sample was found to exhibit HI-AOS, thus contradicting this explanation which has previously been challenged by modelling which showed switching without the traversal of the compensation point.[57] This sample's dynamics were not studied as the point of the study was to keep M and T_M constant while varying the Gd/Tb ratio. Nonetheless the fact that this composition also switched is a reflection that a deeper understanding is needed to explain this phenomenon in a consistent theory.

6.3 PMA in *a*-Gd-Co Alloys

The oft-repeated claim in recent studies of the ultrafast magnetization dynamics of *a*-Gd-Fe-Co is that the Co gives rise to the perpendicular anisotropy and that $\sim$ 10 at.% Co is sufficient to give PMA to these films[55, 56, 59, 82]. If this is true then it stands to reason that the Fe is extraneous and studying *a*-Gd-Co should simplify matters by reducing the number of variables. This was the rationale followed when designing this project.

Instead, a series of growths showed that achieving PMA in *a*-$Gd_{22}Co_{78}$ is not trivial. The initial plan was to have films be 25 - 30 nm thick, and to cap with Ta to establish a control before testing the effect of different over and under layers. However, no film at this thickness had PMA despite

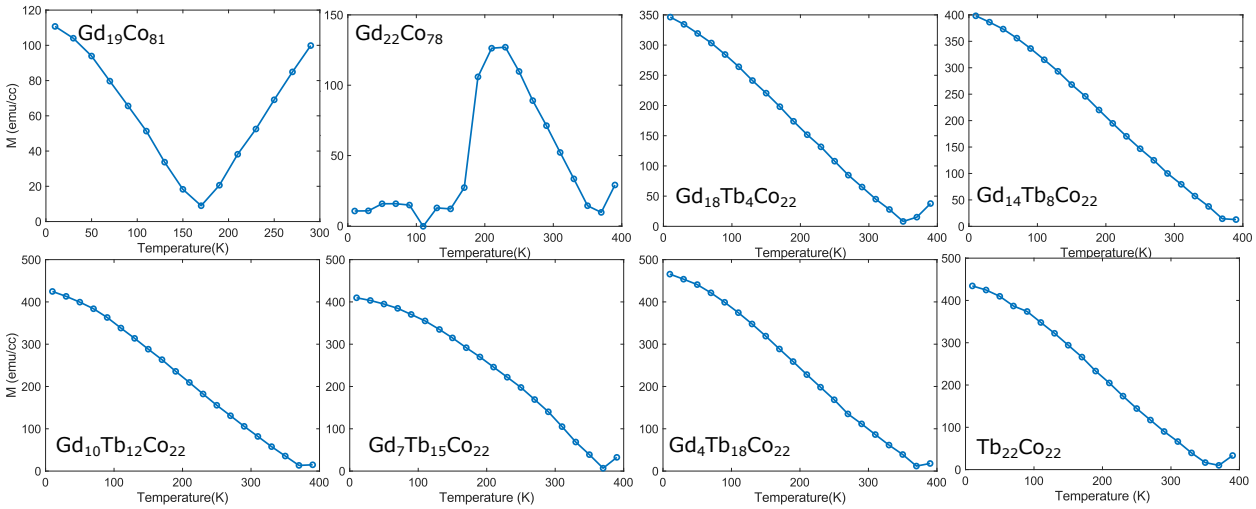

Figure 6.1: Remanent magnetization as a function of temperature after saturating in a 5 T magnetic field applied in the out of plane direction. *a*-$Gd_{19}Co_{81}$ with a compensation temperature below room temperature exhibited HI-AOS but its magnetization dynamics were not studied. The M(T) for *a*-$Gd_{22}Co_{78}$ falls near zero at low temperatures because the perpendicular anisotropy energy is overcome by the shape anisotropy.

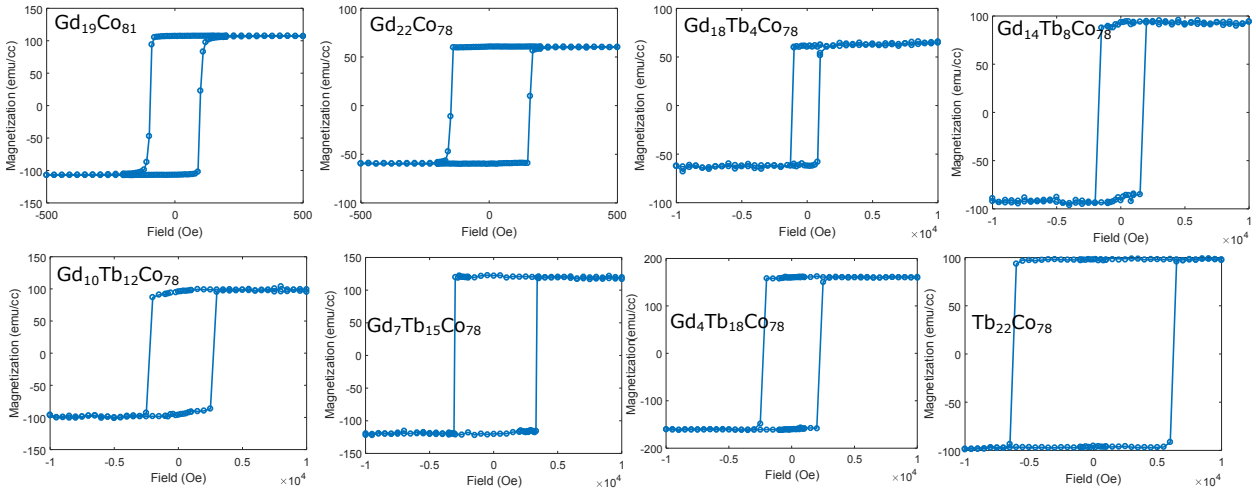

Figure 6.2: Magnetic hysteresis measurements of all samples in this study plus an additional *a*-$Gd_{19}Co_{81}$ sample used to determine if heating through the compensation point is relevant for HI-AOS.

exploring several parameters such as growth temperature, composition and Ar pressure. Eventually it was found that reducing the thickness to 10 nm while growing with Pt over and underlayers led to perpendicular anisotropy, which led to the supposition that the anisotropy in this film was mostly of interfacial character. This would be in contrast to the Tb-containing films which have single-ion anisotropy come from the Tb atoms thanks to its asymmetric 4f orbital due to its $L = 3$ value.

Subsequent growths however, produced films with in-plane magnetization despite following the same recipe that had successfully grown both *a*-$Gd_{22}Co_{78}$ and *a*-$Gd_{19}Co_{81}$ with Pt over and underlayers. A review of the literature shows a complicated story for PMA in *a*-Gd-Co. It was first reported in 1973 that sputtered *a*-Gd-Co and *a*-Gd-Fe had PMA[39]. In 1976 it was found that thermally evaporated *a*-Gd-Co possessed PMA but not sputtered *a*-Gd-Co.[40] Subsequently, other reports confirmed this lack of PMA in sputtered *a*-Gd-Co and noted that both growing in an oxygen or nitrogen-rich atmosphere induced PMA[83, 84].

Recent studies in the ultrafast demagnetization dynamics of RE-TM alloys offer mixed results as well, with one group growing *a*-Gd-Co with PMA in a sputtering chamber,[85] while another achieving in-plane magnetization via molecular beam epitaxy[86, 87]. This last group published a fairly extensive structural characterization work on *a*-Gd-Co, reporting that as-grown films show a lateral gradient composition and a Gd surfactant effect[88]. A tendency of Gd atoms to migrate to the surface was shown to be followed by oxidation down to a nanometer, particularly when the film was grown at very slow rates. All of this demonstrates the extreme sensitivity of the magnetic properties of Gd-based alloys.

Noting the prevailing suggestions in this historical data of oxygen inducing PMA, and in an effort to obtain a reproducible recipe that would yield *a*-Gd-Co with PMA, reactive growths in an oxygen atmosphere were attempted. Fig. 6.3a and 6.3b depict the results of growing *a*-Gd-Co under one standard cubic centimeter per minute (sccm) of oxygen and under a partial pressure of oxygen of 1.7 x 10^{-7} torr respectively. Both films aimed for the same composition of 22 at.% Gd and 78 at.% Co but a clear reduction in the magnetization is evident in the film grown with 1 sccm of O_2 and 10 sccm of Ar at 1 mtorr working pressure. As this is the lowest oxygen flow that the mass flow controller can achieve, a leak valve was installed with which the O_2 pressure was kept constant during deposition by adjusting the leak valve to a constant background pressure of O_2 prior to opening the leak valve of 1.7 x 10^{-7} torr out of total background pressure of 8.8 x 10^{-8} torr as read with a residual gas analyzer before flowing 10 sccm of Ar. Sample b) resulted from these conditions, and it can be seen that the magnetic behavior of this film is closer to that of fig. 6.3c, labeled as "Seasoned Target" which will be explained below. Sample a) visually had a blue tint to its appearance, instead of the shiny metallic gray exhibited by samples b) and c). The reduction in M plus the distinct change to its optical properties indicate that sample a) is substantially oxidized, whereas b) and c) seem to be of comparable quality. It should be noted that all three of these samples exhibited HI-AOS, although only sample c) is part of the main study involving the magnetization dynamics measurements due to timing of sample preparation and beam time allocation. Future work should focus on samples like b).

Eventually it was found that sample c) is the result of "seasoning" of the Gd target. When a target is being cleaned via pre-sputtering it is depositing material onto the surface of the gun's shutter. Gd is an extremely good oxygen getter and after a certain time the gadolinium deposited

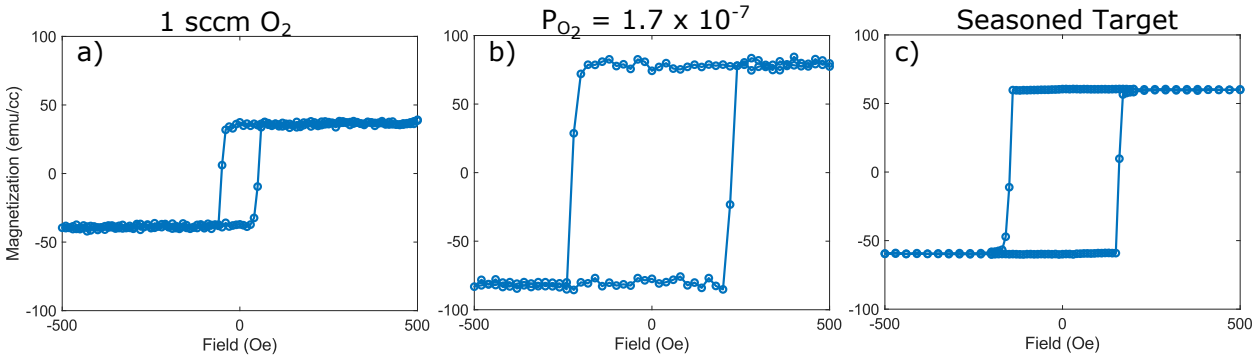

Figure 6.3: Magnetization measurements of *a*-Gd-Co films as grown under: a) 1 sccm of O_2, b) under an oxygen partial pressure of 1.7 x 10^{-7} torr, c) with a "seasoned" Gd target. Note that a) and b) were measured with a VSM and c) with a SQUID, hence the noise level difference.

on the shutter will flake off due to oxidation and place itself on the surface of the Gd target. Over time the conditions will be just right so that pre-sputtering will not fully remove the flake, and thus a little bit of Gd-oxide will be incorporated into the film, giving it PMA. This is what led to the seemingly random conditions that would produce *a*-Gd-Co with PMA. This seasoning of the target was discovered by happenstance as it was noticed that performing a growth after a colleague had previously used it for reactive metal oxide growths often led to *a*-Gd-Co with PMA.

What's interesting about sample c) is that as shown in its RBS spectra in fig. 6.4, it does not contain an oxygen peak, indicating that the presence of oxygen must be below a few percent. Quantifying the degree of oxidation is not an easy task; RBS lacks the sensitivity to detect $<$ 2 at.% O_2, EDS is notoriously bad at detecting oxygen, and X-Ray Photoelectron Spectroscopy (XPS) is too surface sensitive to penetrate through the capping layer of this film. The XPS is fitted with an option to Ar ion mill the sample so that sequential spectra can be taken after a predetermined milling time. However, preferential sputtering of Gd, Co, O and Pt rendered the analysis impossible. Another option could be to tune the oxygen resonance energy of the RBS to probe deeper into the sample. Nonetheless, the growth recipe using an oxygen partial pressure consistently and reproducibly yields *a*-Gd-Co films with PMA.

6.4 Results

MOKE Microscopy

The magnetization of the samples is initialized with an applied out of plane magnetic field of $\sim$ 0.7 T, fully saturating all samples. Samples are then irradiated with 100 fs full-width half maximum (FWHM) optical pulses from a regeneratively amplified Ti-Sapphire laser, with a central wavelength of 810 nm and a bandwidth of 50 nm. The laser beam is p-polarized (electric field in the plane of incidence), and is focused to an elliptical spot with a FWHM of $\sim$ (110 x 80) μm^2, incident at an angle of 50^o with respect to the sample normal. Magneto Optical Kerr Effect (MOKE) images

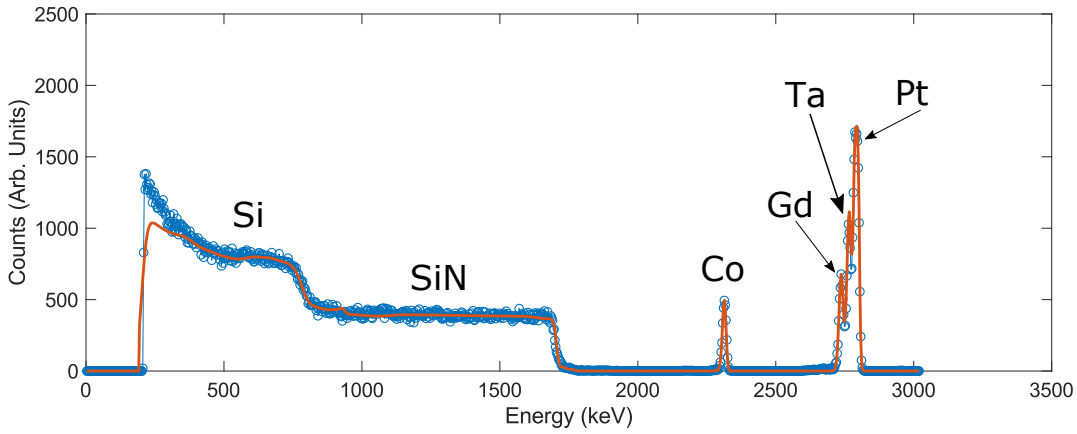

Figure 6.4: RBS spectra of a-$Gd_{22}Co_{78}$ used to measured the atomic composition. If oxidation of the Gd-Co layer is present it would show up as a peak somewhere along the SiN extended peak. Since the signal comes clean the degree of oxidation must be below a couple percent. Solid orange line is the fit using SIMNRA.

depict single shot switching of the magnetization across all films but a-$Tb_{22}Co_{78}$ as shown in Fig. 6.5a. It is seen that films with as little as 4 at.% Gd have deterministic magnetization reversal upon irradiation with a single laser pulse. Amorphous $Tb_{22}Co_{78}$ only shows demagnetization as evidenced by the nucleation of random magnetic domains.

Magnetic Anisotropy

The intrinsic anisotropy constant (K_{ui}) was measured as described in Ch. 5 at room temperature and is plotted as a function of Tb at.% in Fig. 6.5b. The anisotropy constant increases systematically with increased Tb due to its large single ion anisotropy contribution. The effect of growing on Ta or SiN, and of capping with Ta or Pt are also shown in figure 6.5b – Pt promotes larger PMA while Ta and SiN lead to slight decreases; neither buffer nor capping layer tested had any impact on a film's ability to switch via HI-AOS.Despite the systematic increase in K_{ui}, only a-$Tb_{22}Co_{78}$ did not exhibit HI-AOS. Comparison of the anisotropy constants of a-$Tb_{22}Co_{78}$ and a-$Gd_4Tb_{18}Co_{78}$ shows that despite having near-identical values of anisotropy only the films lacking Gd were unable to reverse its magnetization. Therefore K_{ui} does not determine a film's ability to HI-AOS.

Fluence Dependence on Composition

Figure 6.5c shows that increasing the Tb content increases the incident critical fluence, starting from 4.4 mJ/cm^2 for a-$Gd_{22}Co_{78}$ and linearly increasing to 6.2 mJ/cm^2 for a-$Gd_4Tb_{18}Co_{78}$. Extrapolation of this curve indicates that a-$Tb_{22}Co_{78}$ should possess a critical fluence near 6.7 mJ/cm^2 however switching was not observed. Increasing the fluence led to ablation of the sample. Ellipsometry measurements yielded a complex refractive index of $\sim$3.5 + 4.2i for all samples. This

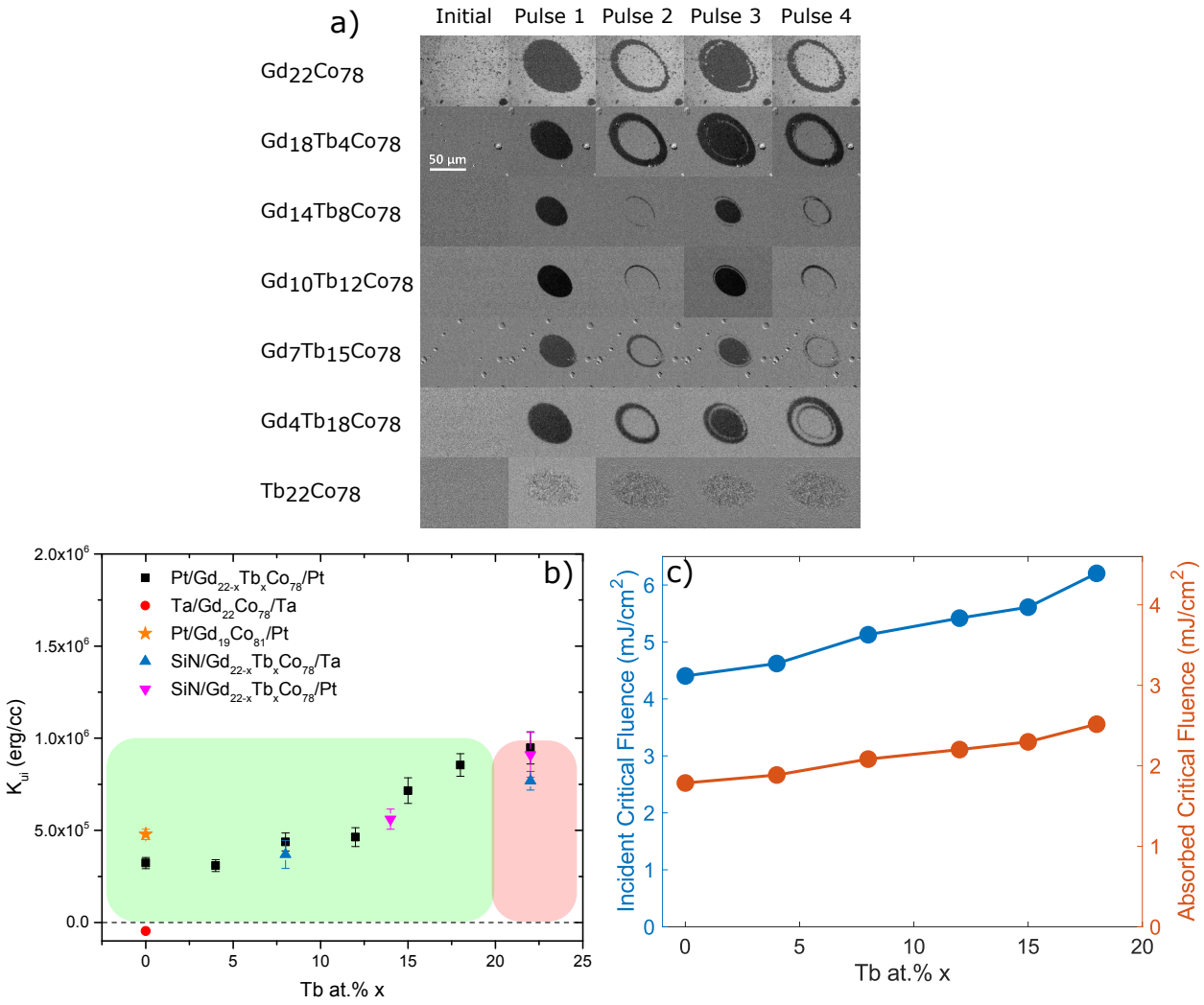

Figure 6.5: a) MOKE microscopy images illustrating samples with ability to all-optically reverse their magnetization upon irradiation.Samples with a Tb concentration of up to 18% exhibited HI-AOS while *a*-$Tb_{22}Co_{78}$ only exhibited demagnetization as evidenced by the nucleation of random domains. b) Intrinsic anisotropy constant K_{ui} vs Tb atomic percent in *a*-$Gd_4Tb_{18}Co_{78}$ thin films. Anisotropy increases with increasing Tb content but no correlation was found between HI-AOS and anisotropy. The green box shows the compositions that exhibited HI-AOS; the red box those that did not. The effect of growing on different substrates and capping layers was tested but it had no effect on HI-AOS. Three separate *a*-Gd-Co samples are shown. At the top is *a*-$Gd_{19}Co_{81}$ with compensation T below RT exhibiting PMA and HI-AOS. Beneath it is *a*-$Gd_{22}Co_{78}$ which is part of the main study. In red is *a*-$Gd_{22}Co_{78}$ which has in-plane magnetization which cannot be probed using polar MOKE, hence it's unknown if it exhibits HI-AOS. c) Incident and absorbed critical fluence increase with increasing Tb content.

results in a net absorption of 41% in each of the samples as extracted from multilayer absorption calculations using the transfer matrix method. The absorbed critical fluence increases linearly from 1.8 mJ/cm^2 to 2.5 mJ/cm^2 for a-$Gd_{22}Co_{78}$ and a-$Gd_4Tb_{18}Co_{78}$ respectively.

Time-Resolved MOKE

Time-resolved MOKE (TR-MOKE) measurements were performed by splitting the laser beam into pump and probe beams and focusing them at the same spot on the sample. The pump beam is as described above for the single shot experiments and triggers the HI-AOS process. The probe is incident normal to the sample surface and its arrival time at the sample relative to the pump is varied by passing the pump beam through a linear delay stage. This enables the probe to detect the temporal dynamics of the magnetization of the a-$Gd_{22-x}Tb_xCo_{78}$ films as they undergo HI-AOS. A peak fluence of 6.9 mJ/cm^2 was chosen as this slightly exceeds the incident critical fluence of a-$Gd_4Tb_{18}Co_{78}$, the sample with the largest Tb content that exhibited HI-AOS.

Figure 6.6a shows the ultrafast magnetization dynamics of all samples studied measured via TR-MOKE. The magnetization reversal process follows a two-step behavior. In the first step a rapid initial drop in the magnetization occurs in which all films share a similar demagnetization process within the first picosecond post irradiation from the pump pulse. The data suggests faster demagnetization rates with increasing Tb, but they are within the errorbar. The second stage consists of remagnetization in the opposite direction as the system cools down. a-$Gd_{22}Co_{78}$ exhibits the fastest remagnetization time and increasing the Tb content systematically slows down this rate. The remagnetization rate plateaus with 15% and 18% Tb samples exhibiting similar dynamics. Finally a-$Tb_{22}Co_{78}$ only demagnetizes upon irradiation and then recovers its magnetization along its initial direction upon cooling. It is possible that a-$Tb_{22}Co_{78}$ exhibits a transient switching in this temporal regime similar to that reported by Alebrand et al.,[76] and modeled by Moreno et al.,[75] or that switching could occur at a higher fluence. However, utilizing higher fluences led to irreversible damage of the sample as the laser ablated or burned the sample's surface. By 200 ps all samples had remagnetized to about 80% of the saturation value.

Fig. 6.6b is a close up of the experimental data of Fig. 6.6a, and it shows how after the initial demagnetization step there is a slight bump in the magnetization that deviates from exponential decay behavior as evidenced in a-$Gd_{22}Co_{78}$, a-$Gd_{18}Tb_4Co_{78}$ and a-$Gd_{14}Tb_8Co_{78}$. The duration of this bump increases with increasing Tb, but for the higher Tb alloys the bump is more linear in character before resuming exponential decay characteristics.

Atomistic Simulations

Atomistic spin dynamics simulations using the VAMPIRE software package[89, 90] combined with a two-temperature model (2TM)[57] (details discussed in Appendix B) neglecting spin-lattice coupling were performed to simulate the experimental magnetization dynamics. As shown in Figure 6.6c the simulation shows excellent agreement with the experiments in reproducing the characteristic behavior of similar demagnetization dynamics followed by increasingly slow remagnetization times with increasing Tb content. A significant bump in the magnetization following the initial

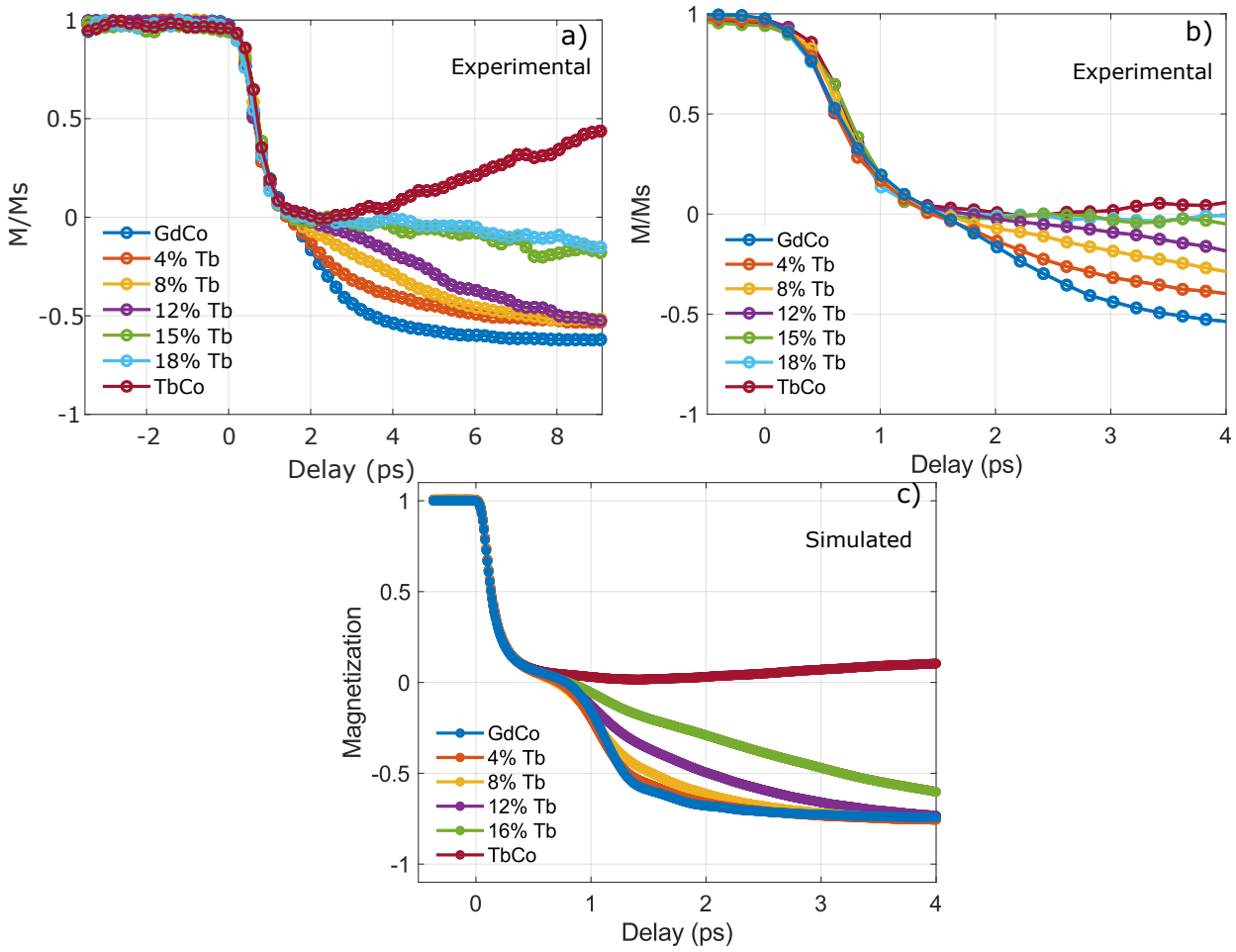

Figure 6.6: a) Time-resolved magnetization dynamics of a-$Gd_{22-x}Tb_xCo_{78}$ thin films measured with a laser fluence of 6.9 mJ/cm^2. The initial rapid drop in magnetization is similar across all samples, but upon entering the remagnetization regime different rates are observed. b) Expanded scale of the experimental data showing the non-exponential behavior in the magnetization following the initial demagnetization step. c) Simulation results of the magnetization dynamics of *a*-$Gd_{22-x}Tb_xCo_{78}$ after laser irradiation obtained with a two-temperature model neglecting spin-lattice coupling as described in the text.

demagnetization step is seen in simulation, and exhibits a more linear character with increasing Tb as seen experimentally. The discrepancy in the time scales between experiment and simulation is due to both the small size of the simulated system not allowing for domain dynamics to be taken in consideration, and also to heat dissipation effects.

Fitting single exponential functions to the data in Fig. 6.6a yields the demagnetization time constant τ that is shown in Fig. 6.7 in blue circles as a function of Tb composition. The data suggests that faster demagnetization rates are achieved with increasing Tb content which is consistent

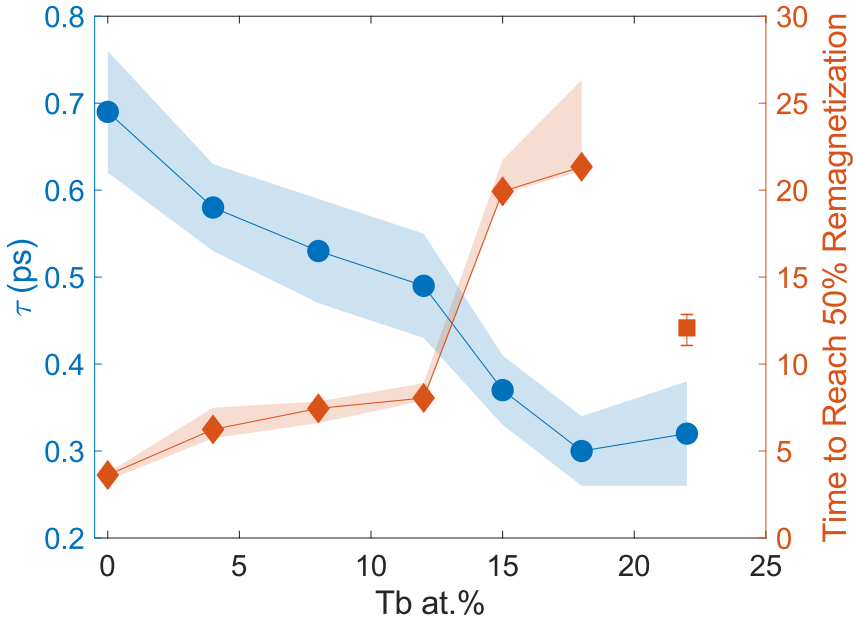

Figure 6.7: Blue circles and color band and left axis: Demagnetization time constant τ obtained from single exponential fitting of the demagnetization stage of Fig. 6.6 as a function of Tb at.%. Orange diamonds and band and right axis: Time required to reach 50% remagnetization as a function of Tb at.%. Increasing the Tb content slows the magnetization reversal until only demagnetization and recovery is observed in a-$Tb_{22}Co_{78}$: the orange square is its time to recover to 50%. The shaded region is the error bar. Data collected after 20 ps had a larger time step, thus the larger error observed.

with the report that in $Gd_{1-x}Tb_x$ alloys the demagnetization rate speeds up with increasing Tb[91] due to the increase in spin-lattice coupling. However, despite how provocative this result is, the time constants here reported are within the experimental error and thus it is not safe to confidently conclude that the demagnetization stage scales with Tb content. The blue shaded region in Fig. 6.7 is the error bar extracted from the single exponential fits, with a 95% confidence band based on the quality of the fit, and is not representative of the experimental error which is at least 100 fs and thus the extracted τ values are within the experimental uncertainty. Since 100 fs is the minimum time step available there is no easy immediate way to better resolve the region of interest. The orange curve in Fig. 6.7 charts the time to reach 50% remagnetization in the opposite direction. The value of 50% is arbitrary and it's meant simply to quantify the observation that increasing the Tb content slows the magnetization reversal until only demagnetization and recovery is observed in a-$Tb_{22}Co_{78}$: the orange square is the time to recover to 50% along the initial magnetization direction. The orange shaded region is the error bar and its asymmetric on the 15% and 18% Tb samples because above 20 ps fewer data points were taken thus increasing the uncertainty.

Fluence Effect on Dynamics

The effect of different fluences on the magnetization dynamics were tested on a-$Gd_{14}Tb_8Co_{78}$ and the results are shown in fig. 6.8. Incident fluences at and below 4.8 mJ/cm^2 only lead to demagnetization and recovery. At an incident fluence of 4.8 mJ/cm^2 the magnetization displays oscillatory behavior near 4 ps and beyond during the recovery stage. This is indicative of the sample's magnetization being at the threshold of switching and thus this fluence is near the critical value. Exceeding the critical fluence led to magnetization reversal with similar dynamics, with the highest fluence of 6.9 mJ/cm^2 displaying a slightly faster remagnetization in the first two ps but then following similar behavior as the other two high fluences. This is probably due to higher heating from the larger laser power and is commonly observed.

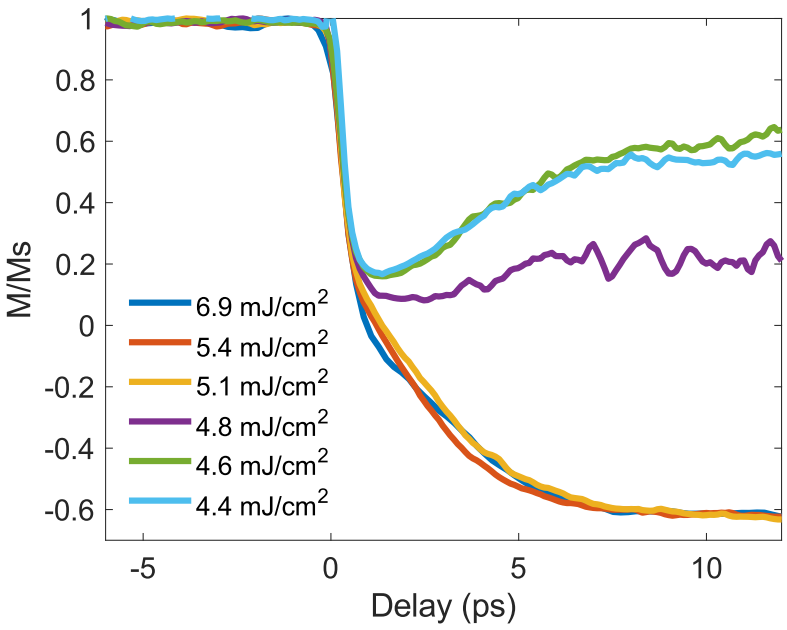

Figure 6.8: TR-MOKE measurements of the dynamics of a-$Gd_{14}Tb_8Co_{78}$ under different incident fluences.

Effect of Annealing

Annealing was used to test the influence of anisotropy and damping on the dynamics. The results are shown in Fig. 6.9. Annealing a-$Gd_{10}Tb_{12}Co_{78}$ at 300 °C for one hour results in a significant reduction in coercivity and anisotropy while maintaining the composition and M_S constant as seen in Fig 6.9a. Further annealing the sample at 350 ^{o}C removed the PMA. The fact that M_S was unchanged by annealing strongly indicates that inhomogeneities such as phase segregation have not occurred. A slower remagnetization time is observed in Fig 6.9b after annealing – similar to

those in the 15% and 18% Tb samples. Atomistic simulations of the dynamics of this sample as a function of Gd damping are shown in Fig. 6.9c. It can be seen that increasing the damping on the Gd sites leads to a slower remagnetization time, suggesting that the experimentally annealed sample has reduced magnetic anisotropy and increased damping. Work from Malinowski et al.[92] showed that introducing local variations of the anisotropy in amorphous CoFeB leads to an increase in the damping parameter. Since the origin of anisotropy in RE-TM alloys is due to a combination of pair-ordering along the growth direction and the single ion anisotropy of Tb[48], annealing leads to a structural relaxation of the pair-ordering that introduces local anisotropy variations which in turn lead to higher damping and thus the slower remagnetization time observed.

Figure 6.10 shows the simulation results of critical fluence as a function of Tb concentration and varying Gd damping. It shows that increasing the Tb content increases the critical fluence as observed experimentally, regardless of the specific damping value used. It also shows, that for a given concentration, increasing the damping increases the critical fluence. This suggests that there are two factors at play in shaping the magnetization dynamics but it's possible that the spin-orbit interaction is the common denominator. As seen in the simulations of fig. 6.9c, at a fixed composition the key parameter that leads to slower remagnetization is the increase in damping. In simulation the damping constant is a phenomenological parameter that combines a host of diverse effects whose physical origins are not often well defined. Increasing the Tb composition leads to a greater spin-orbit interaction in the system (which is considered the intrinsic source of damping[93]) and is proportional to ξ^2/W, where ξ is the spin orbital coupling energy and W is the d-band width[94]. Thus as the system becomes Tb-rich it experiences increased spin-orbit coupling which increases both anisotropy and damping and thus leads to the dynamics observed in Fig. 6.6a and Fig. 6.6c. For the dynamics observed in the annealed sample, the spin-orbit coupling likely has not changed, but the direction of the spin-orbit coupling likely did due to the structural relaxation undergone upon annealing, thereby increasing the damping. The simulation does not directly account for spin-orbit coupling, but it indirectly simulates the effects of stronger spin-orbit coupling via increases in the anisotropy energy or the damping parameter. Therefore although the simulations reveal the critical role that damping plays in modifying the ultrafast magnetization dynamics, it is entirely possible that the underlying physical mechanism is rooted in the spin-orbit interaction.

6.5 Discussion

Following the results of Bergeard et al.,[86] and the hypothesis of Gorchon et al.,[95] local transfer of angular momenta between the RE and TM sublattices plays a major role in the ultrafast reversal dynamics of RE-TM ferrimagnets.We suggest that in Gd-TM ferrimagnets, the 4f (RE) - 5d (RE) - 3d (TM) exchange is the dominant channel for spins to transfer angular momentum between sublattices and subsequently reverse their magnetization. Damping can be considered as an over-arching factor for the loss of energy from the macroscopic variation of the local magnetization by transfer of energy to coupled phonons, spin waves etc.[93, 96] Since Gd has $L = 0$, its 4f orbital is spherical and angular momentum transfer to the lattice from the spin bath is limited, resulting in

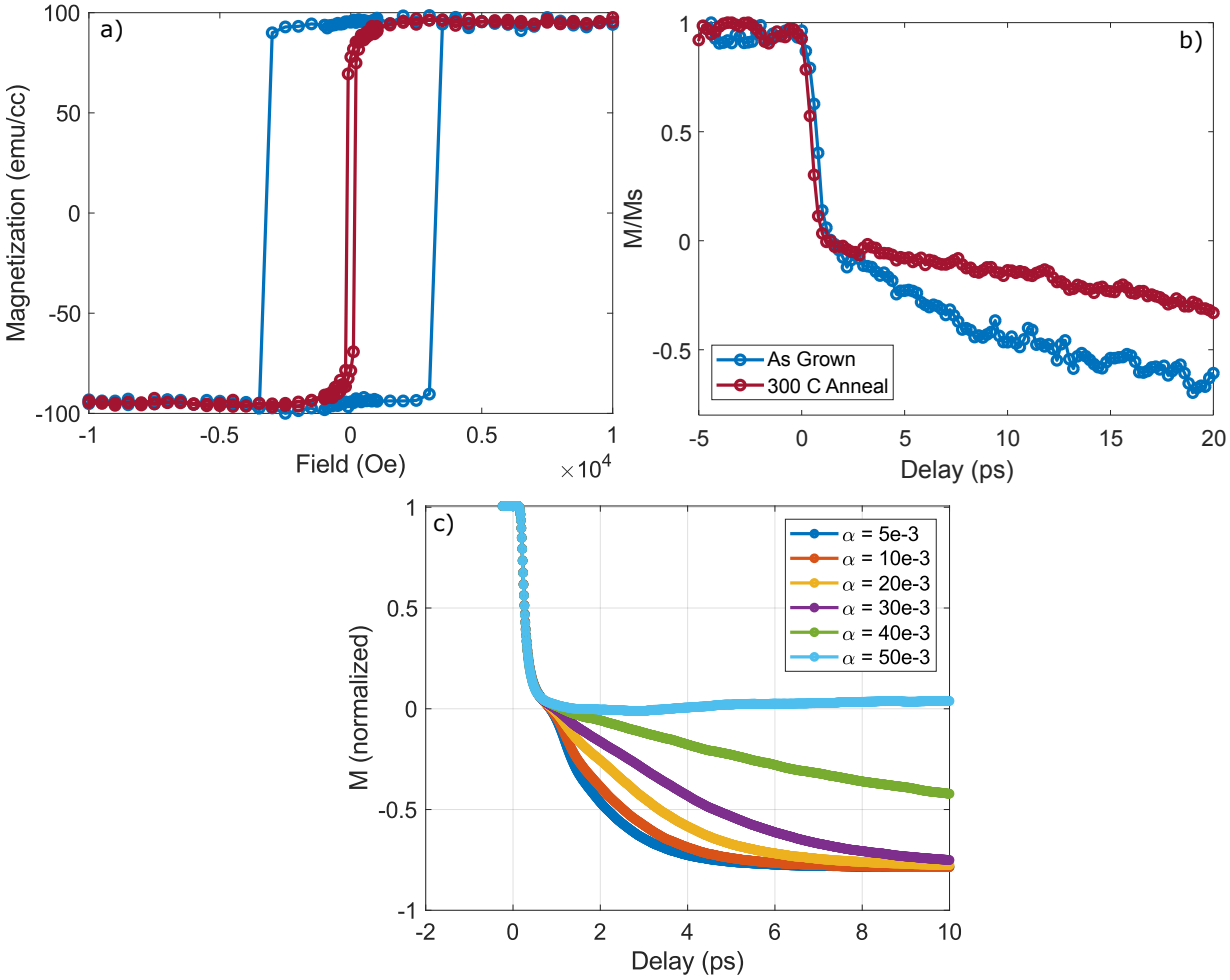

Figure 6.9: a) Magnetization loops in the out-of-plane orientation depicting how annealing reduces the coercivity and anisotropy while keeping M_S intact. b) Magnetization dynamics of *a*-$Gd_{10}Tb_{12}Co_{78}$ in the as-grown state (blue curve) and after annealing (red curve) at 300 ^{o}C for 1 hour. Annealing leads to a slower remagnetization time. c) Simulated time-resolved magnetization dynamics of *a*-$Gd_{10}Tb_{12}Co_{78}$ as a function of increasing Gd damping. Increasing the damping leads to a slower remagnetization time, indicating that annealing leads to a higher damping value.

both low damping and anisotropy compared to Tb. Adding Tb on the other hand, relaxes this constraint due to the anisotropic 4f orbital giving $L = 3$, which introduces greater spin-lattice coupling via the spin-orbit interaction and this paves a channel for the system to dump angular momentum into the lattice. This is reflected in greater damping in the *a*-RE-TM system as assumed by the simulations. Increasing the Tb concentration preferentially increases angular momentum transfer into the lattice with fewer spins participating in the 4f - 5d - 3d exchange, thereby inhibiting switching. Therefore the increased critical fluences and slower magnetization dynamics observed

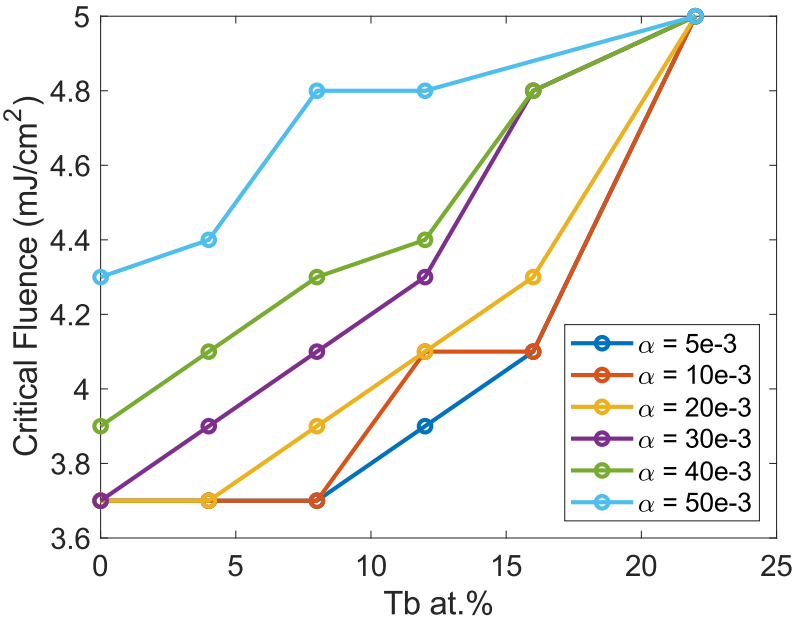

Figure 6.10: Simulated critical fluence as a function of Tb concentration for different damping values of Gd. The Tb and Co damping parameters are constant (0.05). The critical fluence increases as the damping of Gd increases, indicating that lowering the damping of Gd reduces the threshold switching condition of Gd-Tb-Co alloys below the laser ablation limit.

in *a*-Gd-Tb-Co alloys can be explained by the increased magnitude of the spin-orbit coupling that accompanies increasing Tb content. Alternatively, the critical fluence can be linked with the spin wave spectrum, which in the simplest case for a ferrimagnet consists of a ferromagnetic and antiferromagnetic branch. Theoretical work has shown that both modes need to be accessed by the energy from the laser pulse to excite a two-magnon bound state leading to an efficient angular momentum transfer between sublattices [82]. Increased damping on the RE sublattice by the addition of Tb effectively shuts down this exchange, thereby increasing the critical fluence.

6.6 Conclusion

In conclusion, we have shown that *a*-$Gd_{22-x}Tb_xCo_{78}$ thin films exhibit HI-AOS from x = 0 to x = 18, displaying similar demagnetization dynamics and slower remagnetization times with increased critical fluences as Tb content increases. The remagnetization dynamics are explained on the basis of increased damping as the Tb atomic percentage increases. The systematic increase in K_{ui} with increasing Tb content is not correlated with HI-AOS, and annealing led to a slowing of the remagnetization rate, which as verified by simulations indicates that damping is responsible for modifying the ultrafast magnetization dynamics. Two-temperature modeling of the dynamics

reproduced the experimentally observed behavior as well as the strong dependence of critical fluence with increasing Tb content. The experimental inability to observe HI-AOS in *a*-Tb-Co is due to the high critical fluence that under the present conditions is inaccessible without ablating the film. This suggests that better management of the laser thermal load may lead to HI-AOS beyond Gd-TM alloys.

Chapter 7

Time-Resolved X-Ray Magnetic Circular Dichroism of *a*-$Gd_{10}Tb_{12}Co_{78}$

7.1 Introduction

The results of Chapter 6 were obtained with a laser probe wavelength of 810 nm, which is only sensitive to the excitations of Co's 3d electrons plus a small contribution from Gd's 5d electrons which have a residual magnetization due to hybridization.[97] In a system such as *a*-$Gd_{10}Tb_{12}Co_{78}$ this means that a lot of information from the other two magnetic sublattices, Gd and Tb, is not being collected which could help explain the mechanism of HI-AOS. To remedy this, time-resolved X-Ray Magnetic Circular Dichroism (TR-XMCD) measurements were performed at the femtoslicing facility at BESSY II in Berlin.

7.2 Results

The time-resolved XMCD measurements were performed by exciting the sample with 60 fs laser pulses of 800 nm wavelength at a repetition rate of 3 kHz and probing the subsequent dynamics with 100 fs circularly polarized X-ray pulses. By setting the X-ray photon energy at the maximum absorption edge of Co (L3 edge) and Gd and Tb (M5 edges) the dynamics of the Gd, Tb and Co magnetic moments can be disentangled separately. The typical size of the laser beam in focus at the sample, which was at the focal point, was 0.8 x 0.4 mm. The X-ray beam size was 0.3 x 0.1 mm. The laser-induced changes of X-ray transmission were measured for opposite orientations of the magnetic field using a Si avalanche photodiode and a gated boxcar detection system. The time evolution of the pumped (in the presence of laser excitation) and un-pumped (in absence of laser excitation) signals were recorded as a function of pump-probe delay. The dynamic XMCD signals were obtained from the difference of the laser-induced absorption changes measured for opposite magnetic fields. Measurements were done at room temperature under high vacuum.

The incident laser fluence used here to achieve switching (40 mJ/cm^2) is much greater than the one used in TR-MOKE in Chapter 6 of 6.9 mJ/cm^2. Efforts to verify the calibration of this

measurement at the beamline did not yield any immediate nor obvious answers regarding this extreme fluence discrepancy. Since the TR-XMCD measurements are done in vacuum, it would seem likely that the membrane would not be able to withstand the thermal load from the laser due to the lack of convective heat dissipation that is present when in air, suggesting that the incident fluence is in fact significantly lower. This detail remains unresolved.

The samples consisted of Ta(3)/Pt(3)/*a*-$Gd_{10}Tb_{12}Co_{78}$(25)/Pt(3) grown onto X-Ray transparent, *a*-SiN_x membranes 100 nm thick. The Ta is a seed layer that grows amorphous and helps the subsequent Pt layer grow with little roughness. 25 nm of *a*-$Gd_{10}Tb_{12}Co_{78}$ is thick enough to produce good signal to noise ratio for XMCD, and it's thin enough to not incur a heavy X-ray absorption penalty. Samples were capped with 3 nm of Pt to prevent oxidation. Samples were sandwiched between Pt layers to keep the growth recipe presented in Chapter 6 unchanged and be able to compare results across studies. The chips were purchased from Silson Ltd, and consisted of a 7.5 mm x 7.5 mm Si frame, with nine 1x1 mm *a*-SiN_x windows set in a 3x3 array as depicted in fig. 7.1. Having nine windows per chip effectively yielded nine identical samples and allowed the experiment to switch from window to window easily in case a membrane popped due to thermal stresses without wasting beam time. For this pump-probe experiment it was found necessary to irradiate the corners of the window in order to maximize the thermal dissipation and overcome self-heating artifacts.

A thermal heat sink layer consisting of 200 nm of Al was deposited on the backside of the membrane in order to increase the thermal dissipation. Al was picked for its high thermal conductivity and its low X-ray absorption cross-section. The Al layer was deposited via DC magnetron sputtering deposition in the same chamber where the main samples were produced under identical conditions consisting of a background pressure 8.8 x 10^{-8} torr, 1.1 mtorr of Ar and grown at room temperature.

The element-specific magnetization dynamics of 25 nm of *a*-$Gd_{10}Tb_{12}Co_{78}$ are shown in fig. 7.2. Upon irradiation we observe a two-step magnetization reversal process consisting of an initial fast drop in the magnetization, followed by a slower remagnetization in the opposite direction. The cobalt sublattice demagnetizes fastest with a time constant of 320 fs, followed by Tb and Gd with time constants of 410 fs and 630 fs respectively. These time constants are consistent with literature values of *a*-Gd-Fe-Co[55, 56] and were extracted from fitting single exponential functions to the data. The cobalt dynamics as presented in Fig. 7.2 are the average of 22 scans, while the dynamics of Tb and Gd are the result of averaging 11 and 42 scans respectively, hence the larger uncertainty in Tb. The width of the error bars is one standard deviation of the variation in data for that element at that delay. The demagnetization time of Co found here is consistent with that found in Chapter 6 for the sample of the same composition.

Fig. 7.3 plots the individual scans of each element in the left column and compares it to its average in the right column to illustrate the inherent difficulty in determining when sufficient data has been collected due to the high signal to noise ratio present. Particularly for the RE measurements it's difficult to ascertain from a few scans if the magnetization is reversing, and finding the right amount of data density and delay range is not immediately obvious. This can be seen for instance in the longer delay range measured for Tb where it was important to confirm if the REs were indeed switching since in Gd by 50 ps, the magnetization had reversed by 15% (-15% of M_s).

Figure 7.1: X-Ray transparent SiN windows used for the beamtime experiments to acquire the TR-XMCD signal in *a*-$Gd_{10}Tb_{12}Co_{78}$.

By extending the delay range on Tb it was confirmed that indeed both REs were reversing. The Co dynamics display a linear regime after demagnetization that lasts up to around 10 ps, consistent with the TR-MOKE data presented in Chapter 6 which is only sensitive to the Co dynamics.

The small amount of magnetization reversal observed in the RE led the beamline scientists to suggest that a 'halo' background correction be made. Besides the femtosecond X-ray pulses, slicing sources inherently also produce a so-called 'halo' background with different time structure, polarization and pointing that interferes with the time-resolved data causing intensity loss. The halo background radiation superimposes over the 100 fs slicing X-ray pulses and is a consequence of the remaining electron bunch excitations from preceding electron-energy-modulation events by the femtoslicing itself. It's a dynamic contribution to the signal which has to be measured and subtracted on a point by point basis as detailed here [98]. The implementation of this halo correction comes at the cost of doubling the acquisition time. The result of this background correction is shown in Fig. 7.4 for the Tb sublattice, and it reveals a less ambiguous magnetization reversal that increases the observed amount of magnetization switching from 15% to 27% at 300 ps. Cobalt at 50 ps had reversed by 30% in comparison. This made it evident that for future measurements the

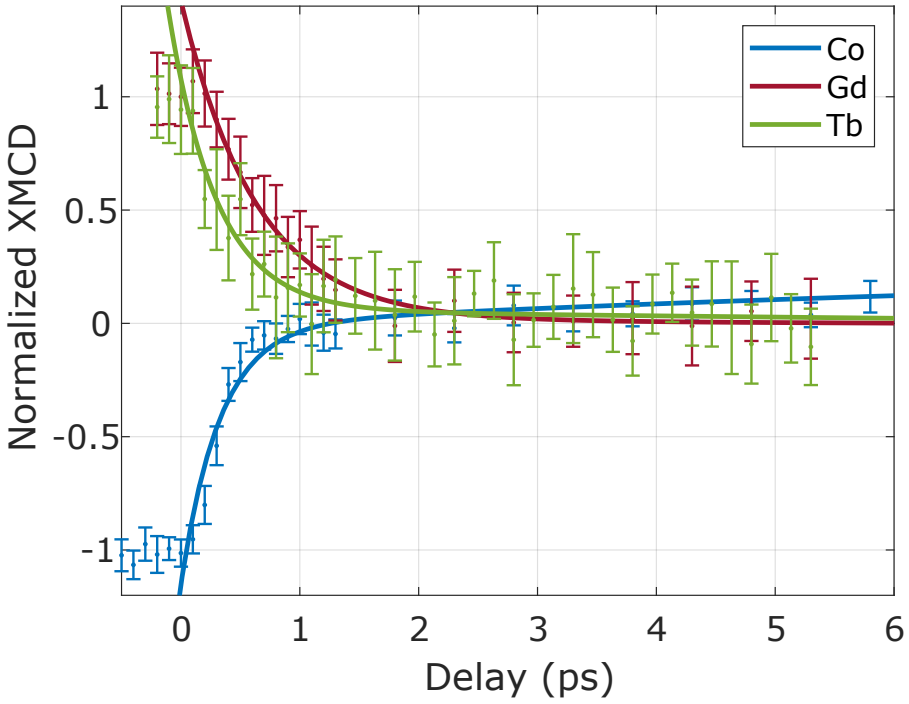

Figure 7.2: Time-resolved XMCD of the three magnetic sublattices: Gd, Tb and Co show that the demagnetization stage is fastest for Co, followed by Tb and finally by Gd. The solid lines are single exponential fits that help visualize the existence of a ferromagnetic transient state between Co and Gd, and Co and Tb between 1.5 and $\sim$ 15 ps where all three signals are greater than zero. The error bars are half of one standard deviation.

halo background must be subtracted in order to properly measure the dynamic signal.

While the data unambiguously shows the demagnetization times of all sublattices, the point at which the magnetization crosses zero for both Gd and Tb is not well-defined. These preliminary data suggest that Gd and Tb cross zero at about 15 ps, while Co crosses zero at around 1.5 ps, indicating a transient ferromagnetic state lasting around 13.5 ps. However, due to the limited density of points, number of scans and halo background more data is necessary in order to improve the signal-to-noise ratio and increase the certainty of these estimates, particularly for Gd and Tb which have a smaller cross-section due to their low atomic concentration in the alloy.

During data acquisition it was noted that cobalt, gadolinium and terbium appeared to oscillate in-phase with a half-period at the sampling density of dt = 500 fs in the time interval of 1-8 ps. An effort was made to determine whether or not these oscillations were from magnon excitations of the antiferromagnetic mode[82] or merely artifacts from insufficient data collection. In this analysis the amplitude of the Fourier transform over the time interval of 1-8ps was investigated. Given the step sizes the Fourier data is limited to F = 1/(2*dt) = 1 THz. Fig. 7.5 shows the Fourier amplitudes in log scale of the mean XMCD data for each element. Notice that at the 1 THz point

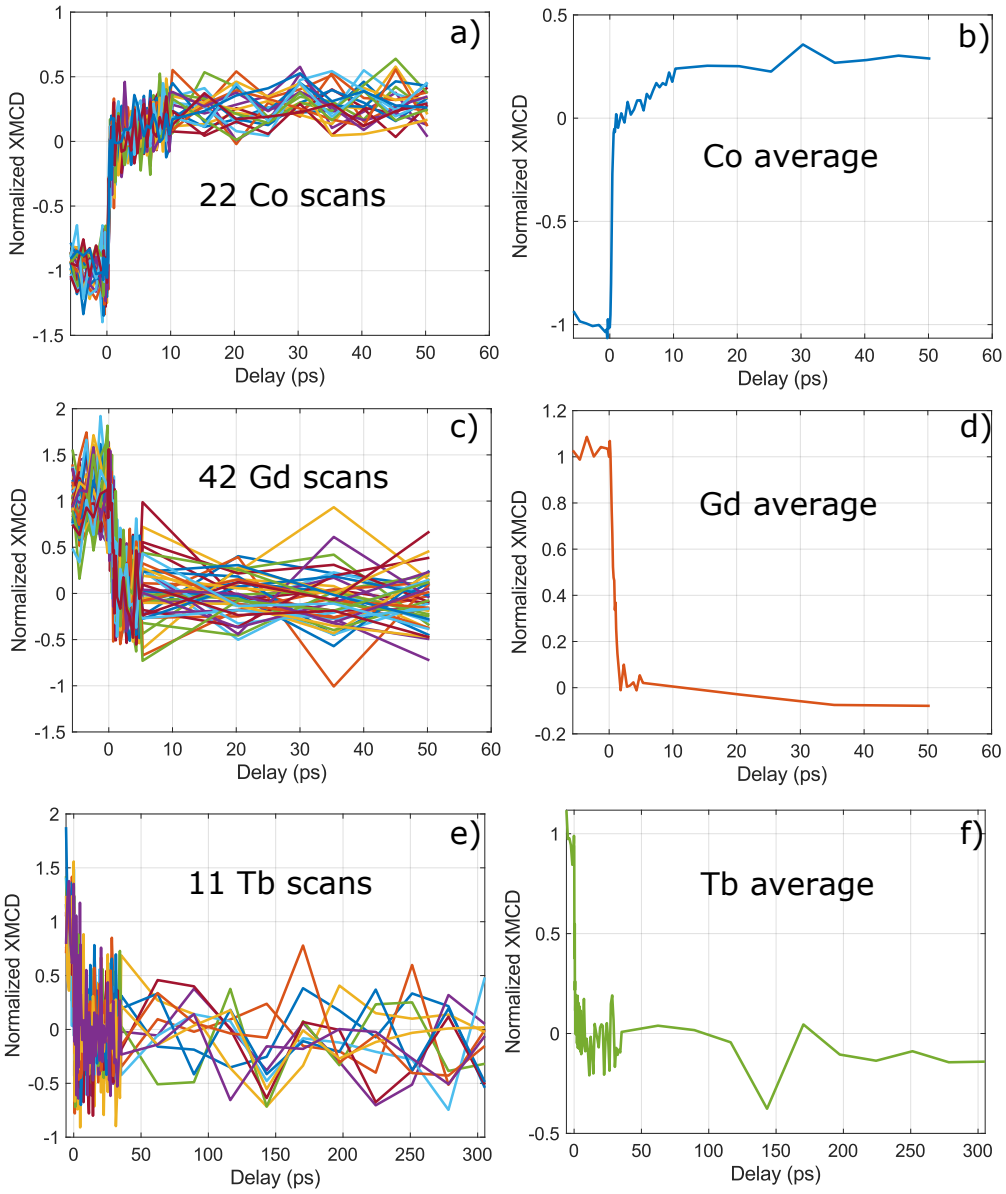

Figure 7.3: The element-specific magnetization dynamics of Co, Gd and Tb taken at the L_3 and M_5 absorption edges of Co and Gd/Tb respectively. a) is the total number of scans on the Co sublattice from which the average is calculated as shown in b). The pairs c) and d), and e) and f) show the total scans and their corresponding average for Gd and Tb respectively.

all of the elements show a notable increase. However, not enough confidence in genuine oscillatory behavior can be attained with a sampling of 500 fs. To address this, more data was acquired for terbium with a denser sampling of dt = 200 fs within this regime.

Fig. 7.6 shows the terbium dynamics spectrum in the 1-6ps regime sampled at 200 fs. With

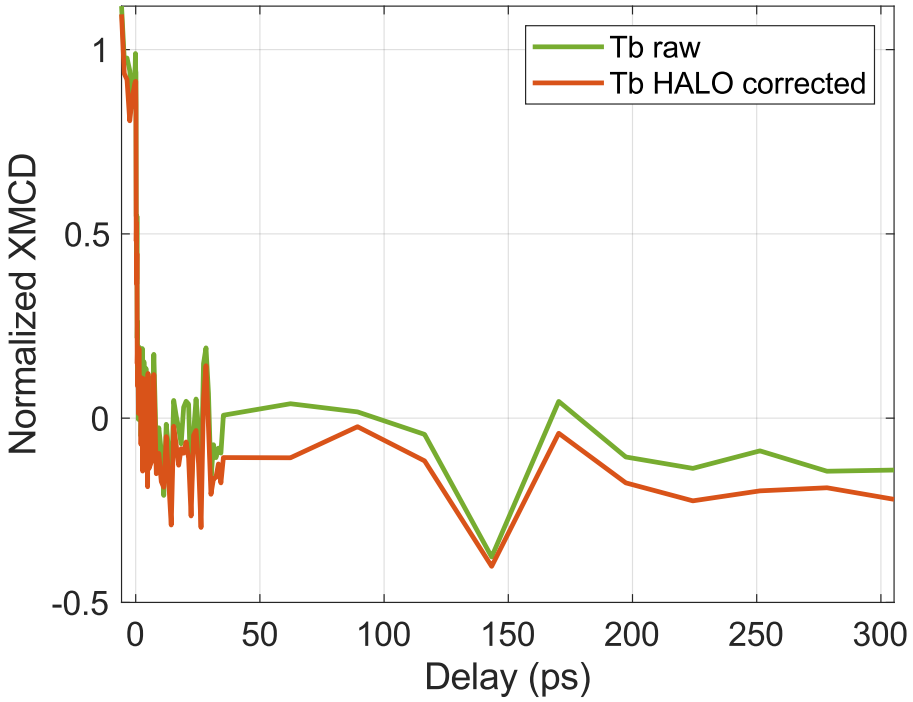

Figure 7.4: Halo corrected scans showing its effect on the magnitude of the XMCD signal collected.

this increased sampling it is fairly evident no notable peaks exist, suggesting that the prior noted oscillations may have been artifacts of under-sampling.

7.3 Conclusion

These preliminary results indicate that more data needs to be collected in order to better characterize the zero-crossing of the magnetization and the lifespan of the transient ferromagnetic state between Co and Gd/Tb. Nonetheless the demagnetization times are well-resolved and are consistent with the results found in both Chapter 6 and literature, and show that Co demagnetizes first, followed by Tb and Gd. The faster demagnetization of Tb compared to Gd suggests that the increased spin-lattice coupling in Tb is responsible for the faster demagnetization rate. Studying other compositions is planned and this will help elucidate what are the factors that enable and modify helicity-independent all optical switching.

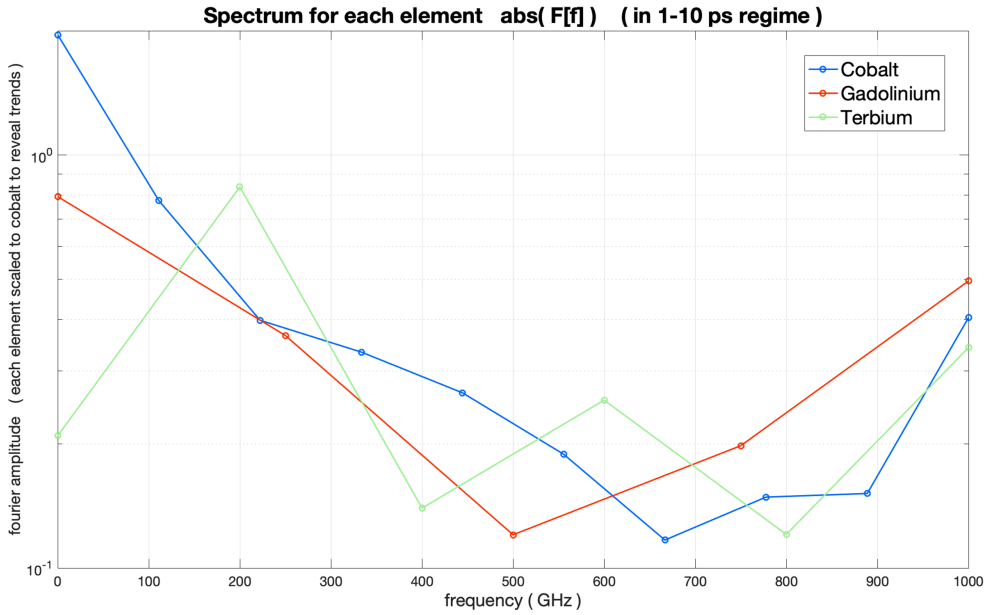

Figure 7.5: Fourier decomposition of the TR-XMCD data in the 1 - 10 ps regime. Difficult to trust the results past 500 GHz due to the small 500 fs step size for Co and Gd.

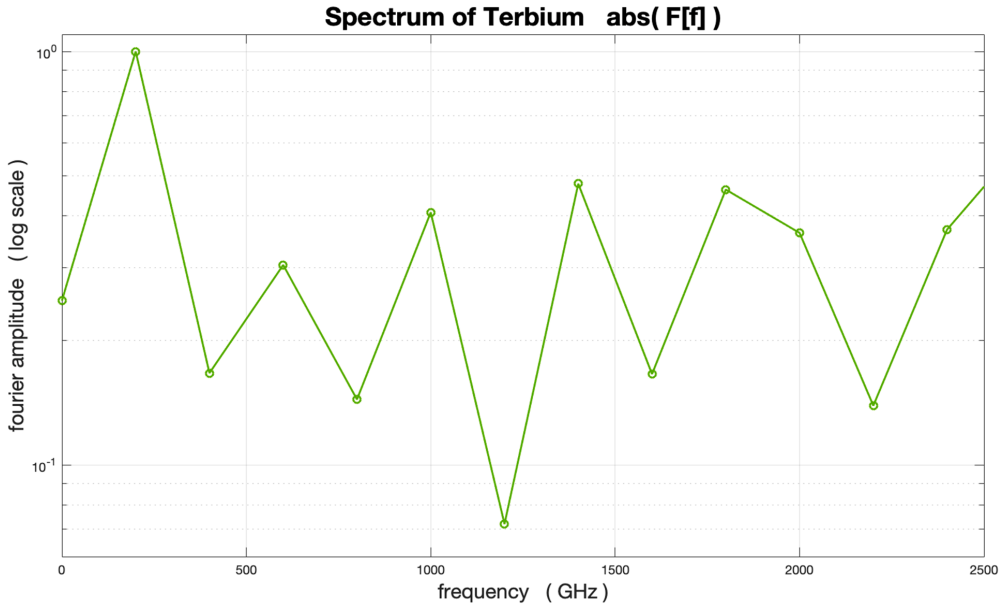

Figure 7.6: Fourier decomposition of the terbium dynamics spectrum in the 1-6ps regime sampled at 200 fs. No notable peaks indicate that the perceived oscillations are artifacts of under-sampling.

Chapter 8

Conclusion

This work has focused primarily on the characterization of two thermally-driven magnetic phenomena: the meta-magnetic transition in FeRh thin films and the ultrafast magnetization reversal in amorphous Gd-Tb-Co thin films. It has also covered the structural characterization of amorphous RE-TM alloys both by electron microscopy and density measurements via XRR and RBS, revealing that growth effects can produce low/high density bilayers that result in unexpected magnetic behavior.

Thin-film growth was implemented and optimized with extensive structural and magnetic characterization. Epitaxial, FeRh thin films were fabricated on different substrates to introduce strain and the effect of strain and thickness on the transition temperature was determined separately. For unstrained films, the transition temperature drops below room temperature for films below 15 nm in thickness. Tensile strain decreases the transition temperature and compressive strain increases it. These effects were seen both experimentally and in DFT calculations, with excellent agreement between predicted and measured transition temperatures. For technological applications above room temperature, FeRh films epitaxially grown on KTO substrates are attractive candidates for magnetic storage applications as even 10 nm films possess a transition temperature comparable to that of bulk FeRh.

A membrane-based heater device for generation and application of large temperature gradients was designed with help from heat transfer simulations. The device was fabricated and tested for imaging of domain wall motion as a consequence of the spin Seebeck effect. The combination of early negative results in conjunction to discouraging reports in the literature that removed or questioned the initial motivation and its theoretical support led to the cancellation of the project. However, the devices designed are ideal for temperature-based experiments with synchrotron techniques that require X-Ray transmission.

Fluctutation electron microscopy measurements of a-$Tb_{16}Co_{84}$ revealed a distinct difference in MRO as a function of growth temperature and tilt angle. It was shown that the material becomes more ordered as the growth temperature increases, and it orders along a specific direction: normal to the film's plane. This preferential ordering along the growth direction correlates with the higher anisotropy constants found in these samples, and are consistent with the models and measurements of the early 1990s. Angle-resolved FEM is a powerful technique that could produce

a new paradigm in the structural characterization of amorphous materials.

An unexpected experimentally discovered coexistence of a soft/hard bilayer in single layer amorphous, ferrimagnetic Tb-Co thin films was found to arise from a growth effect that promotes a low density/high density bilayer which behaves as an exchange-spring magnet at low temperatures. The low density bottom layer is magnetically soft; for film thickness near 1 nm, it is superparamagnetic, and at thickness of 2 nm it is a soft ferrimagnet. For greater thicknesses, the bottom layer retains its soft magnetic nature, while the remainder of the film is denser and has strong perpendicular magnetic anisotropy, leading to exchange spring behavior when the anisotropy becomes large, either at low temperatures or via a Pt overlayer which adds a strong interfacial anisotropy to the layer. Micromagnetic simulations reproduced the experimental hysteretic behavior by incorporating the experimentally-determined anisotropy and magnetization parameters into a soft/hard bilayer model. XRR and RBS are exceptional and complementary tools for the structural characterization of amorphous thin films. This hidden low density layer is probably present in many other material systems, but these phases will magnetically decouple only when the difference in anisotropy energy is large, which in this case occurs at low temperatures only. The presence of a Pt interface enhances the anisotropy constant.

We discovered that a-$Gd_{22-x}Tb_xCo_{78}$ thin films exhibit HI-AOS from x = 0 to x = 18, displaying similar demagnetization dynamics and slower remagnetization times with increased critical fluences as Tb content increases. The remagnetization dynamics were explained on the basis of increased damping as the Tb atomic percentage increases. The systematic increase in K_{ui} with increasing Tb content is not correlated with HI-AOS, and annealing led to a slowing of the remagnetization rate, which as verified by simulations indicates that damping is responsible for modifying the ultrafast magnetization dynamics. Two-temperature modeling of the dynamics reproduced the experimentally observed behavior as well as the strong dependence of critical fluence with increasing Tb content. The experimental inability to observe HI-AOS in a-Tb-Co is due to the high critical fluence that under the present conditions is inaccessible without ablating the film. This suggests that better management of the laser thermal load may lead to HI-AOS beyond Gd-TM alloys.

Preliminary results from time resolved XMCD measurements indicate that upon irradiating a-$Gd_{10}Tb_{12}Co_{78}$ a two-step magnetization reversal process ensues consisting of an initial fast drop in the magnetization, followed by a slower remagnetization in the opposite direction. The cobalt sublattice demagnetizes fastest with a time constant of 320 fs, followed by Tb and Gd with time constants of 410 fs and 630 fs respectively. The demagnetization times are consistent with those found in the previous chapter via TR-MOKE and with literature. More data needs to be collected in order to better characterize the zero-crossing of the magnetization and the lifespan of the transient ferromagnetic state between Co and Gd/Tb. Studying other compositions is planned for future work and this will help elucidate what are the factors that enable and modify helicity-independent all optical switching.

RE-TM alloys have a rich parameter space and their capability for HI-AOS is unparalleled and ripe with potential. Structurally there is still a lot left untapped with the technique of angle-resolved fluctuation electron microscopy, with reverse Monte Carlo simulations potentially yielding precise atomic structural models. The effect of damping was identified as one of the critical factors enabling and modifying the ultrafast magnetization dynamics, so a natural extension is to measure

the element specific damping parameters in *a*-Gd-Tb-Co alloys via XFMR. The high damping of some of these alloys however has to date made FMR hard to resolve, which will be a problem for XFMR as well, so appropriate choice of materials will be needed. Inherent anisotropies in the precessional angles and orbits of the magnetization as it relaxes to equilibrium could be uncovered that further illuminate the physical mechanism of HI-AOS.

Bibliography

[1] M. Fallot. *Ann. Phys. (Leipzig)*, 10(291):291, 1938.

[2] F Bergevin and L de Muldaver. Antiferromagnetic-ferromagnetic transformations in ferh. *J. Chem. Phys*, 35:1904–1905, 1961.

[3] JS Kouvel and CC Hartelius. Anomalous magnetic moments and transformations in the ordered alloy ferh. In *Proceedings of the Seventh Conference on Magnetism and Magnetic Materials*, pages 1343–1344. Springer, 1962.

[4] Leonid M. Sandratskii and Phivos Mavropoulos. *Phys. Rev. B*, 83(17):174408, 2011.

[5] MR Ibarra and PA Algarabel. Giant volume magnetostriction in the ferh alloy. *Physical Review B*, 50(6):4196, 1994.

[6] Nguyen T Nam, W Lu, and T Suzuki. Exchange bias of ferromagnetic/antiferromagnetic in fept/ferh bilayers. *Journal of Applied Physics*, 105(7):07D708, 2009.

[7] Jan-Ulrich Thiele, Stefan Maat, and Eric E Fullerton. Ferh/fept exchange spring films for thermally assisted magnetic recording media. *Applied Physics Letters*, 82(17):2859–2861, 2003.

[8] Denise Hinzke and Ulrich Nowak. Domain wall motion by the magnonic spin seebeck effect. *Physical review letters*, 107(2):027205, 2011.

[9] M. Fallot and R. Horcart. *Rev. Sci. 77, 498*, 77(498):291, 1939.

[10] V. L. Moruzzi and P. M. Marcus. *Phys. Rev. B*, 46:2864–2873, Aug 1992.

[11] S. Maat, J.-U. Thiele, and Eric E. Fullerton. *Phys. Rev. B*, 72:214432, Dec 2005.

[12] Jan-Ulrich Thiele, Stefan Maat, and Eric E. Fullerton. *Applied Physics Letters*, 82(17), 2003.

[13] J. U. Thiele, S. Maat, J. L. Robertson, and E. E. Fullerton. *IEEE Transactions on Magnetics*, 40(4):2537–2542, July 2004.

[14] David W. Cooke, F. Hellman, C. Baldasseroni, C. Bordel, S. Moyerman, and E. E. Fullerton. *Phys. Rev. Lett.*, 109:255901, Dec 2012.

[15] Enric Stern-Taulats, Adri Grcia-Condal, Antoni Planes, Pol Lloveras, Maria Barrio, Josep-Llus Tamarit, Sabyasachi Pramanick, Subham Majumdar, and Llus Maosa. *Applied Physics Letters*, 107(15), 2015.

[16] Q. J. Yap, J. J. Qiu, P. Luo, J. F. Ying, G. C. Han, D. E. Laughlin, J.-G. Zhu, T. Kanbe, and T. Shige. *Journal of Applied Physics*, 116(4), 2014.

[17] T. J. Zhou, K. Cher, J. F. Hu, Z. M. Yuan, and B. Liu. *Journal of Applied Physics*, 111(7), 2012.

[18] Ippei Suzuki, Takayoshi Koike, Mitsuru Itoh, Tomoyasu Taniyama, and Tetsuya Sato. *Journal of Applied Physics*, 105(7), 2009.

[19] G. C. Han, J. J. Qiu, Q. J. Yap, P. Luo, D. E. Laughlin, J. G. Zhu, T. Kanbe, and T. Shige. *Journal of Applied Physics*, 113(17), 2013.

[20] R.O. Cherifi, V. Ivanovskaya, L.C. Phillips, A. Zobelli, I.C. Infante, E. Jacquet, V. Garcia, S. Fusil, P.R. Briddon, N. Guiblin, A. Mougin, A.A. Unal, F. Kronast, S. Valencia, B. Dkhil, A. Barthelemy, and M. Bibes. *Nat. Mater.*, 13:345, January 2014.

[21] Ippei Suzuki, Mitsuru Itoh, and Tomoyasu Taniyama. *Applied Physics Letters*, 104(2):022401, 2014.

[22] C. Bordel, J. Juraszek, David W. Cooke, C. Baldasseroni, S. Mankovsky, J. Minár, H. Ebert, S. Moyerman, E. E. Fullerton, and F. Hellman. *Phys. Rev. Lett.*, 109:117201, Sep 2012.

[23] David W. Cooke, F. Hellman, J. R. Groves, B. M. Clemens, S. Moyerman, and E. E. Fullerton. *Review of Scientific Instruments*, 82(2), 2011.

[24] C. Baldasseroni, G. K. Plsson, C. Bordel, S. Valencia, A. A. Unal, F. Kronast, S. Nemsak, C. S. Fadley, J. A. Borchers, B. B. Maranville, and F. Hellman. *Journal of Applied Physics*, 115(4), 2014.

[25] C. Baldasseroni, C. Bordel, A. X. Gray, A. M. Kaiser, F. Kronast, J. Herrero-Albillos, C. M. Schneider, C. S. Fadley, and F. Hellman. *Applied Physics Letters*, 100(26), 2012.

[26] C Baldasseroni, C Bordel, C Antonakos, A Scholl, K H Stone, J B Kortright, and F Hellman. *Journal of Physics: Condensed Matter*, 27(25):256001, 2015.

[27] S. Polesya, S. Mankovsky, D. Ködderitzsch, J. Minár, and H. Ebert. *Phys. Rev. B*, 93:024423, Jan 2016.

[28] J. Kudrnovskỳ, V. Drchal, and I. Turek. *Phys. Rev. B*, 91(1):014435, 2015.

[29] R. Y. Gu and V. P. Antropov. *Phys. Rev. B*, 72:012403, Jul 2005.

[30] Stephen J May, PJ Ryan, JL Robertson, J-W Kim, Tiffany S Santos, Evgenia Karapetrova, Jerel L Zarestky, X Zhai, SGE Te Velthuis, JN Eckstein, et al. *Nature materials*, 8(11):892–897, 2009.

[31] K Uchida, S Takahashi, K Harii, J Ieda, W Koshibae, Kazuya Ando, S Maekawa, and E Saitoh. Observation of the spin seebeck effect. *Nature*, 455(7214):778, 2008.

[32] K Uchida, J Xiao, Hiroto Adachi, J-i Ohe, S Takahashi, J Ieda, T Ota, Y Kajiwara, H Umezawa, H Kawai, et al. Spin seebeck insulator. *Nature materials*, 9(11):894, 2010.

[33] Ken-ichi Uchida, Hiroto Adachi, Takeru Ota, Hiroyasu Nakayama, Sadamichi Maekawa, and Eiji Saitoh. Observation of longitudinal spin-seebeck effect in magnetic insulators. *Applied Physics Letters*, 97(17):172505, 2010.

[34] C Baldasseroni, DR Queen, David W Cooke, K Maize, A Shakouri, and F Hellman. Heat transfer simulation and thermal measurements of microfabricated x-ray transparent heater stages. *Review of Scientific Instruments*, 82(9):093904, 2011.

[35] P Hansen. Handbook of magnetic materials vol 6, ed khj buschow, 1991.

[36] BL Zink and F Hellman. Specific heat and thermal conductivity of low-stress amorphous si–n membranes. *Solid State Communications*, 129(3):199–204, 2004.

[37] AD Avery, MR Pufall, and Barry L Zink. Observation of the planar nernst effect in permalloy and nickel thin films with in-plane thermal gradients. *Physical review letters*, 109(19):196602, 2012.

[38] Jack Bass and William P Pratt Jr. Spin-diffusion lengths in metals and alloys, and spin-flipping at metal/metal interfaces: an experimentalists critical review. *Journal of Physics: Condensed Matter*, 19(18):183201, 2007.

[39] P Chaudhari, JJ Cuomo, and RJ Gambino. Amorphous metallic films for bubble domain applications. *IBM Journal of Research and Development*, 17(1):66–68, 1973.

[40] R. C. Taylor and A. Gangulee. Magnetization and magnetic anisotropy in evaporated GdCo amorphous films. *Journal of Applied Physics*, 47(10):4666–4668, October 1976.

[41] P. Hansen, C. Clausen, G. Much, M. Rosenkranz, and K. Witter. Magnetic and magnetooptical properties of rareearth transitionmetal alloys containing Gd, Tb, Fe, Co. *Journal of Applied Physics*, 66(2):756–767, July 1989.

[42] P Hansen and K Witter. The role of the compensation temperature in thermomagnetic switching. *IEEE Transactions on Magnetics*, 24(6):2317–2319, 1988.

[43] Y Suzuki, S Takayama, F Kirino, and N Ohta. Single ion model for perpendicular magnetic anisotropy in re-tm amorphous films. *IEEE transactions on magnetics*, 23(5):2275–2277, 1987.

[44] VG Harris, KD Aylesworth, BN Das, WT Elam, and NC Koon. Structural origins of magnetic anisotropy in sputtered amorphous tb-fe films. *Physical review letters*, 69(13):1939, 1992.

[45] F Hellman and EM Gyorgy. Growth-induced magnetic anisotropy in amorphous tb-fe. *Physical review letters*, 68(9):1391, 1992.

[46] F. Hellman, M. Messer, and E. N. Abarra. Coercivity in amorphous TbFe alloys. *Journal of Applied Physics*, 86(2):1047–1052, July 1999.

[47] MMJ Treacy and JM Gibson. Variable coherence microscopy: A rich source of structural information from disordered materials. *Acta Crystallographica Section A: Foundations of Crystallography*, 52(2):212–220, 1996.

[48] V. G. Harris, K. D. Aylesworth, B. N. Das, W. T. Elam, and N. C. Koon. Structural origins of magnetic anisotropy in sputtered amorphous tb-fe films. *Phys. Rev. Lett.*, 69:1939–1942, Sep 1992.

[49] Niklas Roschewsky, Tomoya Matsumura, Suraj Cheema, Frances Hellman, Takeshi Kato, Satoshi Iwata, and Sayeef Salahuddin. Spin-orbit torques in ferrimagnetic GdFeCo alloys. *Appl. Phys. Lett.*, 109(11):112403, September 2016.

[50] JongHyuk Kim, DongJoon Lee, Kyung-Jin Lee, Byeong-Kwon Ju, Hyun Cheol Koo, Byoung-Chul Min, and OukJae Lee. Spin-orbit torques associated with ferrimagnetic order in Pt/GdFeCo/MgO layers. *Sci Rep*, 8(1):6017, December 2018.

[51] Soong-Geun Je, Juan-Carlos Rojas-Snchez, Thai Ha Pham, Pierre Vallobra, Gregory Malinowski, Daniel Lacour, Thibaud Fache, Marie-Claire Cyrille, Dae-Yun Kim, Sug-Bong Choe, Mohamed Belmeguenai, Michel Hehn, Stphane Mangin, Gilles Gaudin, and Olivier Boulle. Spin-orbit torque-induced switching in ferrimagnetic alloys: Experiments and modeling. *Appl. Phys. Lett.*, 112(6):062401, February 2018.

[52] Woo Seung Ham, Sanghoon Kim, Duck-Ho Kim, Kab-Jin Kim, Takaya Okuno, Hiroki Yoshikawa, Arata Tsukamoto, Takahiro Moriyama, and Teruo Ono. Temperature dependence of spin-orbit effective fields in Pt/GdFeCo bilayers. *Appl. Phys. Lett.*, 110(24):242405, June 2017.

[53] Kohei Ueda, Maxwell Mann, Chi-Feng Pai, Aik-Jun Tan, and Geoffrey S. D. Beach. Spin-orbit torques in Ta/Tb $_{x}$ Co $_{100-x}$ ferrimagnetic alloy films with bulk perpendicular magnetic anisotropy. *Appl. Phys. Lett.*, 109(23):232403, December 2016.

[54] Robert Streubel, Charles-Henri Lambert, Noah Kent, Peter Ercius, Alpha T. N'Diaye, Colin Ophus, Sayeef Salahuddin, and Peter Fischer. Experimental Evidence of Chiral Ferrimagnetism in Amorphous GdCo Films. *Advanced Materials*, 30(27):1800199, July 2018.

[55] I. Radu, K. Vahaplar, C. Stamm, T. Kachel, N. Pontius, H. A. Drr, T. A. Ostler, J. Barker, R. F. L. Evans, R. W. Chantrell, A. Tsukamoto, A. Itoh, A. Kirilyuk, Th. Rasing, and A. V. Kimel. Transient ferromagnetic-like state mediating ultrafast reversal of antiferromagnetically coupled spins. *Nature*, 472(7342):205–208, April 2011.

[56] C. D. Stanciu, A. Tsukamoto, A. V. Kimel, F. Hansteen, A. Kirilyuk, A. Itoh, and Th. Rasing. Subpicosecond Magnetization Reversal across Ferrimagnetic Compensation Points. *Physical Review Letters*, 99(21), November 2007.

[57] T.A. Ostler, J. Barker, R.F.L. Evans, R.W. Chantrell, U. Atxitia, O. Chubykalo-Fesenko, S. El Moussaoui, L. Le Guyader, E. Mengotti, L.J. Heyderman, F. Nolting, A. Tsukamoto, A. Itoh, D. Afanasiev, B.A. Ivanov, A.M. Kalashnikova, K. Vahaplar, J. Mentink, A. Kirilyuk, Th. Rasing, and A.V. Kimel. Ultrafast heating as a sufficient stimulus for magnetization reversal in a ferrimagnet. *Nature Communications*, 3(1), January 2012.

[58] M. L. M. Lalieu, M. J. G. Peeters, S. R. R. Haenen, R. Lavrijsen, and B. Koopmans. Deterministic all-optical switching of synthetic ferrimagnets using single femtosecond laser pulses. *Physical Review B*, 96(22), December 2017.

[59] Jon Gorchon, Charles-Henri Lambert, Yang Yang, Akshay Pattabi, Richard B. Wilson, Sayeef Salahuddin, and Jeffrey Bokor. Single shot ultrafast all optical magnetization switching of ferromagnetic Co/Pt multilayers. *Applied Physics Letters*, 111(4):042401, July 2017.

[60] Frances Hellman, Axel Hoffmann, Yaroslav Tserkovnyak, Geoffrey SD Beach, Eric E Fullerton, Chris Leighton, Allan H MacDonald, Daniel C Ralph, Dario A Arena, Hermann A Dürr, et al. Interface-induced phenomena in magnetism. *Reviews of modern physics*, 89(2):025006, 2017.

[61] Matts Björck and Gabriella Andersson. GenX: an extensible X-ray reflectivity refinement program utilizing differential evolution. *Journal of Applied Crystallography*, 40(6):1174–1178, Dec 2007.

[62] M Mayer. Report ipp 9/113, max-planck-institut fur plasmaphysik. *Germany: Garching*, 1977.

[63] Eric E Fullerton, J.S Jiang, and S.D Bader. Hard/soft magnetic heterostructures: model exchange-spring magnets. *Journal of Magnetism and Magnetic Materials*, 200(1-3):392–404, October 1999.

[64] Wenjing Si, GP Zhao, N Ran, Y Peng, FJ Morvan, and XL Wan. Deterioration of the coercivity due to the diffusion induced interface layer in hard/soft multilayers. *Scientific reports*, 5:16212, 2015.

[65] A. Bill and H.B. Braun. Magnetic properties of exchange springs. *Journal of Magnetism and Magnetic Materials*, 272-276:1266–1267, May 2004.

[66] J S Jiang and S D Bader. Rational design of the exchange-spring permanent magnet. *J. Phys.: Condens. Matter*, 26(6):064214, February 2014.

[67] J S Jiang and S D Bader. Magnetic reversal in thin lm exchange-spring magnets q. *Scripta Materialia*, page 6, 2002.

[68] Arne Vansteenkiste, Jonathan Leliaert, Mykola Dvornik, Mathias Helsen, Felipe Garcia-Sanchez, and Bartel Van Waeyenberge. The design and verification of mumax3. *AIP advances*, 4(10):107133, 2014.

[69] E. Beaurepaire, J.-C. Merle, A. Daunois, and J.-Y. Bigot. Ultrafast Spin Dynamics in Ferromagnetic Nickel. *Physical Review Letters*, 76(22):4250–4253, May 1996.

[70] MB Agranat, SI Ashitkov, AB Granovskii, and GI Rukman. Interaction of picosecond laser pulses with the electron, spin, and phonon subsystems of nickel. *Zh. Eksp. Teor. Fiz*, 86(1376):10, 1984.

[71] A Vaterlaus, D Guarisco, M Lutz, M Aeschlimann, M Stampanoni, and F Meier. Different spin and lattice temperatures observed by spin-polarized photoemission with picosecond laser pulses. *Journal of Applied Physics*, 67(9):5661–5663, 1990.

[72] A. Vaterlaus, T. Beutler, and F. Meier. Spin-lattice relaxation time of ferromagnetic gadolinium determined with time-resolved spin-polarized photoemission. *Physical Review Letters*, 67(23):3314–3317, December 1991.

[73] Alexey V. Kimel and Mo Li. Writing magnetic memory with ultrashort light pulses. *Nature Reviews Materials*, 4(3):189–200, March 2019.

[74] S. Mangin, M. Gottwald, C-H. Lambert, D. Steil, V. Uhl, L. Pang, M. Hehn, S. Alebrand, M. Cinchetti, G. Malinowski, Y. Fainman, M. Aeschlimann, and E. E. Fullerton. Engineered materials for all-optical helicity-dependent magnetic switching. *Nature Materials*, 13(3):286–292, March 2014.

[75] R. Moreno, T. A. Ostler, R. W. Chantrell, and O. Chubykalo-Fesenko. Conditions for thermally induced all-optical switching in ferrimagnetic alloys: Modeling of TbCo. *Physical Review B*, 96(1), July 2017.

[76] Sabine Alebrand, Ute Bierbrauer, Michel Hehn, Matthias Gottwald, Oliver Schmitt, Daniel Steil, Eric E. Fullerton, Stphane Mangin, Mirko Cinchetti, and Martin Aeschlimann. Subpicosecond magnetization dynamics in TbCo alloys. *Physical Review B*, 89(14), April 2014.

[77] Tian-Min Liu, Tianhan Wang, Alexander H. Reid, Matteo Savoini, Xiaofei Wu, Benny Koene, Patrick Granitzka, Catherine E. Graves, Daniel J. Higley, Zhao Chen, Gary Razinskas, Markus Hantschmann, Andreas Scherz, Joachim Sthr, Arata Tsukamoto, Bert Hecht, Alexey V. Kimel, Andrei Kirilyuk, Theo Rasing, and Hermann A. Drr. Nanoscale Confinement of All-Optical Magnetic Switching in TbFeCo - Competition with Nanoscale Heterogeneity. *Nano Letters*, 15(10):6862–6868, October 2015.

[78] M. Vomir, M. Albrecht, and J.-Y. Bigot. Single shot all optical switching of intrinsic micron size magnetic domains of a Pt/Co/Pt ferromagnetic stack. *Applied Physics Letters*, 111(24):242404, December 2017.

[79] C. E. Graves, A. H. Reid, T. Wang, B. Wu, S. de Jong, K. Vahaplar, I. Radu, D. P. Bernstein, M. Messerschmidt, L. Mller, R. Coffee, M. Bionta, S. W. Epp, R. Hartmann, N. Kimmel, G. Hauser, A. Hartmann, P. Holl, H. Gorke, J. H. Mentink, A. Tsukamoto, A. Fognini, J. J. Turner, W. F. Schlotter, D. Rolles, H. Soltau, L. Strder, Y. Acremann, A. V. Kimel, A. Kirilyuk, Th. Rasing, J. Sthr, A. O. Scherz, and H. A. Drr. Nanoscale spin reversal by non-local angular momentum transfer following ultrafast laser excitation in ferrimagnetic GdFeCo. *Nature Materials*, 12(4):293–298, April 2013.

[80] F Hellman, M Messer, and EN Abarra. Coercivity in amorphous tb–fe alloys. *Journal of applied physics*, 86(2):1047–1052, 1999.

[81] A Mekonnen, M Cormier, AV Kimel, Andrei Kirilyuk, Ales Hrabec, Laurent Ranno, and Th Rasing. Femtosecond laser excitation of spin resonances in amorphous ferrimagnetic gd 1- x co x alloys. *Physical review letters*, 107(11):117202, 2011.

[82] J Barker, U Atxitia, TA Ostler, O Hovorka, O Chubykalo-Fesenko, and RW Chantrell. Two-magnon bound state causes ultrafast thermally induced magnetisation switching. *Scientific reports*, 3:3262, 2013.

[83] A. Brunsch and J. Schneider. Perpendicular magnetic anisotropy in evaporated amorphous GdCo films. *Journal of Applied Physics*, 48(6):2641–2643, June 1977.

[84] Sotaro Esho. Perpendicular magnetic anisotropy in sputtered GdCo films. *Journal of Applied Physics*, 50(2):1006–1009, February 1979.

[85] A. Mekonnen, A. R. Khorsand, M. Cormier, A. V. Kimel, A. Kirilyuk, A. Hrabec, L. Ranno, A. Tsukamoto, A. Itoh, and Th. Rasing. Role of the inter-sublattice exchange coupling in short-laser-pulse-induced demagnetization dynamics of GdCo and GdCoFe alloys. *Physical Review B*, 87(18), May 2013.

[86] N. Bergeard, V. Lpez-Flores, V. Halt, M. Hehn, C. Stamm, N. Pontius, E. Beaurepaire, and C. Boeglin. Ultrafast angular momentum transfer in multisublattice ferrimagnets. *Nature Communications*, 5(1), December 2014.

[87] V López-Flores, N Bergeard, V Halté, C Stamm, N Pontius, M Hehn, E Otero, E Beaurepaire, and C Boeglin. Role of critical spin fluctuations in ultrafast demagnetization of transition-metal rare-earth alloys. *Physical Review B*, 87(21):214412, 2013.

[88] N Bergeard, A Mougin, M Izquierdo, E Fonda, and F Sirotti. Correlation between structure, electronic properties, and magnetism in co x gd 1- x thin amorphous films. *Physical Review B*, 96(6):064418, 2017.

[89] R. F. L. Evans, W. J. Fan, P. Chureemart, T. A. Ostler, M. O. A. Ellis, and R. W. Chantrell. Atomistic spin model simulations of magnetic nanomaterials. *Journal of Physics Condensed Matter*, 26(10), 2014.

[90] VAMPIRE software package. version 5. Available from https://vampire.york.ac.uk/.

[91] A. Eschenlohr, M. Sultan, A. Melnikov, N. Bergeard, J. Wieczorek, T. Kachel, C. Stamm, and U. Bovensiepen. Role of spin-lattice coupling in the ultrafast demagnetization of $gd_{1-x}tb_x$ alloys. *Phys. Rev. B*, 89:214423, Jun 2014.

[92] G. Malinowski, K. C. Kuiper, R. Lavrijsen, H. J. M. Swagten, and B. Koopmans. Magnetization dynamics and Gilbert damping in ultrathin Co48fe32b20 films with out-of-plane anisotropy. *Applied Physics Letters*, 94(10):102501, March 2009.

[93] M. C. Hickey and J. S. Moodera. Origin of Intrinsic Gilbert Damping. *Physical Review Letters*, 102(13), March 2009.

[94] P. He, X. Ma, J. W. Zhang, H. B. Zhao, G. Lpke, Z. Shi, and S. M. Zhou. Quadratic Scaling of Intrinsic Gilbert Damping with Spin-Orbital Coupling in L 1 0 FePdPt Films: Experiments and *Ab Initio* Calculations. *Physical Review Letters*, 110(7), February 2013.

[95] J. Gorchon, R. B. Wilson, Y. Yang, A. Pattabi, J. Y. Chen, L. He, J. P. Wang, M. Li, and J. Bokor. Role of electron and phonon temperatures in the helicity-independent all-optical switching of gdfeco. *Phys. Rev. B*, 94:184406, Nov 2016.

[96] T. L. Gilbert. A phenomenological theory of damping in ferromagnetic materials. *IEEE Transactions on Magnetics*, 40(6):3443–3449, Nov 2004.

[97] A. R. Khorsand, M. Savoini, A. Kirilyuk, A. V. Kimel, A. Tsukamoto, A. Itoh, and Th. Rasing. Element-Specific Probing of Ultrafast Spin Dynamics in Multisublattice Magnets with Visible Light. *Physical Review Letters*, 110(10), March 2013.

[98] Daniel Schick, Loıc Le Guyader, Niko Pontius, Ilie Radu, Torsten Kachel, Rolf Mitzner, Thomas Zeschke, Christian Schüßler-Langeheine, Alexander Föhlisch, and Karsten Holldack. Analysis of the halo background in femtosecond slicing experiments. *Journal of synchrotron radiation*, 23(3):700–711, 2016.

[99] A.P. Mihai L.H. Lewis D. Heiman M.A. de Vries, M. Loving and C.H. Marrows. *New Journal of Physics*, 15(1):013008, 2013.

[100] Chloe Baldasseroni. *Ph.D. Thesis, University of California, Berkeley*, 2013.

[101] P. E. Blöchl. *Phys. Rev. B*, 50:17953–17979, Dec 1994.

[102] G. Kresse and D. Joubert. *Phys. Rev. B*, 59:1758–1775, Jan 1999.

[103] G. Kresse and J. Hafner. *Phys. Rev. B*, 47:558–561, Jan 1993.

[104] G. Kresse and J. Furthmüller. *Phys. Rev. B*, 54:11169–11186, Oct 1996.

[105] John P. Perdew, Kieron Burke, and Matthias Ernzerhof. *Phys. Rev. Lett.*, 77:3865–3868, Oct 1996.

[106] Hendrik J. Monkhorst and James D. Pack. Special points for brillouin-zone integrations. *Phys. Rev. B*, 13:5188–5192, Jun 1976.

[107] R F L Evans, W J Fan, P Chureemart, T A Ostler, M O A Ellis, and R W Chantrell. Atomistic spin model simulations of magnetic nanomaterials. *Journal of Physics: Condensed Matter*, 26(10):103202, March 2014.

[108] SI Anisimov and BL Kapeliovich. Electron emission from metal surfaces exposed to ultrashort laser pulses. *Zh. Eksp. Teor. Fiz*, 66(2):375–377, 1974.

Appendix A

Supplementary Materials for FeRh

Table A.1 lists the lattice parameters and transition temperatures T* and widths. Magnetization measurements as a function of temperature were done with a Quantum Design SQUID under a constant magnetic field of 5 T. The exception to this is for FeRh films grown on KTO for which the whole transition lies beyond the temperature capability of the SQUID. For these films a vibrating sample magnetometer was used to measure the magnetization as a function of temperature from 310 K - 500 K in a 1 T magnetic field. The relation of -8K/T was used to adjust these values to 5 T, i.e. after obtaining the transition temperatures from the VSM measurements we subtracted 32 K to account for the 4 T difference. Thus all the tabulated values for the transition temperatures in table S1 correspond to those under a 5 T field.

X-ray diffraction measurements (Fig. 2.3) were used to obtain the in-plane and out of plane lattice parameters from which the strain was extracted. A triple axis PANalytical X'Pert diffractometer was used with Cu K-α radiation. The diffraction measurements were done at room temperature and under no magnetic field. XRD measurements confirmed the epitaxial growth of FeRh films on all substrates. Comparing FeRh's (110) peaks with respect to its substrate yielded the same epitaxial relationship: (001) FeRh // (001) substrates and [100] FeRh // [110] substrates. The chemical order parameter S was extracted for all films from the XRD intensities using[99, 100] S = $\sqrt{I_{001}^{exp}/I_{002}^{exp}}/\sqrt{I_{001}^{calc}/I_{002}^{calc}}$. The chemical order for all films were within the reported value S = 0.88 $\pm$ 0.04[99, 100]. Using $(\omega - 2\theta)$ scans the (002) peak of FeRh was used to calculate the out of plane c lattice parameter, while the (101) peak was used to extract the in-plane a lattice parameter. From a and c, with $b = a$, the average Poisson ratio was calculated to be $\nu = 0.37 \pm 0.08$, using the equation $\frac{-2\nu}{1-\nu} = \frac{(c-a_{AF})/a_{AF}}{(a-a_{AF})/a_{AF}}$ (where a_{AF} is the bulk lattice parameter in the AF state) which takes into account the biaxial strain supplied by the substrate.

The 15 and 10 nm films grown on MgO and STO were in the ferromagnetic state when measured due to their lower T*. To correct for this and present the data in the AF state the volume of these films is calculated. The calculation assumes that the in-plane lattice parameters, a and b, are equal and unchanged during the transition due to substrate clamping. The volume is reduced by 1% during the FM$\rightarrow$AF transition, so we take off 1% of the calculated volume, finally divide this new volume by a^2 to get the corrected c value that is used in the main paper. The values reported

in the table are in the as-measured state. All other films were in the antiferromagnetic state.

Density functional theory (DFT) calculations are performed using the projector augmented wave (PAW) formalism [101, 102] and a plane wave basis set, as implemented in the Vienna ab initio simulation package (VASP) [103, 104]. The exchange and correlation potential are treated in the framework of generalized gradient approximation (GGA) of Perdew-Burke-Ernzerbof (PBE) [105]. Spin-polarized calculations were used. The wave functions were expanded in plane waves up to a cutoff of 400 eV and the convergence precision of the total energy was set to be lower than 1×10^{-5} eV. A $2 \times 2 \times 2$ supercell (16 atoms) was used to calculate bulk FeRh characteristics, whereas a $2 \times 2 \times 1$ was used for the thin film. For the summation of charge densities over the Brillouin zone, $5 \times 5 \times 5$ Gamma-central K-points was used for bulk calculations while $5 \times 5 \times 1$ for thin film calculations [106]. Conjugate gradient algorithm was adopted to optimize the atomic structures with the atomic force lower than 0.01 eV/Å.

DFT has been performed to calculate the crystal parameters, electronic and magnetic properties of FeRh bulk. The calculated crystal parameters are 2.989 Å for AF state and 3.010 Å for FM state, very close to the experimental 2.985 Å and 2.995 Å, respectively. The calculated Fe and Rh magnetic moment are 3.098 μB and 0.0 μB per atom in AF state, and 3.179 μB and 1.042 μB per atom in FM state, respectively. The origin of such magnetic moment can be deduced from the spin-polarized electronic density of states (DOS), as shown in Figure A.1. We can see that *d* electrons of Fe atoms in AF state have strong spin polarization near Fermi level, leading to big net magnetic moment, while Rh atoms has symmetrical DOS without net magnetic moment. In FM state, *d* electrons of both Fe and Rh have spin splitting. The density of Fe is larger than that of Rh, indicating a larger net magnetic moment in Fe. The Fe and Rh DOS corresponding to the same spin projection also show a common peak structure. This feature reveals strong hybridization of the Fe and Rh *d* electron in both spin channels.

We can also see that DOS near Fermi level is not empty and is different in AF and FM states. Such behavior could result into different electronic entropy in two states. In our calculations for FeRh bulk with experimental lattice parameters, the free total energy difference ΔE ($E_{FM} - E_{AF}$) between the FM and the AF state is 0.057 eV (every Fe atom) when electronic entropy is not included. However, ΔE decreases to 0.033 eV when electronic entropy is included. This indicates electronic entropy favors FM state and tends to make an AF to FM transition with the increasing temperature. Similar results have been discussed by previous work [4, 28].

To extract the strain dependence of the transition temperature, T^*, from the strain dependence of ΔE values calculated by DFT we proceed as follows:

At the transition temperature T^*, the Gibbs free energy for the FM and AF state are equal so

$$E_{FM} - T^* S_{FM} + PV_{FM} = E_{AF} - T^* S_{AF} + PV_{AF} \tag{A.1}$$

Collecting terms:

$$\Delta E = E_{FM} - E_{AF} = T^*(S_{FM} - S_{AF}) - P(V_{FM} - V_{AF}) = T^* \Delta S - P\Delta V \tag{A.2}$$

where the thermodynamic variables (E,S,V) are all taken at T^*. Since V_{FM} is only one percent larger than V_{AF}, even for P = 1 atm the $P\Delta V$ term is negligible compared to ΔE (1.68 x 10^{-7}

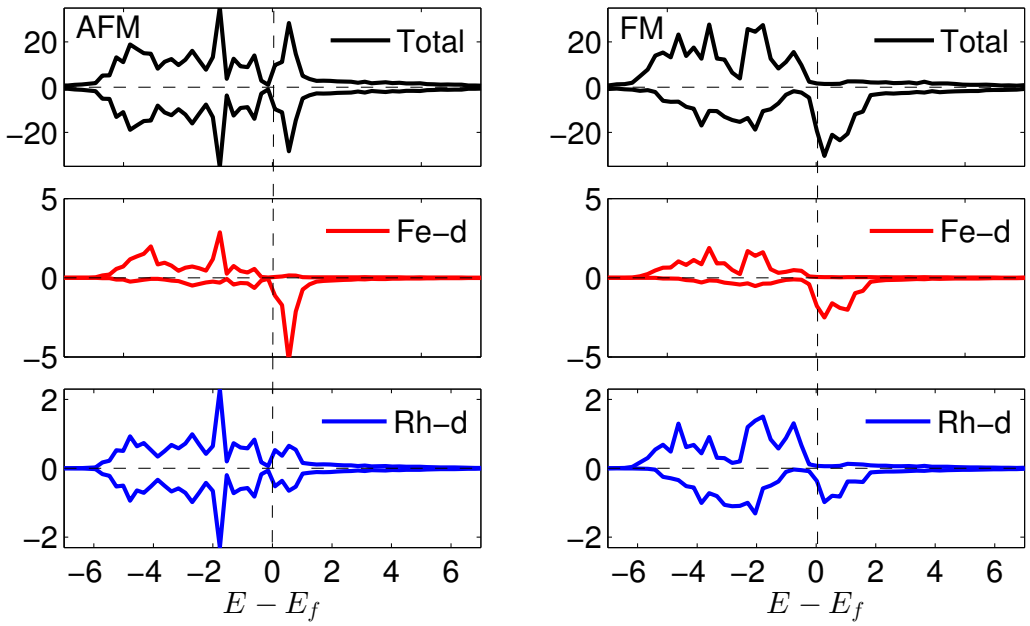

Figure A.1: Density of states of AF (left) and FM (right) phase. The top panel is the total density of all the atoms; the middle panel is the density of d-electrons in one Fe atom; the bottom panel is the density of d-electrons in one Rh atom. In each panel the line with positive DOS values corresponds to the spin-up projection and the line with negative DOS values corresponds to the spin-down projection. The vertical dashed line indicates the Fermi level.

eV/FeRh molecule vs 0.03 eV/FeRh molecule). We therefore neglect the $P\Delta V$ term resulting in

$$\Delta E|_{T^*} = T^* \Delta S|_{T^*} \tag{A.3}$$

where both ΔE and ΔS are explicitly evaluated at T*. We next expand each:

$$\Delta E|_{T^*} = \Delta E|_{0\mathrm{K}} + \int_0^{T^*} (C_{FM} - C_{AF})\, dT = \Delta E|_{0\mathrm{K}} + \int_0^{T^*} \Delta C\, dT \approx \Delta E|_{0\mathrm{K}}$$

$$\Delta S|_{T^*} = \Delta S|_{0\mathrm{K}} + \int_0^{T^*} \frac{\Delta C}{T}\, dT = \int_0^{T^*} \frac{\Delta C}{T}\, dT = \frac{L}{T^*} \tag{A.4}$$

where L is the latent heat of the transition. Equations (4) include two terms, the energy and entropy difference between the FM and AF states at zero Kelvin plus a temperature-dependent contribution obtained by integrating the specific heat difference $\Delta C = C_{FM} - C_{AF}$ or $\Delta C/T$ from zero to T*. At T = 0, ΔS = 0 since both phases are chemically and magnetically ordered, so ΔS at T* is due entirely to a temperature-dependent S, due to various excitation of the system, dominated by magnetic

excitations which are different in the FM and AF phases, as discussed in Cooke et al.[14] This integrated $\Delta C/T$ gives $\Delta S\ |_{T^*} \approx 2.7$ x 10^{-5} eV/FeRh molecule/K (1.06 x 10^{20} eV/kg/K)(Cooke et al.[14]), comparable to that derived from the measured latent heat at T*. The integrated ΔC is 0.0028 eV/FeRh molecule, significantly smaller than the 0.03 eV/FeRh molecule T = 0 energy difference calculated by DFT; we therefore neglect that term.

The above equations (3) combined with (4) therefore yield

$$\Delta E|_{T^*} \approx \Delta E|_{0\mathrm{K}} \approx T^* \Delta S|_{T^*} = T^* \int_0^{T^*} \frac{\Delta C}{T}\, dT = L \tag{A.5}$$

which we rearrange to write

$$T^* = \frac{\Delta E|_{0\mathrm{K}}}{\Delta S|_{T^*}} \tag{A.6}$$

For c/a = 1 and T* = 350 K, $\Delta E|_{0\mathrm{K,\ c/a\ =\ 1}}$ (which we define as ΔE_0) is 0.03 eV/FeRh molecule (from DFT presented in this paper). We (somewhat similarly) define $\Delta S|_{T^*,\ \mathrm{c/a\ =\ 1}}$ as ΔS_0. For other values of c/a we apply a Taylor expansion truncated to the first-order term.

$$T^* = T_0^* + \frac{\partial T^*}{\partial (c/a)} \times \delta(c/a) \tag{A.7}$$

Here T_0^* is the transition temperature for c/a = 1 (350 K), and $\delta(c/a)$ = c/a - 1 denotes the change between c/a values. The partial derivative of T^* with respect to c/a is obtained by using the chain rule on eq.(6), treating both the entropy and internal energy as functions of c/a.

$$\frac{\partial T^*}{\partial (c/a)} = \frac{\partial (\Delta E|_{0\mathrm{K}})}{\partial (c/a)} \frac{1}{\Delta S|_{T^*,\ \mathrm{c/a\ =\ 1}}} - \frac{\Delta E_0}{(\Delta S|_{T^*,\ \mathrm{c/a\ =\ 1}})^2} \frac{\partial (\Delta S|_{T^*})}{\partial (c/a)} \tag{A.8}$$

which we rewrite as

$$\frac{\partial T^*}{\partial (c/a)} = \frac{\partial (\Delta E|_{0\mathrm{K}})}{\partial (c/a)} \frac{1}{\Delta S_0} - \frac{\Delta E_0}{(\Delta S_0)^2} \frac{\partial (\Delta S|_{T^*})}{\partial (c/a)} \tag{A.9}$$

We assume that the partial derivative of $\Delta S|_{T^*}$ with respect to c/a is small compared to the partial derivative of $\Delta E|_{0\mathrm{K}}$ with respect to c/a, i.e. that the effects of strain on the excitation spectrum (ΔC) are smaller than the effects on the ground state energy. We also assume that the temperature-dependent term of $\Delta E|_{T^*} (= \int_0^{T^*} \Delta C\, dT)$ remains small and similarly independent of c/a. Thus we obtain

$$\frac{\partial T^*}{\partial (c/a)} = \frac{\partial (\Delta E|_{0\mathrm{K}})}{\partial (c/a)} \frac{1}{\Delta S_0} \tag{A.10}$$

We then approximate the derivative of $\Delta E|_{0\mathrm{K}}$ with respect to c/a by taking differences of $\Delta E|_{0\mathrm{K,\ c/a}}$ from ΔE_0 (the value of $\Delta E|_{0\mathrm{K,\ c/a\ =\ 1}}$).

$$\frac{\partial (\Delta E|_{0\mathrm{K}})}{\partial (c/a)} \approx \frac{(\Delta E|_{0\mathrm{K,\ c/a}} - \Delta E_0)}{\delta (c/a)} = \frac{(\Delta E|_{0\mathrm{K,\ c/a}} - \Delta E_0)}{(c/a) - 1} \tag{A.11}$$

Substituting eq.(10) and (11) into eq. (7)

$$T^* = T_0^* + \frac{(\Delta E|_{0\mathrm{K,\ c/a}} - \Delta E_0)}{(c/a-1)} \frac{1}{\Delta S_0}(c/a-1) \tag{A.12}$$

Cancelling the common term we arrive at

$$T^* = T_0^* + \frac{(\Delta E|_{0\mathrm{K,\ c/a}} - \Delta E_0)}{\Delta S_0} \tag{A.13}$$

Finally we substitute (from Eq. 6) $\Delta S|_{T^*,\ \mathrm{c/a\ =\ 1}} \equiv \Delta S_0 = \frac{\Delta E|_{0\mathrm{K,\ c/a\ =\ 1}}}{T_0^*} \equiv \frac{\Delta E_0}{T_0^*}$ to reach the equation presented in the main text

$$T^* = T_0^* \left(1 + \frac{(\Delta E|_{0\mathrm{K,\ c/a}} - \Delta E_0)}{\Delta E_0}\right) \tag{A.14}$$

The derivation for the transition temperature for figure 4 follows the same procedure as above, except that we now treat energy and entropy as functions of 1/N, with N being the number of monolayers of FeRh. The procedure is done as a function of 1/N because N = ∞ for bulk and approaches zero for smaller thicknesses, thus making it possible to apply a Taylor expansion in 1/N.

We note that the DFT-derived value of $\Delta E|_{0\mathrm{K}}$ = 0.03 eV/FeRh molecule together with the measured T* of 350 K gives a theoretical value of $\Delta S|_{T^*,\mathrm{c/a\ =\ 1}}$ = 8.5x10^{-5} eV/FeRh molecule/K, three times larger than the experimental values of $\Delta S|_{T^*}$ (measured either from integrating C/T of thin films or from the latent heat of bulk samples). Note also that including the temperature dependence of energy ($\int_0^{T^*} \Delta C\, dT$) (dropped in the discussion above in eq. (4)) would somewhat increase this difference. This discrepancy suggests an overestimation of ΔE, which is very sensitive to the lattice parameters and computational methods; different values of DFT-derived ΔE are found in the literature[4, 29]. This discrepancy has been noted elsewhere in the literature, where corrections to the calculated ΔE to align the measured ΔS to the measured T* have been used[29]. This effect will not affect the calculation of the strain dependence of T*; equations (13) and (14) show the normalization which cancels out this effect, but it makes a calculation of T* itself not quantitatively correct; i.e. combining the DFT-derived $\Delta E|_{0\mathrm{K}}$ directly with an experimental value of $\Delta S|_{T^*}$ yields a significantly too large value of T*.

	a Lattice Parameter (Å)	*c* Lattice Parameter (Å)	Transition Temperature T* (K)	Width of Transition (K)	T^*_{AF-FM}	T^*_{FM-AF}
MgO						
10 nm	2.984 ± 0.006	3.021 ± 0.004	230 ± 35	70	265	195
15 nm	2.986 ± 0.005	3.012 ± 0.004	288 ± 32	65	320	255
22 nm	2.989 ± 0.004	2.985 ± 0.003	331 ± 22	44	353	309
100 nm	2.986 ± 0.004	2.983 ± 0.003	346 ± 10	19	355	336
KTO						
10 nm	2.961 ± 0.004	3.027 ± 0.004	341 ± 17	34	358	324
15 nm	2.972 ± 0.004	3.024 ± 0.004	377 ± 14	27	391	364
22 nm	2.975 ± 0.003	3.022 ± 0.003	386 ± 11	21	397	376
100 nm	2.976 ± 0.003	3.004 ± 0.003	366 ± 8	15	373	358
STO						
10 nm	2.983 ± 0.008	3.016 ± 0.008	256 ± 31	61	286	225
15 nm	2.987 ± 0.007	3.008 ± 0.006	297 ± 27	53	323	270
22 nm	2.987 ± 0.006	2.984 ± 0.004	322 ± 17	34	339	305
100 nm	2.985 ± 0.004	2.985 ± 0.003	345 ± 6	12	351	339
IBAD MgO						
100 nm	3.001 ± 0.006	2.964 ± 0.004	331 ± 12	24	343	319

Table A.1: Values for the lattice constants are presented as measured. 10 and 15 nm films on MgO and STO are in the FM state when measured in the X-ray diffractometer. Values for the transition temperatures for FeRh films grown on MgO, IBAD MgO and STO are presented as measured in a 5 T magnetic field. Values for the transition temperatures for FeRh films grown on KTO have been adjusted to account for the 4 T difference since these films were measured in a 1 T field.

Appendix B

Atomistic spin dynamics and supplementary information

B.1 Atomistic Simulations

For the numerical investigation of spin dynamics under femtosecond laser excitation, Sergiu Ruta and Roy Chantrell of the University of York developed and simulated a model of amorphous, ferrimagnetic $Gd_{22-x}Tb_xCo_{78}$ thin films. The atomistic level simulation allows to model each atomic type (Gd,Tb,Co) independently and it has been previously used to accurately describe HI-AOS in ferrimagnets. The energy of the system is described by the spin Hamiltonian

$$\mathscr{H} = -\sum_{i<j} J_{i,j} S_i \cdot S_j - \sum_i k_u (S_i^z)^2 \tag{B.1}$$

where the spin S_i is a unit vector describing the local spin direction. It is normalized to the local atomic spin magnetic moment (μ_s). We use μ_{Co} = 1.61 μ_B for the magnetic moment on Co sites, μ_{Gd} = 7.63 μ_B for the Gd sites, and μ_{Tb} = 9.34 μ_B for the Tb sites.

The magnetic anisotropy, k_u, is taken from literature as: 8.07 x 10^{-24} for Gd, 2.16 x 10^{-22} for Tb and 3.73 x 10^{-23} for Co[75]. $J_{i,j}$ is the exchange constant and is limited to nearest neighbor interactions.The work of Hansen et al.[41] shows that the RE-TM exchange does not depend on the RE concentration, whereas the TM-TM exchange interaction is strongly influenced by the presence of RE. To describe the effect as observed experimentally, the effective Co-Co exchange is taken as:

$$J^{\text{eff}}_{\text{Co-Co}} = J^{\text{bulk}}_{\text{Co-Co}} + J_{\text{Co-Tb-Co}} \frac{x}{1-x-y} + J_{\text{Co-Gd-Co}} \frac{y}{1-x-y} \tag{B.2}$$

where x and y are the Tb and Gd atomic concentrations respectively. For Tb-Co the above equation simplifies to:

$$J^{\text{eff}}_{\text{Co-Co}} = J^{\text{bulk}}_{\text{Co-Co}} + J_{\text{Co-Tb-Co}} \frac{x}{1-x} \tag{B.3}$$

Similarly for Gd-Co:

$$J^{\text{eff}}_{\text{Co-Co}} = J^{\text{bulk}}_{\text{Co-Co}} + J_{\text{Co-Gd-Co}} \frac{y}{1-y} \tag{B.4}$$

The exchange parameters used are given in the following table:

Exchange Interaction	$J^{\text{bulk}}_{\text{Co-Co}}$	$J_{\text{Co-Tb-Co}}$	$J_{\text{Co-Gd-Co}}$	$J_{\text{Co-Gd}}$	$J_{\text{Co-Tb}}$	$J_{\text{Gd-Gd}}$	$J_{\text{Tb-Gd}}$	$J_{\text{Tb-Tb}}$
Exchange Value (1x10^{21} J)	5.9	-4.4	-5.366	-1.25	-1.0	1.26	1.0	0.82

Table B.1: Exchange values used for the atomistic spin dynamics simulations

Based on the above exchange parameters both the compensation temperature and Curie temperature do not vary in the a-$Gd_{22-x}Tb_xCo_78$ system, with the Tc around 800K and the compensation temperature around 400K.

The system dynamics are computed using the VAMPIRE software package[107] based on the Landau-Lifshitz-Gilbert (LLG) equation:

$$\partial_t S_i = -\frac{\gamma}{(1+\alpha^2)}[S_i \times B^i_{\text{eff}} + \alpha_i S_i \times (S_i \times B^i_{\text{eff}})] \tag{B.5}$$

where γ is the gyromagnetic ratio and α is the Gilbert damping factor. The on-site effective field can be computed as summation of the local field derived from the spin Hamiltonian with a random field to model the heat bath:

$$B^i_{\text{eff}} = -\frac{\partial \mathscr{H}}{\partial S_i} + \zeta_i \tag{B.6}$$

where ζ_i is a stochastic thermal field due to the interaction of the conduction electrons with the local spins. The stochastic thermal field is assumed to have Gaussian statistics and satisfies:

$$\langle \zeta_{i,a}(t)\zeta_{j,b}(t')\rangle = \delta_{ij}\delta_{ab}(t-t')2\alpha_i k_B T \mu_i/\gamma_i \tag{B.7}$$

$$\langle \zeta_{i,a}(t)\rangle = 0 \tag{B.8}$$

where k_B is the Boltzmann constant and T is the temperature. We incorporate the rapid change in thermal energy of a system under the influence of a femtosecond laser pulse. The spin system is coupled to the electron temperature, Te, which is calculated using the two-temperature model[108]:

$$T_e C_e \frac{dT_e}{dt} = -G_{el}(T_l - T_e) + P(t) \tag{B.9}$$

$$C_l \frac{dT_l}{dt} = -G_{el}(T_e - T_l) \tag{B.10}$$

where C_e =700 $Jm^{-3}K^{-1}$, C_l=3.0 x 10^6 $Jm^{-3}K^{-1}$, G_{el}=17 x 10^{17} $Wm^{-3}K^{-1}$ are similar with the values used to simulate a-Gd-Fe-Co[57] and a-Tb-Co[75]. P(t) models the temperature from the laser pulse into the electronic system. The pulse has a width of 70 fs.

B.2 Supplementary Materials

EDS Maps

Figure B.1 shows elemental mapping of a 15 nm thick, a-$Gd_{10}Tb_{12}Co_{78}$ sample capped with 7nm of Ta taken on an FEI TitanX, operated at 200 kV in STEM mode with an approximate probe size of 3 nm diameter. EDS maps were created and analyzed using the Bruker EDS software package.

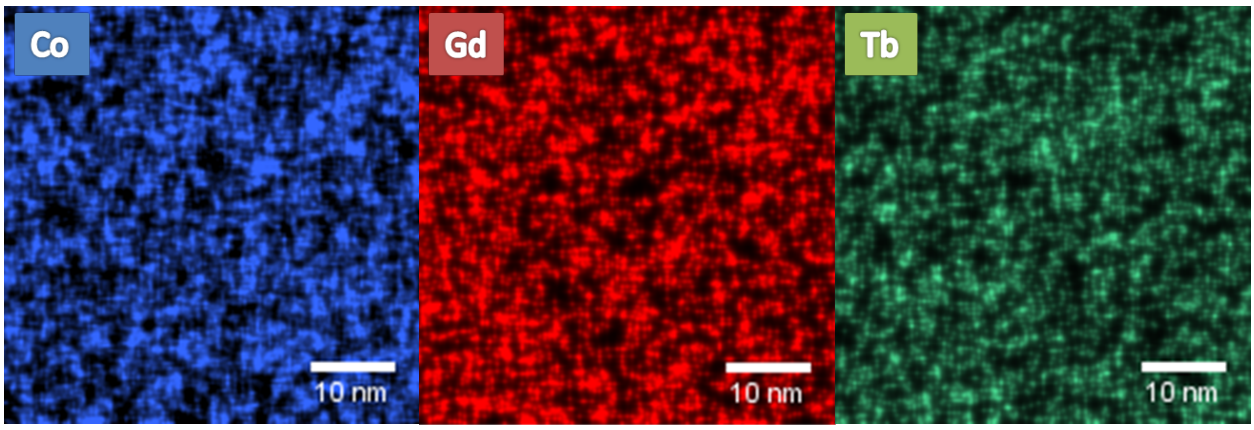

Figure B.1: Scanning Transmission Electron Microscopy Images with Energy Dispersive Spectroscopy found no evidence of inhomogeneities down to the 10nm scale, below which the discreteness of the 3 nm probe size shows up as pixelation in the images. The work by Graves et al.[79] reported clustering of each atomic species in *a*-Gd-Fe-Co at the 10 nm scale and argued that angular momentum transfer from RE-rich regions to TM-rich regions is responsible for HI-AOS in *a*-RE-TM systems.

Time constants

Table B.2 summarizes the demagnetization constants extracted from a single exponential fit to the time-resolved data of Fig. 6.5b of the main text,

Extended Time Dynamics

Figure B.2 presents the extended time dynamics of the magnetization to illustrate the magnetization recovery timescale after laser irradiation.

Sample	$\tau(ps)$	Time to reach 50% reversal (ps)	Lower Bound (ps)	Upper Bound (ps)
$Gd_{22}Co_{78}$	0.69 $\pm$0.07	3.62	3.32	3.75
$Gd_{18}Tb_4Co_{78}$	0.58 $\pm$0.05	6.24	5.73	7.49
$Gd_{14}Tb_8Co_{78}$	0.53 $\pm$0.06	7.45	6.61	7.85
$Gd_{10}Tb_{12}Co_{78}$	0.49 $\pm$0.06	8.05	7.89	8.91
$Gd_7Tb_{15}Co_{78}$	0.37 $\pm$0.04	19.93	19.79	21.75
$Gd_4Tb_{18}Co_{78}$	0.30 $\pm$0.04	21.34	21.11	26.33
$Tb_{22}Co_{78}$	0.32 $\pm$0.06	N/A	N/A	N/A

Table B.2: Demagnetization constants extracted from a single exponential fit to the time-resolved data of fig. 6.5b

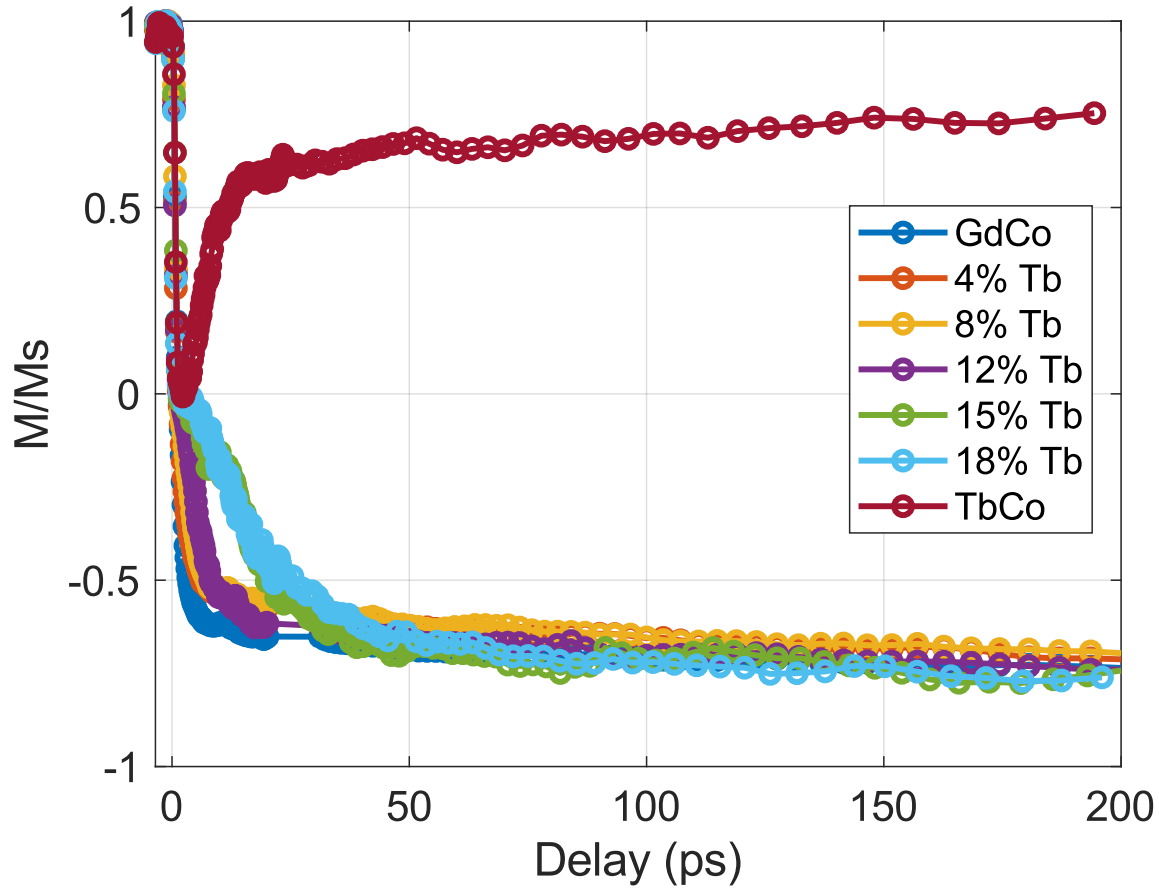

Figure B.2: Expanded scale of the ultrafast magnetization dynamics illustrating the recovery of the magnetization after 200 ps post laser illumination.